

Anomalous $B(E2)_{4^+/2^+}$ Ratios in the Neutron-Deficient Nuclide ^{168}Os and ^{166}W

Thesis submitted in accordance with the requirements of the University of
Liverpool for the degree of Doctor in Philosophy

by

Bahadır Saygı

Oliver Lodge Laboratory

September 2013

This thesis is dedicated to my Mum and Dad.

Thank you.

“Let no one ignorant of geometry enter.”

Over the entrance of Plato Academy.

“O gemi bir gün mutlaka gelecek.”

İsmail Abi, Leyla ile Mecnun.

Acknowledgements

I know that it is a big cliché but I should say that “time is passing so fast”. I cannot believe that four years have gone that quickly and I am writing this section.

I would like to thank my supervisor Dr. David Joss for providing the opportunity to work on this exciting nuclear physics research project. I could not manage my research without him. He has become a perfect guide for me in nuclear physics and life during the past four years and I am sure that he will be there when I need him in the future.

I would like to thank Prof. Robert Page for many useful and interesting discussions. He always changed my perspective on the problems at hand whenever I needed a better one.

I am grateful to Dr. Dave O’Donnell for his all responses to my questions in nuclear physics and proofreading of a very early draft of this thesis. He will be always a good mentor and a good friend in my life.

Next to thanks go to Dr. Tuomas Grahn, Dr. Liam Gaffney and Dr. Robert Carroll for helping me to understand how I can do proper data sorting and lifetime measurements.

A huge thanks to Dr. Joe Rees and Dr. Mark Drummond. I could write pages and pages on these two names but I will keep them for myself. Liverpool became a better place for me after I met you two. Cheers guys and salutes from flat 27 in 71 Sefton Street.

I would like to thank all the friends I met in the department, Dr. Filiz Ertuğral, Dr. John Revill, Dr. Eddie Parr, Andy Mistry, Jamie Dormand and Alex Thornthwaite...the list goes on, for dinners in Kimos, the proofreading of this thesis, having chats during the tea sessions in the third floor, making trips warmer to Jyväskylä, Finland and night shifts.

Many thanks to Prof. Sefa Ertürk for encouraging me since my early steps in research life. He was always on the phone with his wisdom when I was looking for advice. Now, the distance is getting closer, Sir. I am coming back to Turkey.

I would like to thank Dr. Şebnem Kandil İngeç. She taught me a lot when I was an undergraduate student at Gazi University and encouraged me with the idea doing a Ph.D in abroad.

I would like to thank the Turkish Ministry of National Education for providing the funding for my research. I would also like to thank all the people at the University Liverpool and Jyväskylä that made the research possible.

Thanks to all the Turkish friends I made in London, Liverpool and Manchester.

The last thank goes to my family. I believe that they deserve to hear it in Turkish. Sevgili babacığım Abdil Sayğı (nam-ı diğer Reis) ve anneciğım Döndü Sayğı, evden üniversite eğitimim için ayrıldığım ilk günden itibaren hem Ankara’da hem de Liverpool’da geçirdiğim sürede sizin manevi desteğiniz olmasaydı, tezime bir kelime dahi yazamazdım. Varlığınız her zaman benim için bir dayanak noktasıdır. Sayğı ve sevgilerimle ellerinizden öperim.

Abstract

The structure of the neutron-deficient nuclides ^{168}Os and ^{166}W has been investigated in experiments using the JUROGAM γ -ray spectrometer and GREAT spectrometer in conjunction with RITU separator at the Accelerator Laboratory of the University of Jyväskylä. The excitation level scheme for ^{168}Os has been extended and the lifetimes of excited states in ^{166}W have been measured using the DPUNS differential plunger and the recoil distance Doppler-shift method. These states were produced using by a fusion-evaporation reaction using a ^{92}Mo target and a ^{78}Kr beam. This thesis addresses the anomalous $B(E2; 4_1^+ \rightarrow 2_1^+)/B(E2; 2_1^+ \rightarrow 0_1^+)$ ratios measured for these neutron-deficient $N = 92$ isotones. The extended level scheme of ^{168}Os has revealed several new features. These features were investigated in a model using the Bateman equations and based on the differential decay curve method to provide possible explanations for the anomalous $B(E2)_{4^+/2^+}$ ratios in ^{168}Os extracted from recent lifetime measurements by Grahn *et al.* [1]. In a complementary experiment, the lifetimes of the 2^+ , 4^+ , 6^+ , 12^+ and 14^+ excited states in ^{166}W have been measured for the first time using recoil gated γ - γ -coincidence spectra. The measured reduced transition probabilities revealed a $B(E2; 4^+ \rightarrow 2^+)/B(E2; 2^+ \rightarrow 0^+)$ ratio less than unity. The $B(E2)$ value for the transitions between high-spin states provides evidence for a weak interaction strength at the ground-Stockholm band crossing.

Contents

1	Concepts in Nuclear Physics	23
1.1	The Spherical Shell Model	23
1.2	Definition of the Nuclear Shapes	28
1.3	Deformed Shell Model	29
1.3.1	The Nilsson Potential	31
1.4	Collective Motion	33
1.4.1	Nuclear Vibration	34
1.4.2	Nuclear Rotation	34
1.5	The Features of Gamma Decay	36
1.5.1	The Kinematics of Gamma Decay	36
1.5.2	Electromagnetic Transition Rates	36
1.5.3	Selection Rules for γ -Ray Transitions	38
1.6	Natural Decay Law and Bateman Equations	39
2	Experimental Methodology	42
2.1	Fusion Evaporation Reactions	42
2.2	The JUROGAMII γ -ray spectrometer	44
2.2.1	Gas-Filled Recoil Separators	45
2.2.2	The Recoil Ion Transport Unit (RITU)	46
2.3	The Gamma Recoil Electron Alpha Tagging (GREAT) Spectrometer	46

2.4	Data Acquisition	49
2.4.1	Recoil Gating	51
2.5	The DPUNS Plunger	51
2.6	Lifetime Measurement Techniques	54
2.6.1	The Recoil Distance Doppler Shift Method (RDDS)	54
2.7	The Differential Decay Curve Method (DDCM)	59
2.7.1	Fundamental Mathematics of DDCM	59
2.7.2	DDCM for Coincidence Analysis	62
3	New Excited States in ^{168}Os	66
3.1	Introduction	67
3.2	Experimental Details	69
3.3	Results	70
3.4	Discussion	77
3.4.1	Configuration Assignments	77
3.4.2	Reduced Transition Probabilities	80
3.4.3	The Model	87
3.5	Summary	95
4	Lifetime measurements of excited states in ^{166}W	96
4.1	Introduction	97
4.2	Experimental Details	97
4.3	Results	99
4.3.1	The 2^+ , 4^+ and 6^+ states	99
4.3.2	The 12^+ and 14^+ states	107
4.4	Discussion	113
4.4.1	Reduced Transition Probabilities	113
4.4.2	The Level Scheme of ^{166}W	118

4.4.3	Comparison with Nuclear Models	124
4.4.4	High-Spin Structure of ^{166}W	127
4.5	Summary	130
5	Conclusion and Future Work	131

List of Figures

1	Experimental $B(E2)$ values for 2^+ and 4^+ excited states in non-magic nuclei in the region $40 \leq Z \leq 80$. The diagonal line represents $B(E2; 4^+ \rightarrow 2^+) = B(E2; 2^+ \rightarrow 0^+)$. Filled diamonds and $^{152}\text{Dy}_{86}$ use data from National Nuclear Data Center (NNDC). Exceptions are in the figure are listed; $^{98}\text{Ru}_{54}$ [23], $^{114}\text{Te}_{62}$ [26], $^{114}\text{Xe}_{60}$ [27], $^{134}\text{Xe}_{80}$ [28], $^{132}\text{Ce}_{74}$ [29], $^{134}\text{Ce}_{74}$ [30], $^{132}\text{Nd}_{72}$ [31], $^{144}\text{Nd}_{84}$ [25], ^{166}W from present work, ^{168}Os [1] $^{180}\text{Pt}_{102}$ [24].	21
1.1	Comparison of Square-Well (black) Harmonic Oscillator (blue) and Woods-Saxon (red) potentials. The potentials are produced for illustration. . . .	25
1.2	Illustration of Spin-Orbit effect on nuclear shell. As mentioned in the text, a level with higher angular momentum $1h_{11/2}$ is lowered and a level with lower angular momentum $1h_{9/2}$ is raised.	27
1.3	The Lund Convention for describing quadrupole shapes.	30
1.4	Graphical representation of the Nilsson quantum numbers.	32
2.1	A schematic diagram of the process involved in the de-excitation of a compound nucleus formed in a fusion-evaporation reaction.	43
2.2	A schematic plan view diagram of the RITU gas-filled separator [61]. . . .	47
2.3	A schematic drawing of the Gamma Recoil Electron Alpha Tagging (GREAT) Spectrometer [55].	48

2.4	Schematic diagram of the TDR system's electronics and data acquisition adopted from Ref. [63]	50
2.5	A two-dimensional spectrum present the separation of recoils from the scattered beam. The time difference between the timing signals in MWPC and DSSD's (TOF) on the x-axis and energy loss signal in MWPC on the y-axis. The shaded area defines recoils.	52
2.6	A schematic drawing of the DPUNS plunger device [56] Target and degrader are placed into the target chamber. Stepper motor is employed to set the target-to-degrader distances. An actuator keep distance in balance during the beam bombardment. TESA is used to calibrate the induced target voltage.	53
2.7	Chart adopted from Ref. [67] which shows the different lifetime measuring techniques over the different time ranges.	55
2.8	A schematic illustration of the degrader and target foils adopted for recoil tagging experiments. The shifted component is the number of γ -ray emitted before the degrader in $0 \leq t < T$ time interval and the degraded component is the number of γ -ray emitted after degrader in $T \leq t < \infty$ time interval.	57
2.9	Hypothetical Level Scheme. Transition B is gated to measure the lifetime of state i in direct gating method of DDCM. Transition C is gated to measure the lifetime of state i in indirect gating method of DDCM. Transition C is a high-lying feeder for the level i , transition B is the direct feeder and transition A is the depopulator of the state i	60

2.10	Lifetime values calculated for different distances within the region of sensitivity are presented in the top panel. The solid line in the middle panel is a fit of the normalised shifted curve with second order polynomials to the data. The solid line in the panel on bottom is the fit of the degraded component with derivative of the second order polynomials multiplied by the lifetime τ	65
3.1	Level scheme deduced for ^{168}Os . The transition energies are given in keV and their relative intensities are proportional to the widths of the arrows. Energy levels are labelled with their excitation energies relative to the ground state and their spin and parity assignments. Parentheses indicate tentative assignments.	71
3.2	Double-gated γ -ray coincidence spectra correlated with a recoil implantation in the GREAT spectrometer. (a) spectrum showing γ rays in coincidence with the 642 and 643 keV transitions. (b) Spectrum showing γ rays in coincidence with the 579 and 692 keV transitions in Band 3. (c) Spectrum showing γ rays in coincidence with the 688 and 778 keV transitions in Band 4.	74
3.3	Double-gated γ -ray coincidence spectra correlated with a recoil implantation in the GREAT spectrometer. Spectra show a new decay path from the 12^+ state to the 9^- state in Band 3. (a) spectrum showing γ rays in coincidence with the 243 and 532 keV transitions. (b) Spectrum showing γ rays in coincidence with the 243 and 365 keV transitions.	75

3.4	Double-gated γ -ray coincidence spectra correlated with a recoil im- plantation in the GREAT spectrometer. Spectra show a new decay path from the 12^+ state to Band 1. Insets to the figure show the high-energy linking transitions from the quasi- β band to the ground- state band. (a) Spectrum showing γ rays in coincidence with the 516 and 516 keV transitions. (b) Spectrum showing γ rays in coincidence with the 516 and 543 keV transitions. (c) Spectrum showing γ rays in coincidence with the 543 and 582 keV transitions.	76
3.5	Comparison of the excitation energies of states in the new positive- parity structure in ^{168}Os (Band 1) with the quasi- β bands in the heavier Os isotopes. Data taken from references [88].	79
3.6	The total aligned angular momentum, I_x as a function of rotational fre- quency for the bands in ^{168}Os	81
3.7	Variation of ratio of the 4^+ and 2^+ state excitation energy in the even neutron-deficient $66 \leq Z \leq 78$ nuclei as function of neutron number. Data from National Nuclear Data Center (NNDC).	82
3.8	Comparison of experimental $B(E2)$ values of the 2^+ and 4^+ state in the even neutron-deficient $66 \leq Z \leq 78$ nuclei as a function of neutron num- ber. Data from National Nuclear Data Center (NNDC). Exceptions are ^{168}Os [1], ^{166}W from present work, τ of the 2^+ state in ^{172}W and ^{178}W [90], ^{174}W [91] and ^{176}W [92].	85
3.9	Comparison of experimental $B(E2)_{4^+/2^+}$ ratios in the even neutron-deficient $66 \leq Z \leq 78$ nuclei as a function of P factor. Data from National Nuclear Data Center (NNDC). Exceptions are ^{168}Os [1], ^{166}W from present work, τ of the 2^+ state in ^{172}W and ^{178}W [90], ^{174}W [91] and ^{176}W [92].	86
3.10	Hypothetical Level Scheme based on ^{168}Os . The labelling of the levels maps the real spins and parities on ^{168}Os to the labels used in the model.	88

3.11	Variation in the apparent half-life of state B (4^+) as a function of the half-life of the state Y (12^+). (a) The effect of a doublet with components above state Y. (b) The variation as a function of the half-life of state Y without a straddling doublet. Blue line indicates the measured half-life of the 4^+ state by Grahn <i>et al.</i> [1]. Red line indicates the half-life value of the state B(the 4^+ state) have been extracted from calculation for a ratio of $B(E2)_{4^+/2^+} = 1$	94
4.1	Typical recoil-gated γ - γ -coincidence spectra of ^{166}W recorded at three target-to-degrader distances with the 10 JUROGAMII detectors at 134° . The evolution of the shifted and the degraded components is shown as a function of target-to-degrader distance for depopulator (left column) and feeder (right column) transitions of the 2^+ state in ^{166}W . The dotted and dashed lines indicate the position of the fully shifted and degraded components of the depopulating transition, respectively.	101
4.2	Typical recoil-gated γ - γ -coincidence spectra of ^{166}W recorded at three target-to-degrader distances with the 10 JUROGAMII detectors at 134° . The evolution of the shifted and the degraded components is shown as a function of target-to-degrader distance for depopulator (left column) and feeder (right column) transitions of the 4^+ state in ^{166}W . The dotted and dashed lines indicate the position of the fully shifted and degraded components of the depopulating transition, respectively.	102

- 4.3 Typical recoil-gated γ - γ -coincidence spectra of ^{166}W recorded at three target-to-degrader distances with the 10 JUROGAMII detectors at 158° . The evolution of the shifted and the degraded components is shown as a function of target-to-degrader distance for depopulator (left column) and feeder (right column) transitions of the 6^+ state in ^{166}W . The dotted and dashed lines indicate the position of the fully shifted and degraded components of the depopulating transition, respectively. 103
- 4.4 A graph illustrating the principles of the DDCM. Top panel shows the normalised shifted curve of the 2^+ state of ^{166}W extracted from spectra recorded by detectors placed at 134° . Middle panel shows the intensity difference of the direct feeding and depopulating transition and the solid line is the derivative of the curve shown in the upper panel. Bottom panel shows the lifetime τ as a weighted mean of values τ 104
- 4.5 A graph illustrating the principles of the DDCM. Top panel shows the normalised shifted curve of the 4^+ state of ^{166}W extracted from spectra recorded by detectors placed at 134° . Middle panel shows the intensity difference of the direct feeding and depopulating transition and the solid line is the derivative of the curve shown in the upper panel. Bottom panel shows the lifetime τ as a weighted mean of values τ 105
- 4.6 A graph illustrating the principles of the DDCM. Top panel shows the normalised shifted curve of the 6^+ state of ^{166}W extracted from spectra recorded by detectors placed at 158° . Middle panel shows the intensity difference of the direct feeding and depopulating transition and the solid line is the derivative of the curve shown in the upper panel. Bottom panel shows the lifetime τ as a weighted mean of values τ 106

4.7	Evolution of the shifted and degraded components as a function of target-to-degrader distance for depopulator and feeder transition of the 12^+ state in ^{166}W with 10 JUROGAMII detectors at 134° . The dotted and dashed lines indicate the position of the fully shifted and degraded components of the depopulating transition, respectively.	109
4.8	A graph illustrating the principles of the DDCM. Top panel shows the normalised shifted curve of the 12^+ state of ^{166}W extracted from spectra recorded by detectors placed at 134° . Middle panel shows the intensity difference of the degraded component of the direct feeding and depopulating transition and the solid line is the derivative of the curve shown in the upper panel. Bottom panel shows the lifetime τ as a weighted mean of values τ	110
4.9	Evolution of the shifted and degraded components as a function of target-to-degrader distance for depopulator and feeder transition of the 14^+ state in ^{166}W with 10 JUROGAMII detectors at 134° . The dotted and dashed lines indicate the position of the fully shifted and degraded components of the depopulating transition, respectively.	111
4.10	A graph illustrating the principles of the DDCM. Top panel shows the normalised shifted curve of the 14^+ state of ^{166}W extracted from spectra recorded by detectors placed at 134° . Middle panel shows the intensity difference of the degraded component of the direct feeding and depopulating transition and the solid line is the derivative of the curve shown in the upper panel. Bottom panel shows the lifetime τ as a weighted mean of values τ	112

4.11	(a) Excitation energies of the 2^+ and 4^+ states as a function of neutron number for the W isotopes. (b) Experimental reduced transition probabilities $B(E2; 2^+ \rightarrow 0^+)$ as a function of neutron number for the W isotopes. (c) Experimental reduced transition probabilities $B(E2; 4^+ \rightarrow 2^+)$ as a function of neutron number for the W isotopes. Data for excitation energies from National Nuclear Data Center (NNDC). τ of the 2^+ state in ^{172}W and ^{178}W [90], ^{174}W [91] and ^{176}W [92]. ^{166}W from present work and τ of the 4^+ state from National Nuclear Data Center (NNDC).	115
4.12	Experimental $B(E2)_{4^+/2^+}$ ratios as a function of P factor. At this point, it makes sense including ^{168}W , because it reveals a ratio less than unity by errors, relative to ^{152}Dy . Data from National Nuclear Data Center (NNDC). Exceptions are ^{168}Os [1], ^{166}W from present work, $^{98}\text{Ru}_{54}$ [23], $^{114}\text{Te}_{62}$ [26], $^{114}\text{Xe}_{60}$ [27], $^{134}\text{Xe}_{80}$ [28], $^{132}\text{Ce}_{74}$ [29], $^{134}\text{Ce}_{74}$ [30], $^{132}\text{Nd}_{72}$ [31], $^{144}\text{Nd}_{84}$ [25], $^{180}\text{Pt}_{102}$ [24].	117
4.13	Double-gated γ -ray coincidence spectra correlated with a recoil implantation in the GREAT spectrometer. (a) spectrum showing γ rays in coincidence with the hypothesised 252 keV self-coincident doublet. (b) The 424 keV hypothesised doublet.	119
4.14	Examples of double-gated γ -ray coincidence spectra correlated with a recoil implantation in the GREAT spectrometer. (a) spectrum showing γ rays in coincidence with the 326 and 465 keV transitions showing transitions in the yrast band. (b) γ rays in coincidence with the 546 and 656 keV transitions showing transitions in Band 2. (c) γ rays in coincidence with the 373 and 528 keV transitions showing transitions in Band 3. (d) γ rays in coincidence with the 326 and 911 keV transitions.	120

4.15	Excitation energies of quasi- β bands in ^{166}W . Data taken from references [102]	121
4.16	Level scheme of ^{166}W showing the yrast and side bands [96].	123
4.17	The comparison of theoretical calculations for 2^+ states in tungsten isotopes with experimentally measured values. The theoretical values were taken from Reference [29]. (a) Finite-Range Droplet Model (FRDM) (b) WoodsSaxon Model (WSM) (c) Dynamical Microscopic Model (DMM) and (d) DMM calculations theoretical predictions were normalised with experimental value of ^{182}W . Data from National Nuclear Data Center (NNDC). Exceptions are ^{172}W and ^{178}W [90], ^{174}W [91] and ^{176}W [92]. ^{166}W from present work.	125
4.18	(a) B(E2) values of excited states for W isotopes as a function of neutron number. (b) Energies of excited states for W isotopes as a function of neutron number. Data from National Nuclear Data Center (NNDC). Exceptions are B(E2) values for ^{166}W from present work	128
4.19	(a) B(E2) values of excited states for W-isotopes as a function of neutron number. (b) Energies of excited states for W-isotopes as a function of neutron number. Data for ^{168}W from Ref [109], excitation energies for ^{166}W from Ref [96] and B(E2) values from present work.	129

Introduction

The collective behaviour of protons and neutrons resulting in vibrational and rotational excitations is one of the most important paradigms in nuclear physics [2]. It has long been established through experimental measurements that nucleon separation energies and the excitation energy of 2^+ states in even-even nuclei have relatively high values at certain magic numbers corresponding to closed shells [3, 4]. Conversely, the observation of rotational bands and large quadrupole moments at the mid-shells indicates that valence nucleons interact in a coherent manner to produce large average deformations [2]. The variation of such properties as a function of proton or neutron number has allowed the evolution of collectivity in atomic nuclei to be probed and has provided stringent constraints on theoretical descriptions.

The advent of selective tagging techniques has allowed excited states in the most exotic nuclei to be observed for the first time. For example, the recoil-decay tagging technique [5] that uses spatial and temporal correlations to identify γ -ray transitions in weakly populated nuclei by the subsequent radioactive decays of the emitting nucleus has revealed excited states in the over 40 nuclei in the neutron-deficient region below the $Z = 82$ shell gap [6, 7, 8, 9, 10]. The identification of excited states in atomic nuclei spanning complete shells is crucial to determining the evolution of collectivity. For example, recent tagging experiments of the light osmium isotopes have identified excited states completing an unbroken sequence of isotopes from $^{162}\text{Os}_{86}$ [11] to $^{198}\text{Os}_{122}$ [12], which spans most of the $82 \leq N \leq 126$ neutron shell.

Energy level systematics of the Os isotopes suggest that single-particle excitations dominate near the closed $N = 82$ shell but collectivity develops rapidly with increasing valence neutron number. Indeed, over a range of only eight neutrons the isotopes display features indicating behaviour related to vibrations, soft triaxiality, shape coexistence and well deformed rotation [13, 14, 15]. In recent years it has become possible to perform more detailed spectroscopic measurements of highly neutron-deficient nuclei. Considerable effort has been expended on developing techniques that allow detailed information to be determined regarding nuclear matrix elements. The exploitation of recoil-distance Doppler shift measurements using a differential plunger device in conjunction with recoil(-decay) tagging techniques has allowed the lifetimes of excited states to be measured [16]. The lifetime of excited states can be related to the reduced transition probability $B(E2)$, which provides a direct measure of collectivity. A systematic programme of lifetime measurements in heavy ($166 \leq A \leq 188$) neutron-deficient nuclei has started to reveal useful information about collective behaviour in the transitional nuclei above $N = 82$ [1, 17, 18, 19, 20].

Recent lifetime measurements by Grahn *et al.* of the low-lying states in ^{168}Os have revealed ratios of reduced transition probabilities that are unexpectedly low for a collective nucleus, $B(E2; 4^+ \rightarrow 2^+)/B(E2; 2^+ \rightarrow 0^+) = 0.36(14)^*$ [1]. Low $B(E2)_{4^+/2^+}$ ratios have been observed in several other cases around closed shells due to seniority effects [21] or due to shape coexistence where the 2^+ and 4^+ states belong to differently deformed configurations yet this behaviour is not expected in deformed nuclei with regular collective excitations [18, 19]. In 2004, a detailed survey of existing data was carried out by Çakırlı *et al.* [22]. Çakırlı's work was inspired by the lifetime measurement for ^{98}Ru , which revealed an anomalous $B(E2)_{4/2}$ ratio, which was compared with nine other nuclei with abnormal $B(E2)_{4^+/2^+}$ ratios. Çakırlı suggested these phenomena should be investigated further using other tech-

*Hereafter labelled $B(E2)_{4^+/2^+}$

Nuclide	P Factor	2004 B(E2) _{4/2}	Ref.	2013 B(E2) _{4/2}	Ref.
⁹⁸ Ru ₅₄	2.40	0.35(11)	[32]	1.86(16)	[23]
¹¹⁴ Te ₆₂	1.71	0.84(11)	[26]	0.84(11)	[26]
¹¹⁴ Xe ₆₀	2.86	0.99(9)	[27]	0.99(9)	[27]
¹³⁴ Xe ₈₀	1.33	0.76(7)	[28]	0.76(7)	[28]
¹³² Ce ₇₄	4.00	1.07(25)	[29]	1.07(25)	[29]
¹³⁴ Ce ₇₄	3.43	0.76(15)	[30]	0.76(15)	[30]
¹³² Nd ₇₂	5.00	0.88(6)	[31]	0.88(6)	[31]
¹⁴⁴ Nd ₈₄	1.67	0.73(9)	[33]	0.98(3)	[25]
¹⁶⁶ W ₉₂	4.44	-	-	0.33(5)	Present Work
¹⁶⁸ Os ₉₂	4.00	-	-	0.36(13)	[1]
¹⁸⁰ Pt ₁₀₂	3.33	0.9(2)	[34]	1.7(3)	[24]

Table 1: The abnormal B(E2)_{4/2} ratios.

niques such as Coulomb excitation. Since then, the measurements for ⁹⁸Ru and ¹⁸⁰Pt have been repeated and corrected using Coulomb excitation [23] and recoil-distance Doppler shift lifetime measurements [24], respectively. Of the remaining cases, Coulomb excitation of ¹⁴⁴Nd has provided a value more consistent with the collective model [25]. These results are encouraging for the collective theory since they suggest that the apparent abnormal behaviour may arise from experimental limitations. However, recent RDDS lifetime measurements for ¹⁶⁸Os and the lifetime measurements for ¹⁶⁶W exhibit anomalous B(E2)_{4+/2+} ratios that require explanation. The analysis of the $N = 92$ isotones, ¹⁶⁸Os and ¹⁶⁶W, has revealed the two lowest B(E2)_{4+/2+} values at 0.36(13) and 0.33(5), respectively. An updated survey inspired by Çakırlı *et al.* has been conducted in this work and is presented in Figure 1 and a comparison of B(E2)_{4+/2+} ratio from the recent measurements with the work of Çakırlı *et al.* is given in Table 1.

This thesis aims to discover the origins of the anomalous B(E2)_{4+/2+} ratios in ¹⁶⁸Os and ¹⁶⁶W. After a brief survey of the relevant nuclear physics concepts and experimental methodology new results reporting an extension the the level scheme of ¹⁶⁸Os are presented. The anomalous B(E2)_{4+/2+} ratios are discussed in terms of these

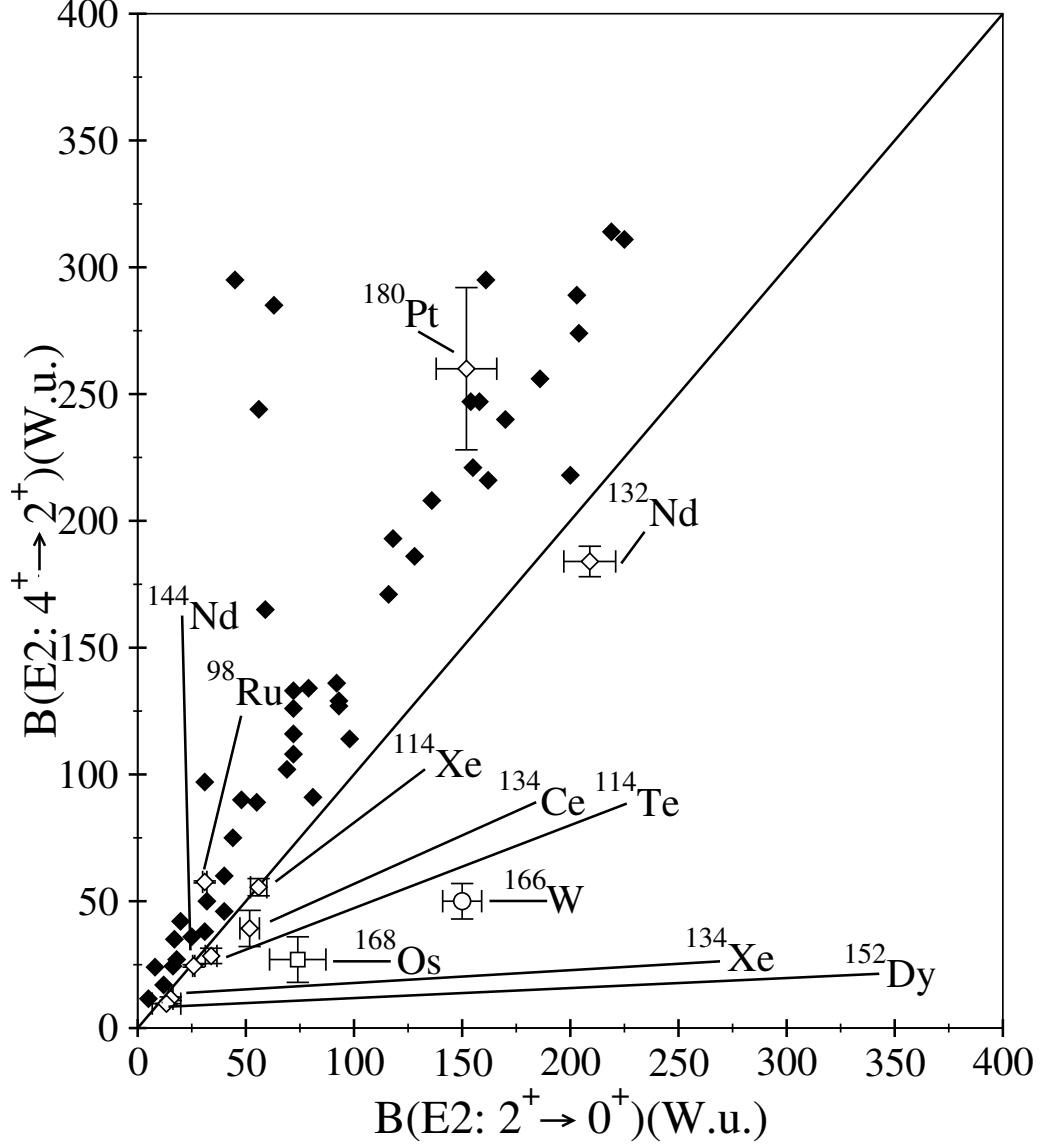


Figure 1: Experimental $B(E2)$ values for 2^+ and 4^+ excited states in non-magic nuclei in the region $40 \leq Z \leq 80$. The diagonal line represents $B(E2; 4^+ \rightarrow 2^+) = B(E2; 2^+ \rightarrow 0^+)$. Filled diamonds and $^{152}\text{Dy}_{86}$ use data from National Nuclear Data Center (NNDC). Exceptions in the figure are listed; $^{98}\text{Ru}_{54}$ [23], $^{114}\text{Te}_{62}$ [26], $^{114}\text{Xe}_{60}$ [27], $^{134}\text{Xe}_{80}$ [28], $^{132}\text{Ce}_{74}$ [29], $^{134}\text{Ce}_{74}$ [30], $^{132}\text{Nd}_{72}$ [31], $^{144}\text{Nd}_{84}$ [25], ^{166}W from present work, ^{168}Os [1] $^{180}\text{Pt}_{102}$ [24].

new features, which indicate that the Grahn *et al.* [1] measured an apparent lifetime for the 4^+ state in ^{168}Os due to the complicated structure of ^{168}Os . This thesis also reports the first lifetime measurements of excited states in ^{166}W , which also displays the $B(E2)_{4^+/2^+}$ anomaly and compares this results with existing theoretical models. It is apparent that the anomaly does not have a common origin in both nuclides.

Chapter 1

Concepts in Nuclear Physics

1.1 The Spherical Shell Model

The Liquid Drop Model (LDM) [35] was the first proposed model to describe features of the atomic nucleus. The idea of considering the nucleus as a liquid drop originated from the saturation properties of the nuclear forces and the low compressibility and well-defined surface of the nucleus. The goal of the LDM was to elucidate the relation between the binding energies and the mass of the nucleus and its results are in good agreement with the variation of binding energies as a function of mass. However, calculations from the LDM were not sufficient to clarify the empirical high separation energies around a few specific proton and neutron numbers [36]. These nucleon numbers, 2, 8, 20, 28, 50, 82 and 126, are called magic numbers and are analogous to electron shell closures in atomic physics. Experimentally observed magic numbers led nuclear physicists to the nuclear shell model [3, 4]. The shell model assumed that each nucleon moves independently in an average potential that is produced by the interaction of all the other nucleons in the nucleus. In order to reproduce these magic numbers theoretically, it was necessary to decide upon an appropriate nuclear potential with an effective interaction. The harmonic oscillator potential

was chosen for the potential term in the Hamiltonian of the Schrödinger equation in Equation 1.1, since the harmonic oscillator is simple to deal with analytically [37].

$$\begin{aligned}\hat{H}\psi &= E\psi \\ \hat{T}\psi + V(r)\psi &= E\psi \\ \frac{\hbar}{2m}\nabla^2\psi + \frac{1}{2}m\omega^2r^2\psi &= E\psi.\end{aligned}\tag{1.1}$$

In spite of this simplicity, the solution to the Schrödinger equation with the harmonic oscillator potential caused two problems. The first problem was that the harmonic oscillator potential introduced degeneracy in the energy states, for example, the $N = 4$ shell contains degenerate states with $l = 4, 2$, and 0 corresponding to the $1g$, $2d$ and $3s$ subshells. The second problem was that the harmonic oscillator potential was able to yield only the first three magic numbers. Moreover, the harmonic oscillator potential tends to infinity with increasing radius, r . However, data from nucleon scattering experiments on nuclei suggested that a realistic nuclear potential should be finite with a finite surface thickness and the radial dependence should lie between extremes of the harmonic oscillator potential and the Square-Well potential [38] as illustrated in Figure 1.1. The analytical form of the realistic nuclear potential is usually chosen to be the Woods-Saxon potential [39] defined as

$$V_{WS}(r) = \frac{-V_0}{1 + \exp(\frac{r - R_0}{a})},\tag{1.2}$$

where V_0 is the potential well depth, a is the surface diffuseness and R is the nuclear radius. The degeneracy of the levels produced by the harmonic oscillator potential was removed using the Woods-Saxon potential. However, even with this more realistic nuclear potential the magic numbers were not reproduced. There were still a few missing pieces in the description of the atomic nucleus from a theoretical

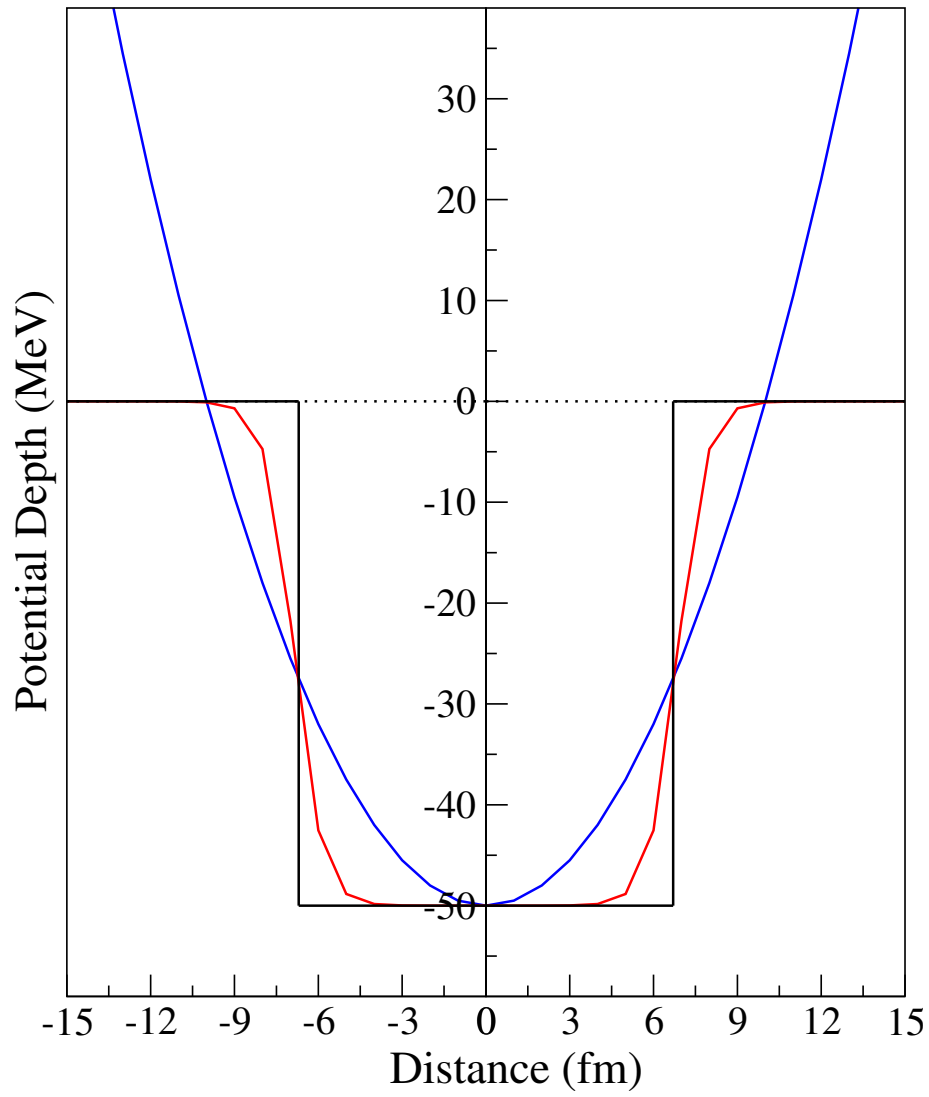


Figure 1.1: Comparison of Square-Well (black) Harmonic Oscillator (blue) and Woods-Saxon (red) potentials. The potentials are produced for illustration.

point of view. A solution was devised independently by Goeppert-Mayer and Haxel, Suess and Jensen [3, 4]. The radial part of the Schrödinger Hamiltonian needed a more radially dependent average field, so the spin-orbit interaction was introduced. The spin-orbit term is defined as

$$\begin{aligned} V_{ls} &= -V_{ls}(r)\mathbf{l}\cdot\mathbf{s}, \\ V_{ls}(r) &\propto \frac{1}{r} \frac{dV(r)}{dr}. \end{aligned} \tag{1.3}$$

The existence of the spin-orbit coupling in the Yukawa field theory of the nuclear forces leads to a strong splitting of the total angular momentum J into $J = l \pm 1/2$, hence the degeneracy of the single particle levels is broken by the spin-orbit potential. The radial component of the wave function changes smoothly with the spin-orbit force. Consequently, the main effect is that the level $J = l + \frac{1}{2}$ is lowered by a higher binding energy, whilst the $J = l - \frac{1}{2}$ is raised (see Figure 1.2), whereupon a gap occurs between the levels. The gap between levels of the same total angular momentum (J) increases with increasing angular momentum (l). Finally, a Hamiltonian using the Woods-Saxon potential and the spin-orbit coupling gives the exact magic numbers

$$H = \frac{\hbar^2}{2m} \nabla^2 + \frac{-V_0}{1 + e^{\left(\frac{r - R_0}{a}\right)}} - V_{ls}(r)\mathbf{l}\cdot\mathbf{s}. \tag{1.4}$$

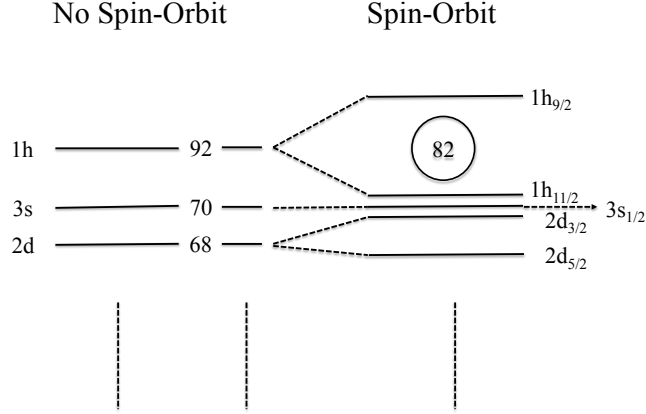


Figure 1.2: Illustration of Spin-Orbit effect on nuclear shell. As mentioned in the text, a level with higher angular momentum $1h_{11/2}$ is lowered and a level with lower angular momentum $1h_{9/2}$ is raised.

Although the spherical shell model successfully explains many nuclear features including the spins, the magnetic moments and the occurrence of isomeric states, it does not provide a satisfactory explanation of large quadrupole moments [40, 41] and the existence of rotational bands [2]. A deviation of the average mean field from spherical symmetry to a quadrupole shape with the same volume was suggested to account for the collective features of the nucleus [37]. The explanation of the nuclear structure where these phenomena are observed has followed two related models, both involving the concept of quadrupole shape. One takes into account the single-particle motion of the nucleons in a deformed field, while the other emphasises the macroscopic motions and excitations of a nucleus with a deformed shape. In the following sections, deformation parameters, microscopic and macroscopic models will be discussed.

1.2 Definition of the Nuclear Shapes

Nuclear deformation is characterised by describing the nuclear surface with a radius vector defined by spherical harmonics. The radius vector is defined as

$$R(\theta, \phi) = R_0 \left(1 + \alpha_{00} + \sum_{\lambda=1}^{\infty} \sum_{\mu=-\lambda}^{\lambda} \alpha_{\lambda\mu} Y_{\lambda\mu}(\theta, \phi) \right) \quad (1.5)$$

where R_0 is the radius of the sphere that has same volume as the deformed shape and the coefficient α_{00} ensures volume conservation. The $\alpha_{\lambda\mu}$ terms introduce deformed shapes, where both λ and μ are integers. The term λ represents the shape character ($\lambda = 1$ for a monopole, $\lambda = 2$ for a quadrupole, $\lambda = 3$ for an octupole) and μ depends on the λ value and varies from $-\lambda$ to λ . Most nuclei display some degree of quadrupole deformation. For the $\lambda = 2$ deformation, the nuclear surface is characterised by the five coefficients,

$$\alpha_{22}, \alpha_{21}, \alpha_{20}, \alpha_{2-1}, \alpha_{2-2}. \quad (1.6)$$

For an axially symmetric shape such an ellipsoid, these terms are reduced to the three terms. Since,

$$\begin{aligned} \alpha_{22} &= \alpha_{2-2} \\ \alpha_{2-1} &= \alpha_{21} = 0 \end{aligned} \quad (1.7)$$

and the nuclear deformation is described with the three deformation parameters and the three Euler angles. In the Lund convention, α_{22} and α_{20} are expressed using the polar coordinates β and γ such that

$$\begin{aligned} \alpha_{22} &= \frac{1}{\sqrt{2}} \beta_2 \sin \gamma, \\ \alpha_{20} &= \beta_2 \cos \gamma, \end{aligned} \quad (1.8)$$

where β represents the deviation of the nucleus from sphericity and γ defines the deviation from axial symmetry. The nucleus has an axially symmetric shape when $\gamma = n60^\circ$ where n is an integer. Otherwise, the nucleus is assumed a triaxial shape where the three axes have different lengths. Combining the deformation parameter for $\lambda = 2$ with the related spherical harmonics, the deformed nuclear surface is defined by

$$R(\theta, \phi) = R_0 \left(1 + \sqrt{\frac{5}{16\pi}} \beta_2 (\cos \gamma (3 \cos^2 \theta - 1) + \sqrt{3} \sin \gamma \sin^2 \theta \cos 2\phi) \right). \quad (1.9)$$

The solution to Equation 1.9 produces a prolate spheroid for $\gamma = 0^\circ, 120^\circ, 240^\circ$ and an oblate spheroid for $\gamma = 60^\circ, 180^\circ$ and 300° . In addition, if the parameter γ is fixed at any value, then Equation 1.9 yields prolate shapes for $\beta > 0$ and oblate shapes for $\beta < 0$. The Lund convention, shown in Figure 1.3, represents the framework for describing different quadrupole shapes.

1.3 Deformed Shell Model

The spherical shell model is based on the independent motion of nucleons in an average field that is produced by the nucleons themselves. The average field is spherical and provides for good descriptions for nuclei that have proton and/or neutron numbers at closed shells or nearly closed shells. However, as nucleons are added to or removed from closed shells collectivity develops and nuclei become deformed as seen in the nuclei that occupy the mid-shell regions. The single-particle states are characterised depending on the symmetry of the average field corresponding to their energy, parity, total angular momentum J and its projection m . The states with different m values are degenerate due to the spherical symmetry. However, the total angular momentum is not a good quantum number since m values are not degenerate in a deformed field. The idea of deformation [35] is able to explain

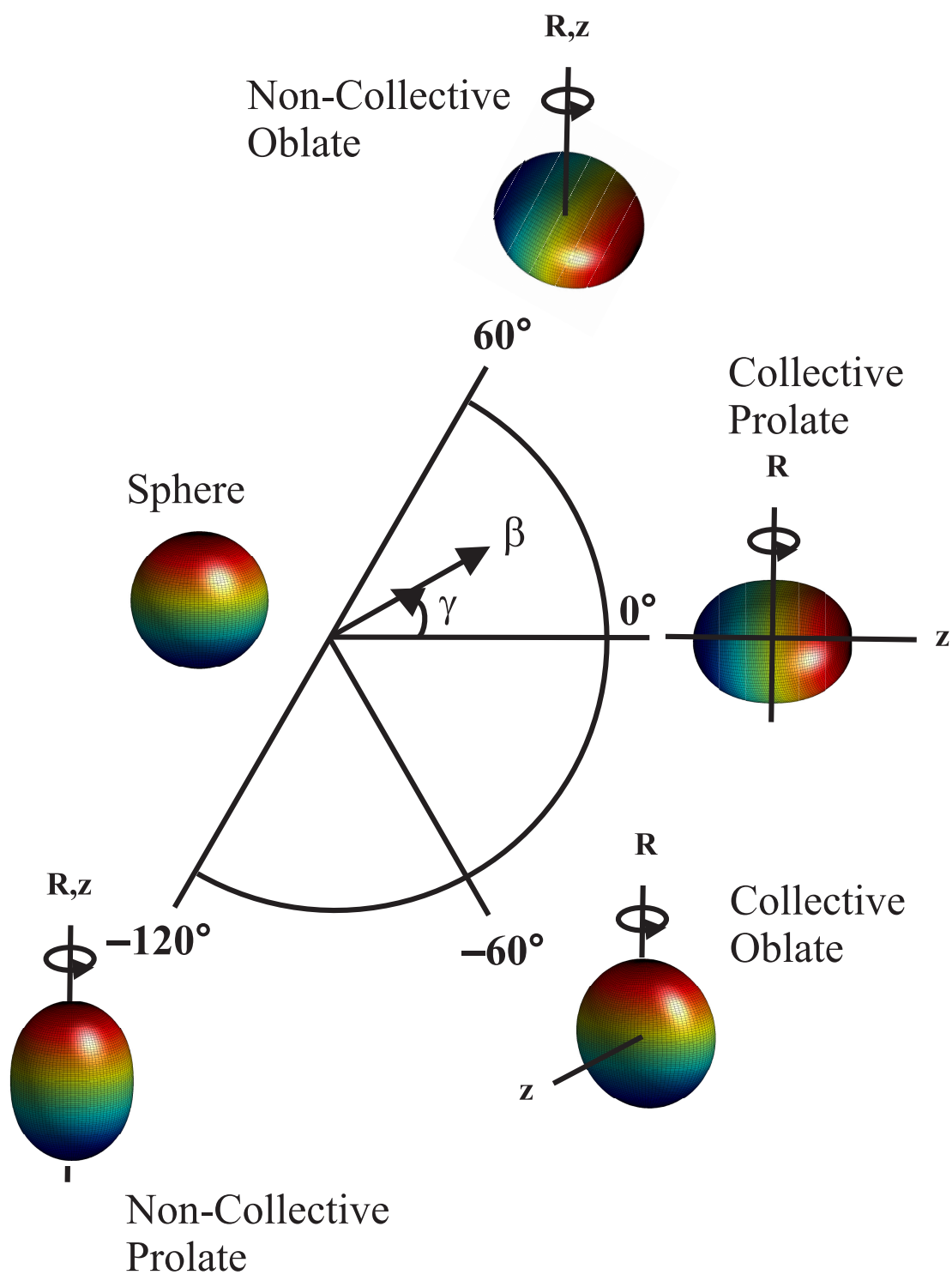


Figure 1.3: The Lund Convention for describing quadrupole shapes.

many experimental phenomena such as the large quadrupole moments and the existence of rotational bands, which cannot be explained in terms of the spherical shell model. The Woods-Saxon potential is already known to reproduce many features of the average potential. Consequently, the generalisation of the Woods-Saxon potential is natural and necessary for deformed nuclei. The deformed Woods-Saxon potential [42] is given by

$$V(r, \theta, \phi) = -\frac{V_0}{1 + \exp\left[\frac{r - R(\theta, \phi)}{a(\theta, \phi)}\right]}, \quad (1.10)$$

where a is the surface diffuseness that depends on the θ and ϕ polar angles. In deformed nuclei, the spin-orbit interaction must be taken into account as well and its generalisation is presented

$$V_{LS} = \lambda(\nabla V(r, \theta, \phi) \wedge \mathbf{p})s \quad (1.11)$$

where \mathbf{p} is the nucleon momentum. The spin-orbit coupling promotes non-sphericity and a finite surface thickness to the shape.

1.3.1 The Nilsson Potential

The harmonic oscillator is useful estimate for a general deformed potential but it needs to be modified for ellipsoidal shapes. The motion of a particle in a deformed potential using the Anisotropic Harmonic Oscillator (AHO) was described by Nilsson [43]. The AHO potential is defined as

$$V_{AHO} = \frac{1}{2}M\omega_{\perp}(x^2 + y^2) + \omega_z^2 z^2. \quad (1.12)$$

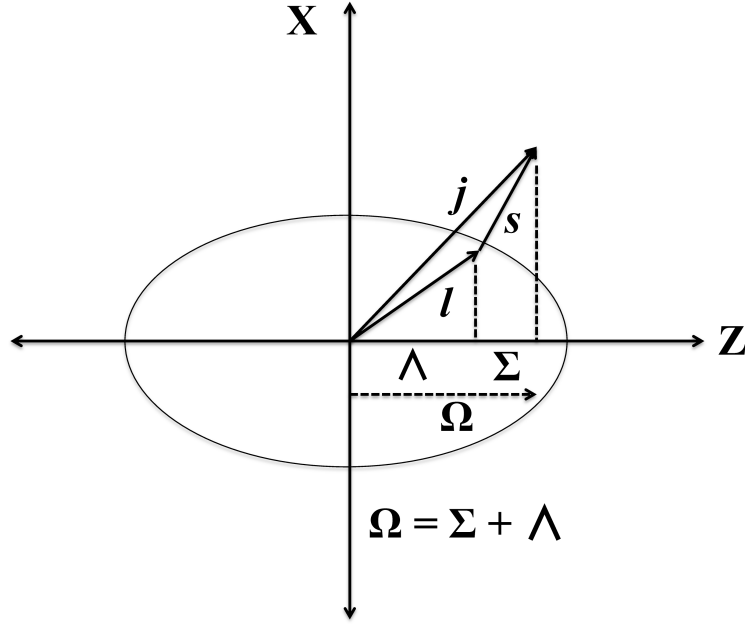


Figure 1.4: Graphical representation of the Nilsson quantum numbers.

where ω_{\perp} is defined with a deformation parameter δ that is equal to $\Delta R/R_0$.

$$\begin{aligned}\omega_{\perp} &= \omega_x^2 = \omega_y^2 = \omega_0^2(\delta) \left(1 + \frac{2}{3}\delta\right) \\ \omega_z^2 &= \omega_0^2(\delta) \left(1 - \frac{4}{3}\delta\right)\end{aligned}\tag{1.13}$$

where $\omega_0(\delta) = \overset{\circ}{\omega}_0 (1 + \frac{2}{3}\delta^2)$, $\overset{\circ}{\omega}_0 \equiv \omega_0$ for $\varepsilon = \gamma = 0$ [44].

Nilsson added the term $-2\hbar \overset{\circ}{\omega}_0 \kappa(\mathbf{l}s)$ that introduces the strength of the spin-orbit force and the angular momentum term $-\hbar \overset{\circ}{\omega}_0 \kappa \mu \mathbf{l}^2$ that flattens the potential. The Nilsson potential takes the form

$$V_{NP} = \frac{1}{2}M\omega_{\perp}(x^2 + y^2) + \omega_z^2 z^2 - \hbar \overset{\circ}{\omega}_0 \kappa(2(\mathbf{l}s) + \mu \mathbf{l}^2).\tag{1.14}$$

For the complete definition of orbitals, Nilsson describes the eigenstates of the anisotropic harmonic oscillator Hamiltonian in cylindrical coordinates with four

quantum numbers (Nilsson numbers) as illustrated in Figure 1.4,

$$\Omega^\pi[N, n_z, l] \tag{1.15}$$

where $\Omega = \Sigma + \Lambda$ is the total projection of the single-particle angular momentum j on the symmetry axis, Λ is the projection of the single-particle orbital angular momentum on the z-axis, Σ is the projection of the single-particle spin angular momentum on the z-axis, π is the parity of the state, N is the number of the oscillator shell, n_z is the number of oscillator quanta along the z-axis and l is the single-particle orbital angular momentum. A systematic comparison between the Nilsson and Woods-Saxon deformed potentials can be found in the work of Bengtsson *et al.* [45]. The asymptotic quantum numbers and corresponding selection rules are employed in both the Nilsson and deformed Woods-Saxon potential.

1.4 Collective Motion

Collectivity is determined by the coherent movement of a large number of the nucleons [2]. The correlations between nucleons in the nucleus give rise to a spherical equilibrium shape or deformed equilibrium shape [46]. The spherical equilibrium shape originates when the short-range inter-nucleon forces show a tendency to couple the particles in pairs to produces $J = 0$; this is the pair coupling scheme which leads to nuclear vibration. Alternatively, the deformed equilibrium shape occurs when each nucleon tends to align its orbit with the average field produced by all other nucleons; this is the aligned coupling scheme which leads to nuclear rotation.

1.4.1 Nuclear Vibration

The nuclear vibrations are oscillations in the shape of nucleus with a constant density [47]. While the average shape is spherical, the instantaneous shape is not. A departure from the spherical shape is characterised by the time-dependent radius vector given by

$$R(\theta, \phi, t) = R_0 \left(1 + \sum_{\lambda=1}^{\infty} \sum_{\mu=-\lambda}^{\lambda} \alpha_{\lambda,\mu}(t) Y_{\lambda,\mu}(\theta, \phi) \right), \quad (1.16)$$

where the $R(\theta, \phi, t)$ is the radius of surface at angles (θ, ϕ) and time t . The parameters $\alpha_{\lambda\mu}$, λ and μ have already been described in Equation 1.9. The $\lambda = 1$ mode is related to an oscillation around a fixed point in the laboratory system [48]. The constituents of the nucleus in the $\lambda = 1$ mode move either together as a group causing no changes in the internal structure of the nucleus (the isoscalar ($T = 0$) dipole mode) or neutrons and protons oscillate in opposite directions (the isovector ($T = 1$) dipole mode). The $\lambda = 2$ mode defines a quadrupole oscillation of the nucleus. A positive quadrupole deformation leads to a prolate shape, while a negative quadrupole deformation leads to an oblate shape. The nuclear shape oscillates about a sphere from oblate to prolate shapes in the $\lambda = 2$ mode. The vibrational model makes a few predictions that can be examined experimentally. If the equilibrium shape is spherical, the time averaged quadrupole moment for the first 2^+ state ought to be zero. The common features of the nuclear vibrators in even-even nuclei are that the ground state spin $J^\pi = 0^+$, in most cases $J^\pi = 2^+$ is the first excited state and the excitation energy ratio $E(4^+)/E(2^+)$ is approximately 2.

1.4.2 Nuclear Rotation

Nuclear rotation requires existence of a non-spherical equilibrium shape [2] since, one cannot observe rotational motion where the symmetry and rotation axes coincide.

As a consequence only deformed nuclei where the rotation axis is perpendicular to the symmetry axis can rotate collectively. For a permanent deformation, the lowest possible shape component is the $\lambda = 2$ quadrupole distortion. The surface of the rotational nucleus for the $\lambda = 2$ mode is determined by a time-independent radius vector,

$$R(\theta, \phi) = R_0 \left(1 + \beta Y_{2,0}(\theta, \phi) \right), \quad (1.17)$$

where β is the deformation parameter and corresponds to the eccentricity of the ellipsoidal shape. The parameter β is defined as

$$\beta = \frac{4}{5} \sqrt{\frac{\pi}{5}} \frac{\Delta R}{R_0}, \quad (1.18)$$

where ΔR is the difference between the semi-major and semi-minor axes of the ellipse.

The kinetic energy of a rotating nucleus is

$$E = \frac{\hbar^2}{2\mathcal{J}} I(I+1) \quad (1.19)$$

where \mathcal{J} is the moment of inertia and I is the total angular momentum of the excited states. This expression gives the values

$$\begin{aligned} E_{2+} &= \frac{\hbar^2}{2\mathcal{J}} 6 \\ E_{4+} &= \frac{\hbar^2}{2\mathcal{J}} 20 \\ E_{6+} &= \frac{\hbar^2}{2\mathcal{J}} 42 \end{aligned} \quad (1.20)$$

and so on. Thus, the energy ratio E_{4+}/E_{2+} is equal to 3.33 for a perfect rotor. The ratio is one the most famous results of the rotational model and is a common sign of rotational motion and deformation [37].

1.5 The Features of Gamma Decay

1.5.1 The Kinematics of Gamma Decay

An excited nucleus can decay to a lower energy state via γ emission or internal conversion [36]. The γ -decay energy is determined by the masses of the initial and final states as

$$M_i c^2 = M_f c^2 + E_\gamma + E_R \quad (1.21)$$

where E_γ is the emitted γ -ray energy and E_R is the recoil energy of the nucleus. Linear momentum conservation implies that $P_R = E_\gamma/c$, where P_R is the momentum of the recoil and E_γ/c is the momentum carried by the γ ray. The recoil energy is given by

$$E_R = \frac{E_\gamma^2}{2M_f c^2}. \quad (1.22)$$

For a 1 MeV γ -ray energy, a mass $A = 100$ recoil has a energy of about 5 eV. This value is much smaller than the gamma-ray energy and can be neglected. Thus, the γ -ray energy is determined to be

$$E_\gamma = (M_i - M_f) c^2. \quad (1.23)$$

1.5.2 Electromagnetic Transition Rates

A real stationary state lives forever and the expectation value of its energy is constant in time. The Heisenberg relationship implies that when $\Delta E = 0$, Δt goes to infinity. Therefore, a state with a certain excitation energy survives forever and its lifetime is hindered against decay. Let us assume the system experiences a weak perturbing potential V' , in addition to the original potential V . The solutions of the Schrödinger equation for V and V' give eigenvalues similar, but not equal to solutions for the original potential V . The additional weak potential V' allows the system to make

transitions between the eigenstates ψ_n for $(V + V')$. Energy must be conserved during the transitions and if the final state energy is lower than the initial state, the energy difference between the states often appears as a γ decay. A non-stationary state has a comparatively shorter lifetime (τ) or half-life ($t_{1/2}$) than a stationary state. That means it has an average lifetime before decay via a γ ray or internal conversion. The non-stationary state has an uncertainty in its energy ΔE , often given as a width Γ . According to the Heisenberg relation, the lifetime of the state is constrained by

$$\Gamma \cdot \tau \geq \hbar/2. \quad (1.24)$$

In the γ decay from initial state i to final state f , the number of decays per unit is called decay probability or transition probability and is denoted by T [49]. The transition probability is given as

$$\mathbf{T}(E\lambda; i \rightarrow f) = \frac{1}{\tau} = \frac{8\pi}{\hbar} \frac{\lambda + 1}{\lambda[(2\lambda + 1)!!]^2} k^{2\lambda+1} B(\lambda; i \rightarrow f), \quad (1.25)$$

where $k = E_\gamma/\hbar c$, E_γ is the energy of emitted photon, λ is multipolarity of the emitted photon and $B(\lambda)$ is the reduced transition rate for electric or magnetic transitions. The electric reduced transition rate, $B(E\lambda)$ can be given in terms of experimentally measurable quantities as

$$B(E\lambda; i \rightarrow f) = \frac{F_\lambda^{(E)}}{(E_\gamma)^{2\lambda+1} \tau} e^2 \cdot b^\lambda \quad (1.26)$$

For an electric quadrupole transition, the internal conversion coefficient α_γ must be taken into account [50] and the reduced transition probability $B(E2)$ becomes

$$B(E2) = \frac{0.0816}{(E_\gamma)^5 \tau (1 + \alpha_\gamma)} e^2 b^2 \quad (1.27)$$

For magnetic transition rates, a detailed explanation can also be found in Reference [50]. The electric quadrupole radiation is of special interest. Since the ground state for even-even nuclei is 0^+ , the first excited 2^+ state only decays via electric quadrupole transitions (E2). In order to define a universal magnitude for the quantitative measurements of E2 rates, the $B(E2)$ value can be used to decide whether a given value is collective or not. The Weisskopf unit (W.u.) or e^2b^λ are used as a unit for $B(E2)$. The relation between W.u. and e^2b^2 is given as

$$1W.u. = (5.94 \times 10^{-6})A^{4/3}e^2b^2. \quad (1.28)$$

For $A = 160$, $1 W.u. = 0.00515e^2b^2$. For transition rates between rotational states of heavy nuclei, $B(E2)$ is considerably larger than $1 W.u.$ and, in some cases, can display values greater than $1000 W.u.$ In spherical vibrational nuclei typical $B(E2)$ values are $\sim 10 - 50 W.u.$ The general behaviour is that $B(E2)$ takes relatively small values near closed shells and high values near the mid shell regions [37].

1.5.3 Selection Rules for γ -Ray Transitions

For a γ ray transition, the first selection rule is that there are no $E0$ multipoles. According to the electric tensor operator in Equation 1.29, the electric moment is constant when $\lambda = 0$. Two different nuclear states cannot be connected by a constant. However, $E0$ transitions can occur via internal conversion instead of γ decay.

$$Q_{\lambda\mu} = \zeta^{E\lambda} \sum_{j=1}^A e(j)r_j^\lambda Y_{\lambda\mu}(\Omega_j) \quad (1.29)$$

where $\zeta^{E\lambda}$ is the phase factor, $e(j)$ is the electron charge and λ is the multipolarity. The γ transitions are categorised according to their multipolarity: $\lambda = 0$ is monopole, $\lambda = 1$ is dipole, $\lambda = 2$ is quadrupole, $\lambda = 3$ is octupole etc. For the selection of

Table 1.1: Multipolarities of γ transition between an initial (I_i) and final states (I_f). For $\Delta\pi = \text{no}$, then even electric and odd magnetic transitions are observed. For $\Delta\pi = \text{yes}$, then odd electric and even magnetic transitions are observed.

λ	1	2	3	4	5
$\pi_i\pi_f = -1$	E1	M2	E3	M4	E5
$\pi_i\pi_f = +1$	M1	E2	M3	E4	M5

γ -ray transitions, the triangular condition in Equation 1.30 for angular momenta J_i and J_f of nuclear states is applied

$$|J_f - J_i| \leq \lambda \leq J_f + J_i \quad (1.30)$$

the parity conservation selection rule is then applied

$$\pi_i\pi_f = \begin{cases} (-1)^\lambda & \text{for E}\lambda \\ (-1)^{\lambda-1} & \text{for M}\lambda \end{cases} \quad (1.31)$$

The combination of the triangular condition and the parity selection rule leads to the classification of electromagnetic transitions in Table 1.1. For instance, for a $2^+ \rightarrow 2^+$ transition may proceed via γ rays of multipolarity $M1$, $E2$, $M3$ and $E4$ transitions. Lower multipolarities are favoured although $E2$ transitions often compete with the $M1$ transitions [51].

1.6 Natural Decay Law and Bateman Equations

The discovery of radioactivity in 1896 was followed by several years of research to understand the decay nature of radioactivity. It was found that this is inherently statistical, that is, it is not possible to guess an exact time for any given atom to disintegrate [49]. Rutherford and Soddy formulated the first decay law for radioactive materials. For a radioactive substance, the disintegration rates characterise the radioactivity. The probability of such a nucleus decaying within a time interval dt

is given by λdt , where λ is the decay probability. If N is the number of radioactive nuclei at given time $t = 0$, then the number of nuclei decayed is given by the following expression

$$dN = -\lambda N dt. \quad (1.32)$$

The integration of this expression results in

$$N(t) = N_0 e^{-\lambda t}, \quad (1.33)$$

which is known as the radioactive decay law. A lifetime term can be introduced as the time in which half of the original radioactive material decay, i.e. for $t = t_{1/2}$, $N = N_0/2$. The relation between half-life and transition rate is $t_{1/2} = \ln 2 / \lambda$ [52]. At this stage, it is helpful to define a mean lifetime term, which is the average time that a nucleus exists before it decays, $\tau = 1/\lambda$ [49]. The number of decays is given mathematically by

$$\left| \frac{dN}{dt} \right| = \lambda N_0 e^{-\lambda t} \quad (1.34)$$

$$A = A_0 e^{-\lambda t} \quad (1.35)$$

The number of decay per second is called the activity A which is defined by $\lambda N(t)$, where λN_0 is the activity A_0 at time $t = 0$. Units often used for activity [52] are

- 1 Curie (Ci) = 3.7×10^{10} disintegration/s
- 1 Rutherford (Rd) = 10^6 disintegration/s
- 1 Becquerel (Bq) = 1 disintegration/s

Typical radioactive sources used in laboratories have activities that vary from microcuries to millicuries [49]. The time evolution of decay sequences [53] are controlled by a set of first-order differential equations. The first-order differential equations are called the Bateman Equations. Determination of the nuclide activity using Bateman

equations are done as follows

$$\frac{dN_i}{dt} = \lambda_{i-1}N_{i-1} - \lambda_i N_i, \quad (1.36)$$

where λ_i stands for the decay constant of i th nuclide. If all daughters have a certain concentration at $t = 0$, then the concentration of n th nuclide after time t is calculated by solving the differential equation

$$N_n(t) = \frac{N_1(0)}{\lambda_n} \sum_{i=1}^n \lambda_i \prod_{j=1, j \neq i}^n \frac{\lambda_j}{\lambda_j - \lambda_i} e^{-\lambda_i t} \quad (1.37)$$

The application of Equation 1.37 in the present data analysis will be shown in later sections.

Chapter 2

Experimental Methodology

This thesis explores the structure of the neutron-deficient ^{168}Os and ^{166}W nuclei. This chapter concerns the reaction mechanism and apparatus employed at the Accelerator Laboratory of the University of Jyväskylä. The facility consists of JUROGAM Ge-detector array coupled to the RITU [54] gas-filled separator and the GREAT [55] spectrometer at the focal plane of RITU. For the lifetime measurements, a plunger Differential Plunger for Unbound States (DPUNS) device [56] is mounted to the target position of the JUROGAMII Ge-detector array. The reaction system, the experimental set-up and the experimental techniques used in order to expand level scheme of ^{168}Os and measure lifetimes of the excited states in the nuclide ^{166}W are discussed in this chapter in detailed.

2.1 Fusion Evaporation Reactions

At present, the most efficient method for producing neutron-deficient nuclei is via a fusion-evaporation reaction [57] using a stable target and beam. Figure 2.1 shows a schematic diagram of the fusion-evaporation mechanism in terms of the excitation energy and angular momentum. The beam is accelerated to an energy to over-

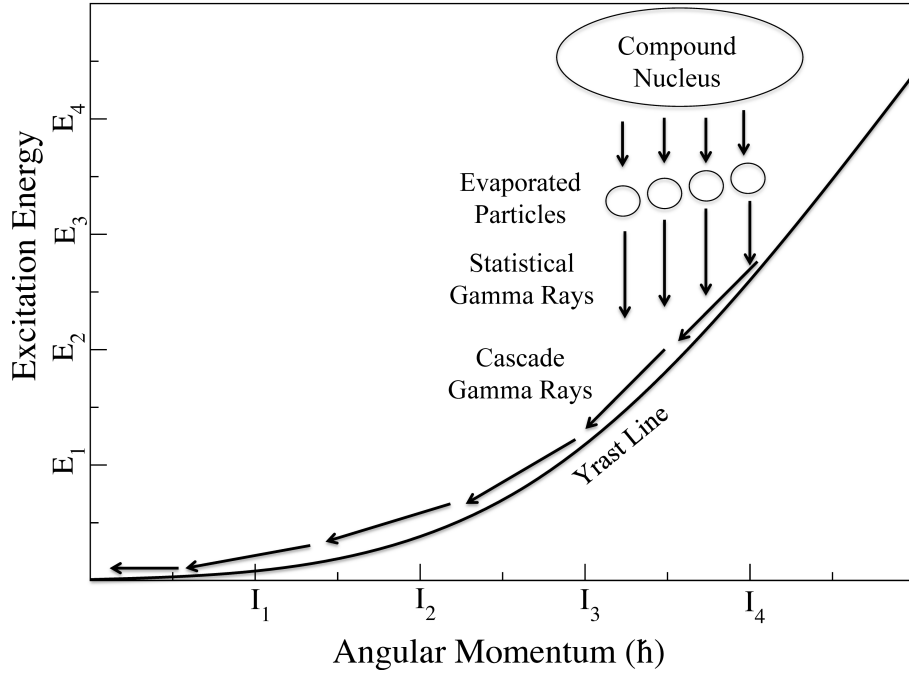


Figure 2.1: A schematic diagram of the process involved in the de-excitation of a compound nucleus formed in a fusion-evaporation reaction.

come the Coulomb barrier fusing projectile and target nuclides to form a compound nucleus. The mechanism of a fusion-evaporation reaction is outlined below;

- Projectiles are accelerated to an energy E_p by a particle accelerator in order to overcome the Coulomb barrier given in Equation 2.1 of the target nuclei defined as

$$E_{Coulomb} = \frac{e^2}{4\pi\epsilon_0} \frac{Z_t Z_p}{(r_t + r_p)}, \quad (2.1)$$

where, Z_p (Z_t) and r_p (r_t) are proton number and radius of the projectile(target) nucleus, respectively.

- The beam and target fuse on a time scale of 10^{-20} seconds and produce a highly excited rotating compound nucleus.
- The compound nucleus may either fission or emit particles such as protons, neutrons or alphas to lose energy. In case of the particle evaporation, each emitted particle takes away at least its binding energy of ~ 8 MeV from the

Table 2.1: The JUROGAMII array specifications. Rings are used as labels for specific angular groups of detectors. The angles are defined with respect to the beam direction and all angles are midpoint angles.

Rings	Angle	Detector Type	Number of Detectors
1	158°	Phase I	5
2	134°	Phase I	10
3	105°	Clovers	12
4	76°	Clovers	12

compound system, but not much angular momentum. Following particle emission, the residual nucleus is left with low excitation energy but high angular momentum. Particle emission continues until threshold energy is reached.

- Statistical γ -rays continue to de-excite the nucleus. The emission of statistical transitions brings the evaporation residue close to the yrast line.
- Along the yrast line cascade γ -ray transitions dominate the de-excitation of the nucleus. E2 transitions dominate and are favoured at this stage due to their transition probability.

Finally, the residual nucleus reaches a low-lying isomeric state or the ground state and will undergo electromagnetic emission or radioactive decay.

2.2 The JUROGAMII γ -ray spectrometer

Gamma rays emitted following a nuclear reaction can be detected at the target position using large arrays of spectrometers such JUROGAMII. The JUROGAMII spectrometer is an array of Compton-suppressed hyper-pure germanium (HP-Ge) detectors with a total photopeak efficiency 5.8 % and energy resolution 2 keV at 1.3 MeV. The array consists of 15 Phase I-type [58] and 24 Clovers [59] detectors. The angular configuration of detectors according to the angle relative to beam direction is given in Table 2.1.

The Phase 1 detectors are large coaxial n-type germanium crystals of 70 mm length and 69-75 mm diameter. The Ge crystals are tapered over front 3 cm of their length with a cone angle of 5.7° in order to provide a uniform electric field across the crystal. Clover detectors are segmented detectors comprising four HPGe crystals in a four-leaf clover configuration. Each clover detector is composed of four coaxial n-type Ge detectors of 50 mm diameter and 70 mm length. The clover detectors are placed in the array at angles near to 90° relative to the beam direction. The granularity of the composite detector minimises the Doppler broadening of the γ rays emitted from recoiling nuclei. The Doppler broadening effect must be reduced since it reduces the resolving power of the array.

2.2.1 Gas-Filled Recoil Separators

Gas-filled recoil separators are efficient tools in the spectroscopy of heavy neutron-deficient nuclei and provide a high transmission efficiency with typical values around 50% [60] when asymmetric reactions are employed. In a gas-filled separator a relatively heavy ion undergoes charge exchange collisions as it traverses a gas at low pressure. All reaction products recoiling out of the target with the same velocity and direction have almost identical trajectories that are independent of the original charge state and the common average trajectory is determined by the average charge state [54]. The interaction between recoils with an average charge state and the homogeneous magnetic field produced by dipole magnets is given by [61]

$$eq_{ave}vB = mv^2/r, \quad (2.2)$$

$$Br = mv/eq_{ave} = mv/(ev/v_0)Z^{1/3}, \quad (2.3)$$

where Br is the magnetic rigidity, v is the velocity of ions and v_0 represents the Bohr velocity $v_0 = 2.19 \times 10^6 \text{ m/s}$. The magnetic rigidity is simplified as

$$Br = 0.0227A/Z^{1/3}, \quad (2.4)$$

where A is the mass number and Z is the proton number of the ions. Equation 2.4 shows that the rigidity is independent of the original charge state and velocity distribution.

2.2.2 The Recoil Ion Transport Unit (RITU)

The RITU [54] gas-filled separator (see Figure 2.2) is situated at the University of Jyväskylä. The standard magnet configuration of many gas-filled separators is DQQ. However, RITU has a $Q_v D Q_h Q_v$ magnet configuration [60] with a total length of 4.8 m. The first quadrupole matches the recoil cone from the target to the acceptance of the dipole magnet. For the reactions used in this thesis, the flight time through RITU to the DSSD at the focal plane is $\sim 1 \mu\text{s}$ and a transmission efficiency of 50% is typical assuming the Helium filling gas is at a pressure around 0.6 mbar [62].

2.3 The Gamma Recoil Electron Alpha Tagging (GREAT) Spectrometer

The GREAT spectrometer [55] in Figure 2.3 was built to study the decay properties of reaction products implanted at the focal plane of a recoil separator such as RITU. GREAT is composed of gas, silicon and germanium detectors. These detectors are optimised in order to detect the implantation of the reaction products and, furthermore, to relate those spatially and temporally with any subsequent decay such as protons, α , β particles, γ and X-rays or conversion electrons. GREAT can be run

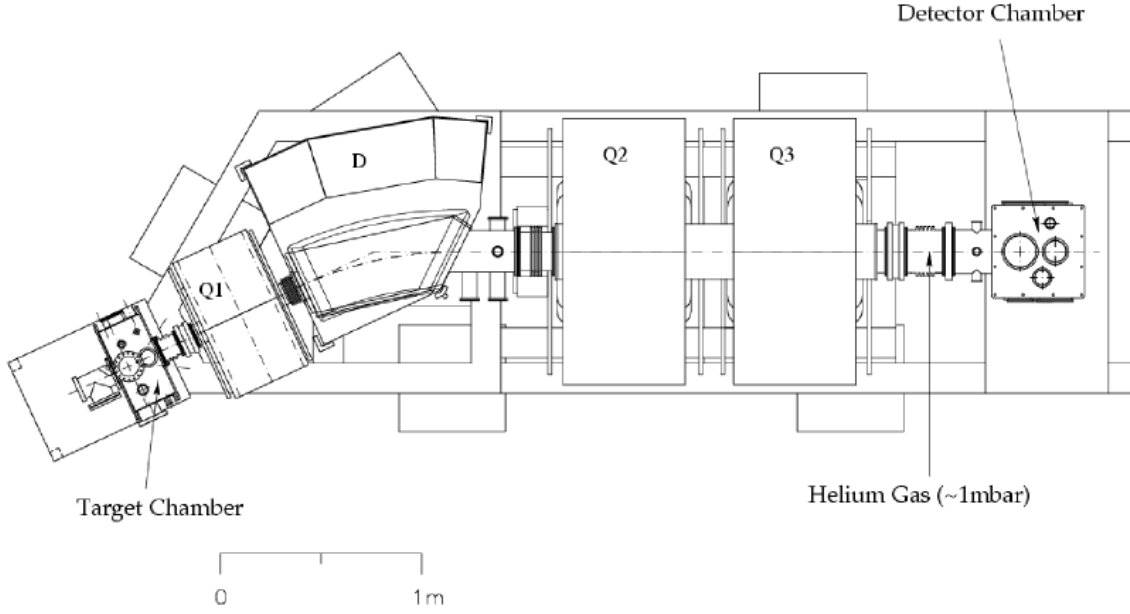


Figure 2.2: A schematic plan view diagram of the RITU gas-filled separator [61].

either as a stand-alone device to study decay properties at the focal plane or may be used in conjunction with a γ -ray spectrometer located at the target position to provide a selective radioactive tag for in-beam studies.

Multiwire Proportional Counter (MWPC)

The MWPC is placed at the entrance of GREAT. It has an 131mm x 50 mm open space with a central vertical support rod for the thin mylar foil entrance and exit windows. The entrance window prevents mixing of the isobutane gases in the MWPC and the low-pressure helium gases in the RITU separator. The exit window also separates the isobutane gas and the vacuum where the other GREAT detectors are deployed. The main function of the MWPC used in conjunction with the DSSD, is to discriminate between fusion-evaporation reaction products and their subsequent decays.

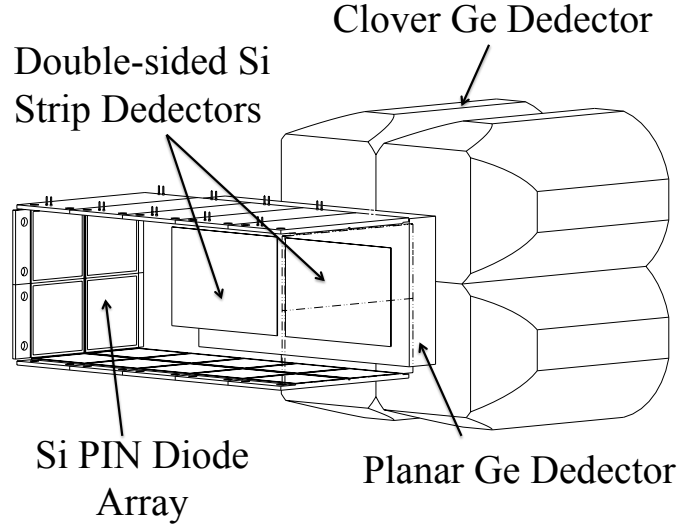


Figure 2.3: A schematic drawing of the Gamma Recoil Electron Alpha Tagging (GREAT) Spectrometer [55].

DSSD

Each DSSD has an active area of $60 \text{ mm} \times 40 \text{ mm}$ and a thickness of $300 \mu\text{m}$. It is divided into 1 mm strips in the X and Y directions in order to provide 60 vertical and 40 horizontal strips resulting in a total of 4800 pixels. There is a 4 mm gap between the two DSSDs, which gives an estimated typical recoil collection efficiency of 85%. The DSSDs are in use in order to measure energies of implanted recoils and their subsequent charged particle decays. Time-of-flight (TOF) information from the MWPC to DSSDs is generated by using the time signals in the MWPC and DSSDs to provide a clean separation between fusion products and unreacted beams.

Pin Diodes

Conversion electrons and back-scattered α -particles are detected by an array of 28 silicon PIN diodes, which are mounted in a perimeter perpendicular to the front face of the DSSDs.

Planar Ge Detector

X-rays and low-energy γ rays are measured with a double-sided germanium strip detector placed just behind DSSDs. The rectangular planar Ge detector crystal has an active area of 120 mm \times 60 mm and is 15 mm thick. The crystal of the planar detector is electrically segmented into 12 horizontal and 24 vertical strips. It can also be used to detect high-energy β particles (≥ 2 MeV).

Clover Detector

A clover germanium detector mounted outside of the vacuum chamber is used to measure high-energy γ rays. The GREAT clover has four Ge crystals with a 70 mm diameter and 105 mm length. Each crystal has four-fold segmentation. A BGO suppression shield surrounds the GREAT clover detector in order to suppress Compton scattered γ rays.

2.4 Data Acquisition

In-beam spectroscopic studies of exotic nuclei near the proton drip line employ fusion-evaporation reactions. The γ rays emitted from all the reaction products are detected by the γ -ray spectrometer located at the target position. In some cases only a small fraction of the detected γ rays are generated by the nucleus of interest and the γ -ray spectra are dominated by emissions from other reaction channels and fission products. Therefore, several methods have been devised in order to hinder miscorrelation between the in-beam γ rays and the nuclei of interest. Investigation of γ rays in delayed coincidence with fusion-evaporation nucleus (recoil gating) implanted in the GREAT DSSDs is the main method used in this work. In order to achieve accurate temporal correlations the Total Data Readout (TDR) acquisition system [63] time stamps each detector signal independently relative to a global

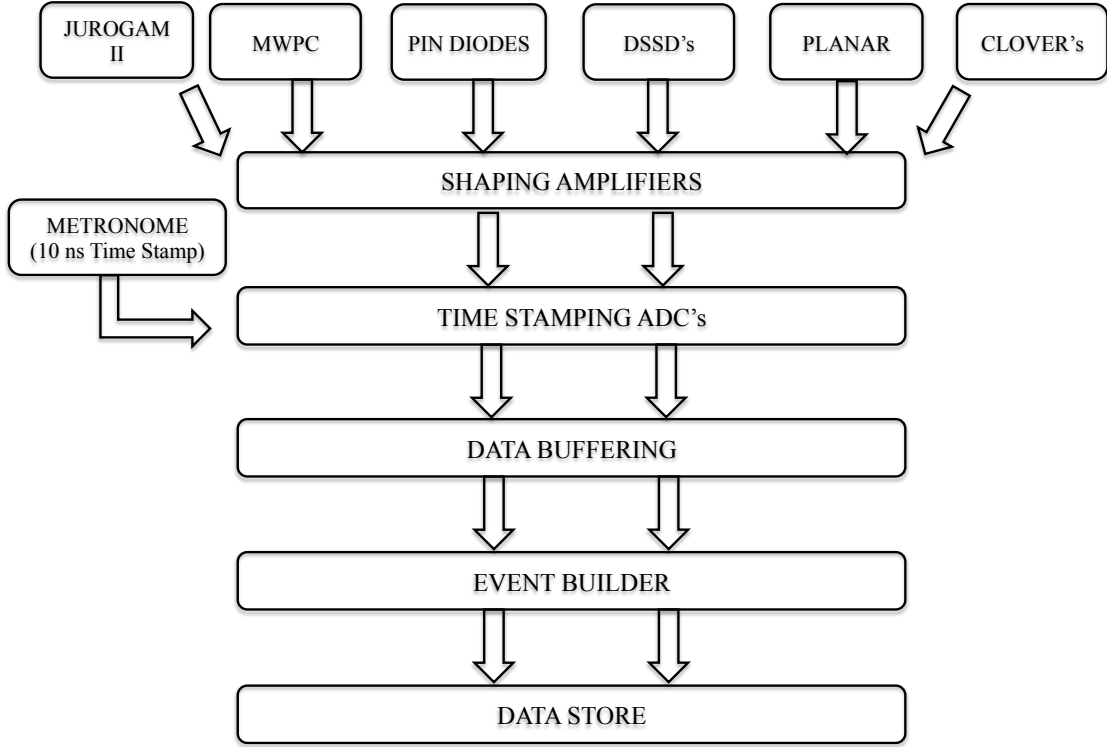


Figure 2.4: Schematic diagram of the TDR system's electronics and data acquisition adopted from Ref. [63]

100-MHz clock with a 10 ns precision. The TDR principle is shown schematically in Figure 2.4. In the TDR system, the timing and energy signals are taken from shaping amplifier. The analog-to-digital converter ADCs cards read the information and timestamp the data. The metronome controls the clock distribution and preserve the synchronisation of ADCs. The data is later merged into a time ordered stream and sent into the event builder. The event builder will pre-filter the data for any pre-set software trigger conditions and reconstruct the events using spatial and temporal correlation.

2.4.1 Recoil Gating

Recoil gating methods are vital and provide correlations between fusion-evaporation reaction products and prompt γ rays emitted at the target position [64]. The recoiling nuclei are transported through the RITU recoil separator and distinguished from unreacted beam before being implanted into the detectors at the focal plane of the GREAT spectrometer. A clear separation of fusion-evaporation products from unreacted beam is done by combining the timing and energy loss signals of the MWPC used in conjunction with the DSSD signals. The time difference of the MWPC and DSSD signals for same event is called time-of-flight (TOF). A two dimensional spectrum constructed from the energy loss in MWPC and TOF information is shown in Figure 2.5. The γ rays are correlated with the fusion-evaporation products by setting a two-dimensional gate on the identified recoil distribution. Although the method makes it possible to relate γ rays with recoils, it cannot show the difference between specific exit channels since no isotope or mass identification is possible at the focal plane of RITU. Cases like ^{166}W and ^{168}Os that are studied in this work are good examples of what can be achieved by the recoil gating technique.

2.5 The DPUNS Plunger

The Differential Plunger for Unbound States (DPUNS) [56] shown in Figure 2.6 is based on the Köln Plunger design [65]. It was designed and commissioned by a collaboration between the Universities of Jyväskylä, Liverpool and Manchester. DPUNS operates in both vacuum and dilute-gas environments. The plunger apparatus is employed for measuring lifetime of the excited states using the recoil distance method. The target and degrader foils are attached to aluminium rings are located in dedicated target chamber. The target and degrader are adjusted until parallel to each other by stretching using screws on conical support frames. The degrader foil

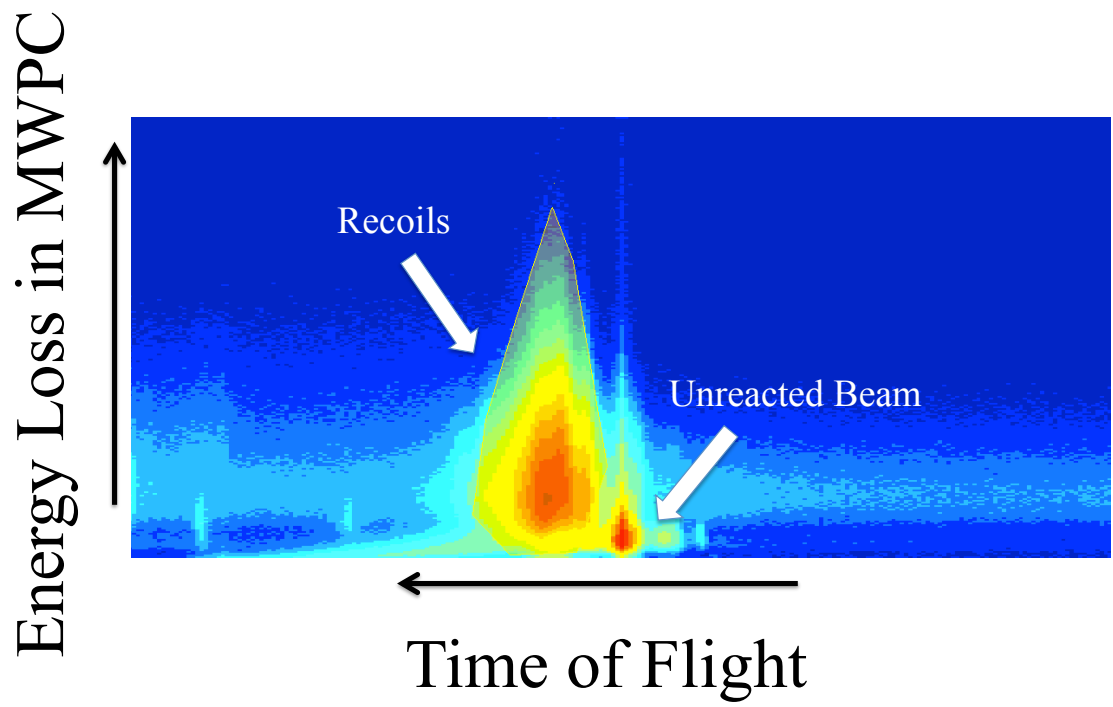


Figure 2.5: A two-dimensional spectrum present the separation of recoils from the scattered beam. The time difference between the timing signals in MWPC and DSSD's (TOF) on the x-axis and energy loss signal in MWPC on the y-axis. The shaded area defines recoils.

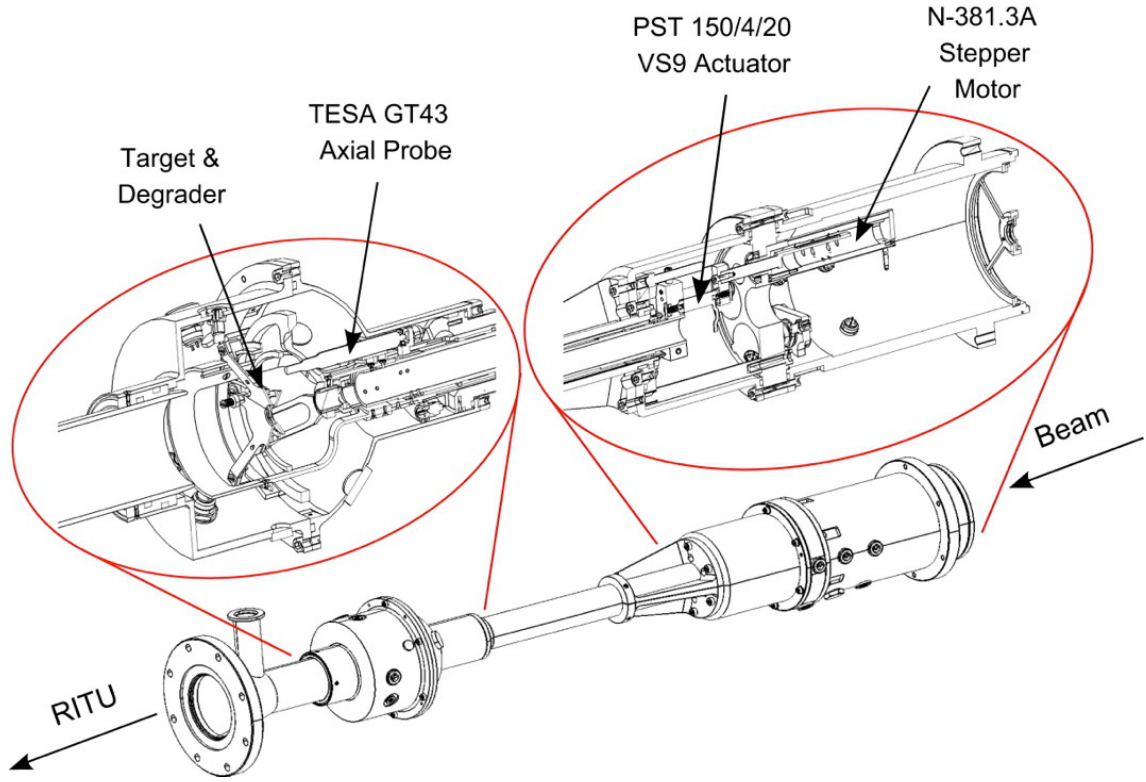


Figure 2.6: A schematic drawing of the DPUNS plunger device [56] Target and degrader are placed into the target chamber. Stepper motor is employed to set the target-to-degrader distances. An actuator keep distance in balance during the beam bombardment. TESA is used to calibrate the induced target voltage.

was kept at a fixed position while the target is moved relative to the degrader. A stepper motor is used to change target-to-degrader distance by moving the target. A piezoelectric actuator crystal is attached to the target holder in order to balance the target-to-degrader distance during beam bombardment. A TESA GT43 axial probe is used for calibrating the induced target voltage to maintain distances. The target-to-degrader distances were continuously recorded for each experimental run. A detailed explanation can be found in the paper written by Taylor *et al.* [56]. DPUNS has been used to measure the lifetimes of excited states in ^{166}W reported in this thesis.

2.6 Lifetime Measurement Techniques

Lifetime measurements of excited states provide fundamental information regarding nuclear structure. Lifetimes can be used to calculate transition probabilities, which are dependent on the associated electromagnetic matrix elements. Comparisons of those matrix elements with the predictions of nuclear models provide a critical test of the model formalism and its relevance in describing the structure of the nucleus. The lifetime of an excited state can be measured by different experimental methods [66]. To measure the lifetime of an excited state it has to be populated using a nuclear reaction that is chosen according to aims of the measurement. Once the excited state is populated it will remain excited for a mean lifetime τ , which is related to width Γ of the state. The relation is given by

$$\Gamma\tau = \hbar, \quad (2.5)$$

where Γ is the decay width, τ is the mean lifetime and \hbar is the Planck constant. The methods are divided into direct and indirect methods that measure the lifetime or the width, respectively. Figure 2.7 shows the different lifetime measuring techniques and the range of their applicability.

2.6.1 The Recoil Distance Doppler Shift Method (RDDS)

In this work, the Recoil Distance Doppler Shift technique was employed. The RDDS is one of the direct methods of measuring lifetimes and is capable of measuring mean lifetimes in the 10^{-8} and 10^{-12} s range. The earliest measurements with this technique were performed by Jacobsen *et al.* and Devons *et al.* [68, 67].

An excited recoiling nucleus is formed at $t = 0$ with an initial velocity v in a nuclear reaction. The nucleus will move a distance $d = vt$ in its excited state before it emits γ rays. The mean lifetime τ of a nuclear state is related to the time

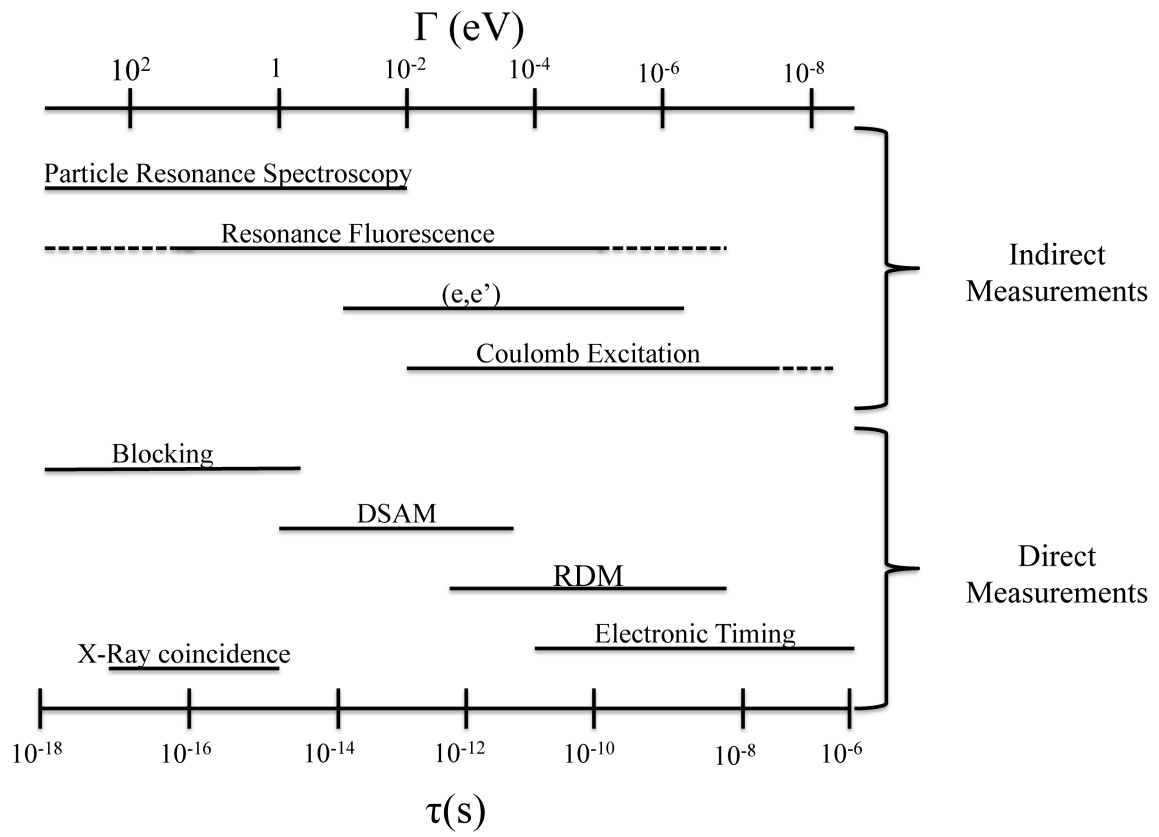


Figure 2.7: Chart adopted from Ref. [67] which shows the different lifetime measuring techniques over the different time ranges.

needed to travel a certain distance d . The RDDS method utilises a plunger device (see Figure 2.6) in which a metal plate or degrader is placed at a short distance away from the target. The γ -ray peak is split into Doppler-shifted or degraded components depending on the point of emission according to

$$E = E_0 \left[1 + \frac{v}{c} \cos \theta \right], \quad (2.6)$$

where E_0 is the energy of the γ ray emitted by nuclei at rest, v is the velocity at the point of emission and θ is the angle of the observation of γ ray relative to the recoil direction. The intensity of the Doppler-shifted γ ray is related the number of γ decays that occur before degrader. Similarly, the intensity of the degraded component is related to the number of γ rays that are emitted at an attenuated velocity \bar{v} after being slowed down in the degrader. Figure 2.8 shows the convention for labelling γ -ray components as shifted or degraded according to emission time. The intensity of shifted and degraded component depend on the target-to-degrader distance [68, 67] and are expected to change in the region of sensitivity. By measuring the relative intensity of these components one can extract the lifetime using a technique such as the Differential Decay Curve Method (DDCM).

The intensity of the shifted and degraded components are calculated by integrating the population of excited states for the nucleus between time interval $t = 0$, $t = T$ and $t = T$ and $t = \infty$, respectively. The population of an excited state in a cascade is analogous to the activity in a radioactive decay series and obeys the natural decay law

$$N(t) = N_0 e^{-\lambda t}, \quad (2.7)$$

where N_0 is the number of nuclei in a given state at $t = 0$, λ is the decay probability, $N(t)$ is the corresponding number of decays at $t = t$. Hereafter the number of decays

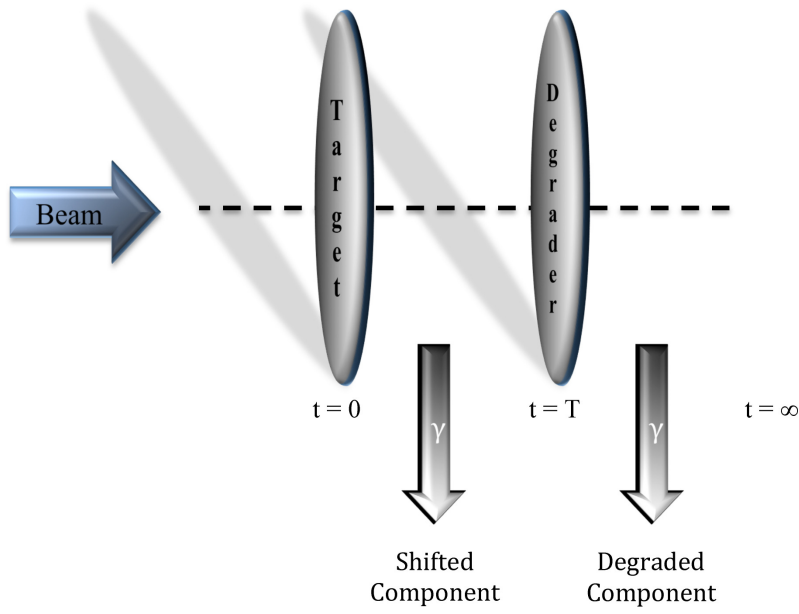


Figure 2.8: A schematic illustration of the degrader and target foils adopted for recoil tagging experiments. The shifted component is the number of γ -ray emitted before the degrader in $0 \leq t < T$ time interval and the degraded component is the number of γ -ray emitted after degrader in $T \leq t < \infty$ time interval.

per second from a specific state is referred to as the activity and is defined as

$$\begin{aligned}
 A(t) &= \frac{dN}{dt} = \lambda N_0 e^{-\lambda t}, \\
 A(t) &= N(t)\lambda, \\
 A(t) &= A_0 e^{-\lambda t}.
 \end{aligned} \tag{2.8}$$

The intensity of the shifted component is the integration of $\lambda N(t)$ within the time interval $0 < t < T$ such that

$$\begin{aligned}
 I_s &= \int_0^T \lambda N_0 e^{-\lambda t} dt, \\
 I_s &= \lambda N_0 \frac{-1}{\lambda} e^{-\lambda t}, \\
 I_s &= -N_0 e^{-\lambda t}, \\
 I_s &= -N_0 (e^{-\lambda T} - 1), \\
 I_s &= N_0 (1 - e^{-\lambda T}).
 \end{aligned} \tag{2.9}$$

If λ is replaced by $1/\tau$ and T is switched to d/v then, the intensity of the shifted component is given in Equation 2.10 as a function of the target-to-degrader distance (d), the lifetime of excited state (τ) and the recoil velocity (v)

$$I_s = N_0(1 - e^{-d/v\tau}). \quad (2.10)$$

The intensity of corresponding degraded component of the γ ray transition is

$$\begin{aligned} I_d &= \int_T^\infty \lambda N_0 e^{-\lambda t} dt, \\ I_d &= \lambda N_0 \frac{-1}{\lambda} e^{-\lambda t}, \\ I_d &= -N_0 e^{-\lambda t} /_T^\infty, \\ I_d &= -N_0(e^{-\infty} - e^{-\lambda T}), \\ I_d &= N_0 e^{-\lambda T}. \end{aligned} \quad (2.11)$$

If the intensity of degraded component is written in terms of d , τ and v it takes the form

$$I_d = N_0 e^{-d/v\tau}. \quad (2.12)$$

It follows that if the velocity of the recoiling nucleus is known then the mean lifetime, τ , can be extracted from a measurement of I_s and I_d or the ratios $I_d/(I_d + I_s)$ or $I_s/(I_d + I_s)$ as a function of distance. For example,

$$\begin{aligned} \frac{I_d}{I_d + I_s} &= \frac{N_0 e^{-d/v\tau}}{N_0} \\ \frac{I_d}{I_d + I_s} &= e^{-d/v\tau} \\ \ln \left(\frac{I_d}{I_d + I_s} \right) &= \frac{-d}{v\tau} \\ \tau &= \frac{-d}{v \ln \left(\frac{I_d}{I_d + I_s} \right)} \end{aligned} \quad (2.13)$$

2.7 The Differential Decay Curve Method (DDCM)

The Recoil Distance Doppler-Shift technique has been used for many years to measure the lifetimes of excited states. In principle, there are no problems in the conventional analysis of RDDS data. The lifetime is extracted by fitting all observed decay curves using a set of coupled differential equations. However, the analysis becomes complicated and often is not easy to extract a reliable lifetime value when a level is fed by many high-lying transitions. The Differential Decay Curve Method (DDCM) [16, 69, 70] was introduced to decrease the complexity arising from a complicated feeding history of a level. The set of coupled differential equations are replaced for each individual level by a single first order differential equation, which can be obtained directly from observables in cases where all feeders of the level of interest are known. The analysis of a plunger data set in the framework of the DDCM allows lifetimes to be measured reliably at only three different target-to-degrader distances. The time interval where the shifted and degraded components vary as a function of distance is called the *region of sensitivity*. In the following sections the underlying mathematical basis of the DDCM and its application to a coincidence analysis will be explained.

2.7.1 Fundamental Mathematics of DDCM

Figure 2.9 shows a hypothetical level scheme. In this scheme a level i is fed by a transition from a higher level h and decays by a transition to lower level j . The time evolution of number of nuclei populated in the level i is defined by the Bateman equations

$$\frac{dn_i(t)}{dt} = -\lambda_i n_i(t) + \lambda_h n_h(t). \quad (2.14)$$

The lifetime $\tau_i(t)$ of level i can be calculated from the intensity of the degraded component of a depopulating γ -ray transition as a function of target-to-degrader

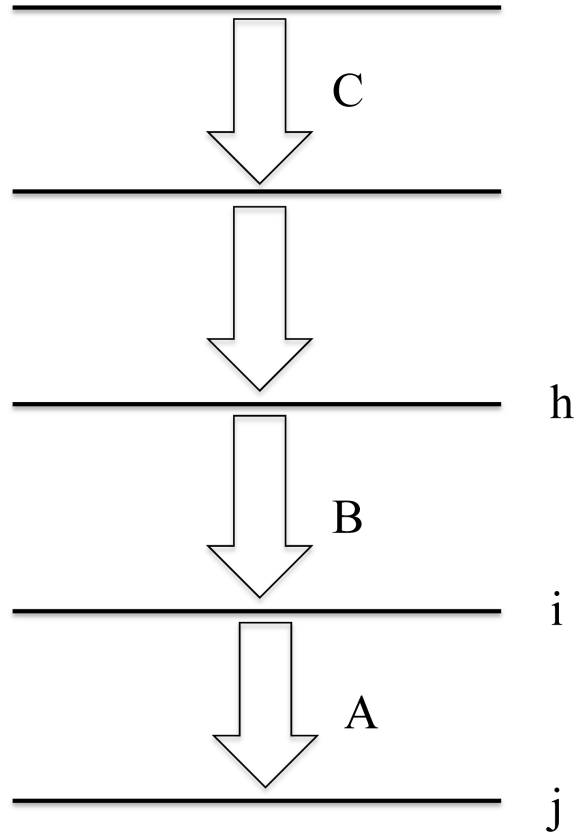


Figure 2.9: Hypothetical Level Scheme. Transition B is gated to measure the lifetime of state i in direct gating method of DDCM. Transition C is gated to measure the lifetime of state i in indirect gating method of DDCM. Transition C is a high-lying feeder for the level i , transition B is the direct feeder and transition A is the depopulator of the state i .

distance and the derivative of that decay function. As stated above the degraded component of a γ -ray transition is determined by integrating Equation 2.14 from t to ∞

$$\int_t^\infty \frac{dn_i(t)}{dt} dt = - \int_t^\infty \lambda_i n_i(t) dt + \int_t^\infty \lambda_h n_h(t) dt. \quad (2.15)$$

If a decay function is defined as $R_i(t)$ for level i and $R_h(t)$ for level h as

$$\begin{aligned} R_i(t) &= \lambda_i \int_t^\infty n_i(t) dt, \\ R_h(t) &= \lambda_h \int_t^\infty n_h(t) dt, \end{aligned} \quad (2.16)$$

and those decay functions are substituted into equation 2.15 one obtains

$$\begin{aligned} n_i(\infty) - n_i(t) &= -R_i(t) + R_h(t), \\ -n_i(t) &= -R_i(t) + R_h(t). \end{aligned} \quad (2.17)$$

Differentiating the decay function of level i yields,

$$\begin{aligned} dR_i/dt &= -\lambda_i n_i(t), \\ n_i(t) &= \frac{-1}{\lambda_i} (dR_i(t)/dt). \end{aligned} \quad (2.18)$$

Combining equations 2.17 and 2.18 relates the decay constant (or lifetime τ) to the decay of the feeder and depopulating transitions of level i ,

$$\begin{aligned} \frac{dR_i(t)}{dt} &= \lambda_i (-R_i(t) + R_h(t)), \\ \frac{1}{\lambda_i} &= - \frac{R_i(t) + R_h(t)}{\frac{dR_i(t)}{dt}}, \\ \tau_i(t) &= - \frac{R_i(t) + R_h(t)}{\frac{dR_i(t)}{dt}}. \end{aligned} \quad (2.19)$$

This relation can be rewritten as a function of distance since $t = d/v$ giving

$$\tau_i(d) = -\frac{R_i(d) + R_h(d)}{v \frac{dR_i(d)}{dt}}, \quad (2.20)$$

where $\tau_i(d)$ is the lifetime of level i for an individual target-to-degrader distance, v is the recoil velocity, $R_i(t)$ and $R_h(t)$ are the decay functions for degraded components of depopulating transitions from levels i and h , respectively and $dR_i(t)/dt$ is the derivative of the decay function $R_i(t)$. Equation 2.20 is the general relation of lifetimes with direct observables but it must be modified for when considering coincidence data.

2.7.2 DDCM for Coincidence Analysis

The first application of the recoil distance Doppler shift technique using γ - γ coincidence data was made by Ward *et al.* who used the technique to measure the lifetimes of excited states in ^{158}Er [71]. In this variant of the technique the decay path is selected by coincidences with the γ ray feeding the level of interest. In this way, the effect of the unobserved feeding is eliminated from the lifetime measurement [69]. The optimum measurements are achieved using γ - γ coincidence plunger experiments with large detector arrays such as JUROGAMII or GAMMASPHERE.

In the γ - γ coincidence experiments, a cascade of transitions (like in Figure 2.9) is observed simultaneously. Measured coincidence intensities must indicate whether the shifted, degraded or the whole lineshape has been used for demanding coincidences. This gives rise to the shorthand notation, $[X_{t_1}^{t_2}, Y_{t_1}^{t_2}]$, which means defines the gating feeder transition X and the depopulating transition Y . The the time intervals t_1, t_2 are chosen to indicate the limits of the integral defining shifted ($t = 0 \rightarrow t$), degraded ($t = t \rightarrow \infty$) or the full lineshape shifted ($t = 0 \rightarrow \infty$). For example, if the aim is to measure the lifetime of level i in Figure 2.9 by gating on the full

lineshape of transition B , which results in observing the full lineshape of transition A , the intensities can be regarded as the sum of different components[70]

$$\left(B_0^\infty, A_0^\infty\right) = \left(B_0^t, A_0^t\right) + \left(B_0^t, A_t^\infty\right) + \left(B_t^\infty, A_0^t\right) + \left(B_t^\infty, A_t^\infty\right). \quad (2.21)$$

As a consequence of time ordering of the transitions (i.e. B is emitted before A) the component

$$\left(B_t^\infty, A_0^t\right) = 0. \quad (2.22)$$

Since the quantities $\left(B_t^\infty, A_0^t\right)$ and $\left(B_0^\infty, A_0^\infty\right)$ are independent of time they produce a useful relation for the derivatives.

$$-\frac{d}{dt}\left(B_0^t, A_0^t\right) = \frac{d}{dt}\left(B_0^\infty, A_t^\infty\right) \quad (2.23)$$

Using the notations given in the previous section and derivatives in this section, the lifetime of a given excited state is determined employing following equation,

$$\tau_i = \frac{-\left(C, A_t^\infty\right) + \left(C, B_t^\infty\right)}{\frac{d}{dt}\left(C, A_t^\infty\right)}, \quad (2.24)$$

where $R_i(d) = \left(C, A_t^\infty\right)$ and $R_h(d) = \left(C, B_t^\infty\right)$. Using Equation 2.23 and replacing $\left(C, A_t^\infty\right)$ with $\left(C, A_d\right)$ and $\left(C, B_t^\infty\right)$ with $\left(C, B_d\right)$, Equation 2.24 can be re-written as

$$\tau_i = \frac{\left(C, A_d\right) - \left(C, B_d\right)}{\frac{d}{dt}\left(C, A_s\right)} \frac{1}{v}. \quad (2.25)$$

Often a gate is set on direct feeding transition of the level of interest. In this case, it becomes simpler to extract lifetime from directly observables and equation 2.25

can be simplified to

$$\tau_i = \frac{\left(B, A_d\right)}{\frac{d}{dt}\left(B, A_s\right)} \frac{1}{v}. \quad (2.26)$$

Figure 2.10 illustrates an example plot for the differential decay curve method. Lifetime values calculated for different distances within the region of sensitivity are presented in Figure 2.10(a), the solid line in the in Figure 2.10(b) is a fit of the normalised shifted curve with second order polynomials to the data. Figure 2.10(c) shows the intensity difference of the degraded component of the direct feeding and depopulating transitions according to Equation 2.25 or the intensity of the degraded component of the depopulating transition according to Equation 2.26 and the solid line is the fit of derivative of the second order polynomials in Figure 2.10(b) multiplied by the lifetime τ to these data points.

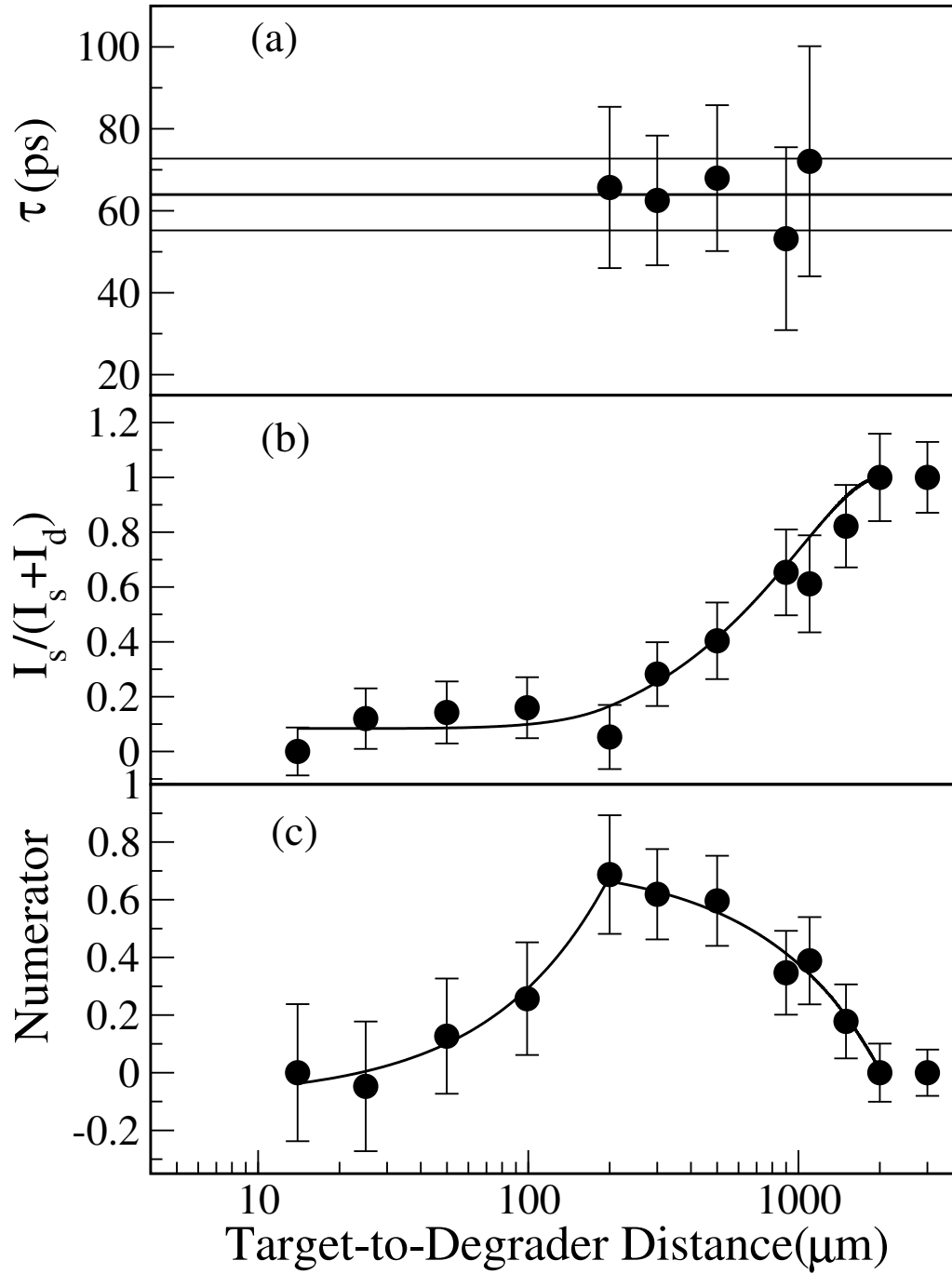


Figure 2.10: Lifetime values calculated for different distances within the region of sensitivity are presented in the top panel. The solid line in the middle panel is a fit of the normalised shifted curve with second order polynomials to the data. The solid line in the panel on bottom is the fit of the degraded component with derivative of the second order polynomials multiplied by the lifetime τ .

Chapter 3

New Excited States in ^{168}Os

The structure of the neutron-deficient nuclide ^{168}Os has been the focus of several recent experiments using the JUROGAM γ -ray spectrometers at the Accelerator Laboratory of the University of Jyväskylä. This chapter reports a significant extension to the known excitation level scheme for ^{168}Os . A parallel experiment by Grahm *et al.* has measured the lifetimes of the yrast states in ^{168}Os using a differential plunger and the recoil distance Doppler-shift method [1]. The ratio of reduced transition probabilities $B(E2; 4_1^+ \rightarrow 2_1^+)/B(E2; 2_1^+ \rightarrow 0_1^+)$ extracted from these measured lifetimes is found to be 0.36(14), which is very unusual for a collective band structure. This chapter discusses scenarios for resolving this apparent anomaly in terms of the newly observed features in the level scheme.

3.1 Introduction

The osmium isotopes currently represent the best opportunity for probing the evolution of nuclear collective behaviour across the $82 \leq N \leq 126$ neutron shell. The existence of the osmium isotopes in an uninterrupted sequence from $^{161}\text{Os}_{85}$ [72] to $^{203}\text{Os}_{124}$ [73] has been established through the measurement of their radioactive decay properties [74]. Excited states have been established in all the known nuclei from $^{162}\text{Os}_{86}$ [11] to $^{198}\text{Os}_{122}$ [12]. The excitation level schemes reveal the evolution of collectivity from single-particle excitations near the $N = 82$ closed shell [11, 75], through weakly deformed vibrational nuclei ($N = 88$), γ -soft rotors ($N = 92$) and shape coexistence ($N = 96$) to well deformed rotors at the neutron midshell ($N = 104$).

The nuclide ^{168}Os occupies the transitional zone between the single-particle and collective regimes. Excited states in ^{168}Os were first identified in recoil-decay tagging experiments [13] by Joss *et al.* who established the ground-state band, the aligned Stockholm ($\nu i_{13/2}^2$) band and two negative-parity $\nu i_{13/2} \otimes \nu(f_{7/2}, h_{9/2})$ side bands to moderate spins and excitation energy. The excitation energy ratio $E(4^+)/E(2^+)$ of ^{168}Os is equal to 2.51, which suggests a collective nucleus that is soft towards triaxial (γ) deformations [76, 77]. The γ -soft nuclei with neutron numbers in the range $88 \leq N \leq 92$ are known to be sensitive to the occupation of core polarising orbitals at the nuclear Fermi surface [13]. Moreover, ^{168}Os lies in close proximity to the $N = 96$ isotones ^{172}Os [14] and ^{174}Pt [78, 79] that exhibit shape coexistence at low spin. The yrast sequences of these nuclides deviate from the usual $I(I+1)$ dependence expected of a rotational nucleus and these perturbations are interpreted to arise from the mixing between the ground-state band and deformed intruder bands [13, 14]. These features provided the motivation for an RDDS lifetime measurement [68, 67] of the yrast states in ^{168}Os by Grahn *et al.* [1]. The results of the lifetime measurements

are presented in Table 3.1.

Table 3.1: Reduced transition probability of the low-lying 2^+ and 4^+ yrast states in ^{168}Os taken from Grahn *et al.* [1].

$E_\gamma[\text{keV}]$	$I_i^\pi \rightarrow I_f^\pi$	$\tau(\text{ps})$	$B(E2)[e^2b^2]\downarrow$	$B(E2)[\text{W.u.}]$
341.2	$2^+ \rightarrow 0^+$	41(7)	0.41(7)	74(13)
516.1	$4^+ \rightarrow 2^+$	15(5)	0.15(5)	27(9)

The reduced transition probabilities, $B(E2)$, extracted from the lifetime measurements have revealed some interesting features. The $B(E2)_{4^+/2^+}$ ratio smaller than unity [1], which is exceedingly rare for collective transitions and inconsistent with model predictions [50]. Ratios of reduced transition probabilities of $B(E2)_{4^+/2^+} < 1$ are possible in certain physical scenarios. For example, such ratios are seen around closed shells where the number of unpaired nucleons, seniority, is a good quantum number [21]. However, the nuclide $^{168}\text{Os}_{92}$ is non-magic and far away from both neutron and proton shell closures. Another possibility for such unusual measurements can be explained in terms of shape coexistence. A small $B(E2; 4^+ \rightarrow 2^+)$ and as a result $B_{4/2} < 1$ occurs if the 4^+ state has a different structure to the 2^+ and 0^+ states. These structural features are quite common in the Hg [80, 18, 19, 81, 82] and Pb [20, 83, 84] isotopes. However, coexisting structures of this type are not anticipated in ^{168}Os at low spin. Indeed, the band mixing calculations of Joss *et al.* for $^{168}\text{Os}_{92}$ place the deformed intruder band at a high excitation energy relative to ground-state band ($E_x \sim 1800$ keV), which suggests that the mixing deformed intruder band is of less significance at low spin [13].

The motivation of this work is to propose explanations of the anomaly in the $B(E2)_{4^+/2^+}$ ratio in ^{168}Os from an empirical point of view. This chapter reports the results of a recent experiment using the highly efficient JUROGAM spectrometers in conjunction with the RITU separator and GREAT focal plane spectrometer that has led to a significant extension of the level scheme in ^{168}Os . New features in the level scheme indicate self-coincident doublets, a more fragmented decay path

from the 12^+ state and a new positive-parity band structure. These features may have consequences for lifetimes measured by Grahn *et al.* [1] and are used in a simple model based on the Bateman Equations to discuss possible scenarios for the apparent anomalous $B(E2)_{4^+/2^+}$ ratio.

3.2 Experimental Details

The neutron-deficient nucleus, ^{168}Os was investigated in an experiment at the University of Jyväskylä Accelerator Laboratory (JYFL). Excited states in ^{168}Os were populated in the fusion evaporation reactions listed in Table 3.2. In each experiment γ rays were detected with the JUROGAM Ge spectrometer array consisting of 43 Eurogam Phase I-type and clover escape-suppressed spectrometers [58] arranged in six angular groups with respect to the beam direction. Evaporation residues recoiling from the target were separated in flight from unreacted beam and fission fragments according to their magnetic rigidity by the RITU gas-filled separator and implanted into the GREAT spectrometer [55] located at the separator focal plane. Recoiling fission residues were distinguished from unreacted beam by the energy loss measured in the GREAT multiwire proportional counter and, in conjunction with the GREAT double-sided silicon strip detectors, their time-of-flight (TOF) characteristics. These data were recorded using the Total Data Readout data acquisition system [63] and analysed offline using the GRAIN [85] and RADWARE [86] software packages.

Data from both experiments was analysed in a high-fold coincidence analysis leading to a significant extension of the ^{168}Os level scheme. The α -decay properties of ^{168}Os are not optimal for the highly selective recoil-decay tagging technique and all the measurements in this thesis are based on the analysis of γ rays that have temporal correlations with fusion-evaporation residues implanted with the GREAT spectrometer.

Table 3.2: Summary of reactions employed in the present work.

Beam Species	Beam Energy (MeV)	Beam Current (pnA)	Target Isotope	Thickness (mg/cm ²)	Duration (h)	Exit Channel	Residual Nucleus
⁷⁸ Kr ¹⁵⁺	335	7	⁹² Mo	0.5	172	2p	¹⁶⁸ Os
⁷⁸ Kr ¹⁵⁺	348	7	⁹² Mo	1.0	26	2p	¹⁶⁸ Os

3.3 Results

A total of 3×10^7 threefold and higher coincidences were recorded in delayed coincidence with any recoil implanted in the DSSDs. These data were sorted off-line using the GRAIN software package into an $E_{\gamma 1} - E_{\gamma 2} - E_{\gamma 3}$ coincidence cube, which was analysed using the LEVIT8R graphical analysis software package [86]. The level scheme for ¹⁶⁸Os was constructed on the basis of relative γ -ray intensities and coincidence relationships from spectra generated from this cube. The deduced level scheme for ¹⁶⁸Os is displayed in Figure 3.1 and the properties of γ rays assigned to this nucleus are recorded in Table 3.3 and 3.4. Figure 3.2 shows typical double-gated spectra highlighting the extension to the known bands in ¹⁶⁸Os. The extension to the aligned $\nu i_{13/2}^2$ configuration, Band 2 in Figure 3.1, contains a 643 keV transition which is unresolved from the 642 keV ($6_1^+ \rightarrow 4_1^+$) transition in the ground-state band. Figure 3.2(a) shows γ rays in coincidence with both 642 and 643 keV and supports the placement of the 643 keV transition above Band 2. Figure 3.2 (b) and (c) show extensions to Bands 3 and 4, respectively.

Table 3.3: Electromagnetic properties of ^{168}Os extracted from the present work.

E_γ (keV)	I_γ (%)	E_i (keV)	I_i	\rightarrow	I_f
125.8	1.97(15)	3365	(12 ⁺)	\rightarrow	(10 ⁺)
140.5	7.6(5)	2731	(10 ⁻)	\rightarrow	(9 ⁻)
144.5	3.3(3)	2299	(8 ⁻)	\rightarrow	(7 ⁻)
207.0	6.1(4)	2938	(11 ⁻)	\rightarrow	(10 ⁻)
236.1	3.8(3)	3365	(12 ⁺)	\rightarrow	(12 ⁻)
237.6	10.6(7)	1737	(5 ⁻)	\rightarrow	6 ⁺
243.3	2.31(18)	3365	(12 ⁺)	\rightarrow	(10 ⁺)
267.0	12.0(8)	1737	(5 ⁻)	\rightarrow	(3 ⁻)
341.1	100(7)	341	2 ⁺	\rightarrow	0 ⁺
348.4	13.6(9)	2938	(11 ⁻)	\rightarrow	(9 ⁻)
365.4	23.5(15)	3731	(14 ⁺)	\rightarrow	(12 ⁺)
382.3	10.1(7)	3365	(12 ⁺)	\rightarrow	10 ⁺
398.3	16.5(10)	3129	(12 ⁻)	\rightarrow	(10 ⁻)
417.3	48(3)	2155	(7 ⁻)	\rightarrow	(5 ⁻)
426.0	12.7(9)	3365	(13 ⁻)	\rightarrow	(11 ⁻)
426.8	5.9(5)	3365	(12 ⁺)	\rightarrow	(11 ⁻)
432.7	6.0(5)	2731	(10 ⁻)	\rightarrow	(8 ⁻)
435.5	44(3)	2590	(9 ⁻)	\rightarrow	(7 ⁻)
515.5	6.2(6)	3240	(10 ⁺)	\rightarrow	(8 ⁺)
516.3	72(5)	857	4 ⁺	\rightarrow	2 ⁺
531.1	18.3(12)	4262	(16 ⁺)	\rightarrow	(14 ⁺)
531.9	6.3(6)	3122	(10 ⁺)	\rightarrow	(9 ⁻)
542.6	3.8(4)	2724	(8 ⁺)	\rightarrow	(6 ⁺)
565.5	10.8(7)	3695	(14 ⁻)	\rightarrow	(12 ⁻)
579.1	12.2(8)	3944	(15 ⁻)	\rightarrow	(13 ⁻)
582.0	2.2(3)	2182	(6 ⁺)	\rightarrow	(4 ⁺)
612.2	11.5(8)	1470	(3 ⁻)	\rightarrow	4 ⁺
625.8	10.4(7)	4888	(18 ⁺)	\rightarrow	(16 ⁺)
641.8	37.2(24)	1499	6 ⁺	\rightarrow	4 ⁺
643.1	6.8(5)	5531	(20 ⁺)	\rightarrow	(18 ⁺)
656.3	6.7(5)	2155	(7 ⁻)	\rightarrow	6 ⁺
677.3	4.8(3)	6208	(22 ⁺)	\rightarrow	(20 ⁺)
688.1	6.5(5)	4383	(16 ⁻)	\rightarrow	(14 ⁻)
691.9	6.4(5)	4635	(17 ⁻)	\rightarrow	(15 ⁻)
724.1	21.1(14)	2223	8 ⁺	\rightarrow	6 ⁺
724.1	21.1(14)	2223	8 ⁺	\rightarrow	6 ⁺
743.4	5.8(6)	1600	(4 ⁺)	\rightarrow	4 ⁺
760.1	15.5(10)	2983	10 ⁺	\rightarrow	8 ⁺
774.0	3.4(3)	5409	(19 ⁻)	\rightarrow	(17 ⁻)

Table 3.4: . Table 3.3 continued

E_γ (keV)	I_γ (%)	E_i (keV)	I_i		I_f
778.2	3.3(3)	5161	(18 ⁻)	→	(16 ⁻)
840.8	1.04(15)	6002	(20 ⁻)	→	(18 ⁻)
851.2	1.35(16)	6261	(21 ⁻)	→	(19 ⁻)
879.9	31.3(20)	1737	(5 ⁻)	→	4 ⁺
1128.8	5.3(5)	1470	(3 ⁻)	→	2 ⁺
1224.8	3.0(3)	2724	(8 ⁺)	→	6 ⁺
1257.7	2.7(5)	1600	(4 ⁺)	→	(4 ⁺)
1325.2	1.5(3)	2182	(6 ⁺)	→	4 ⁺

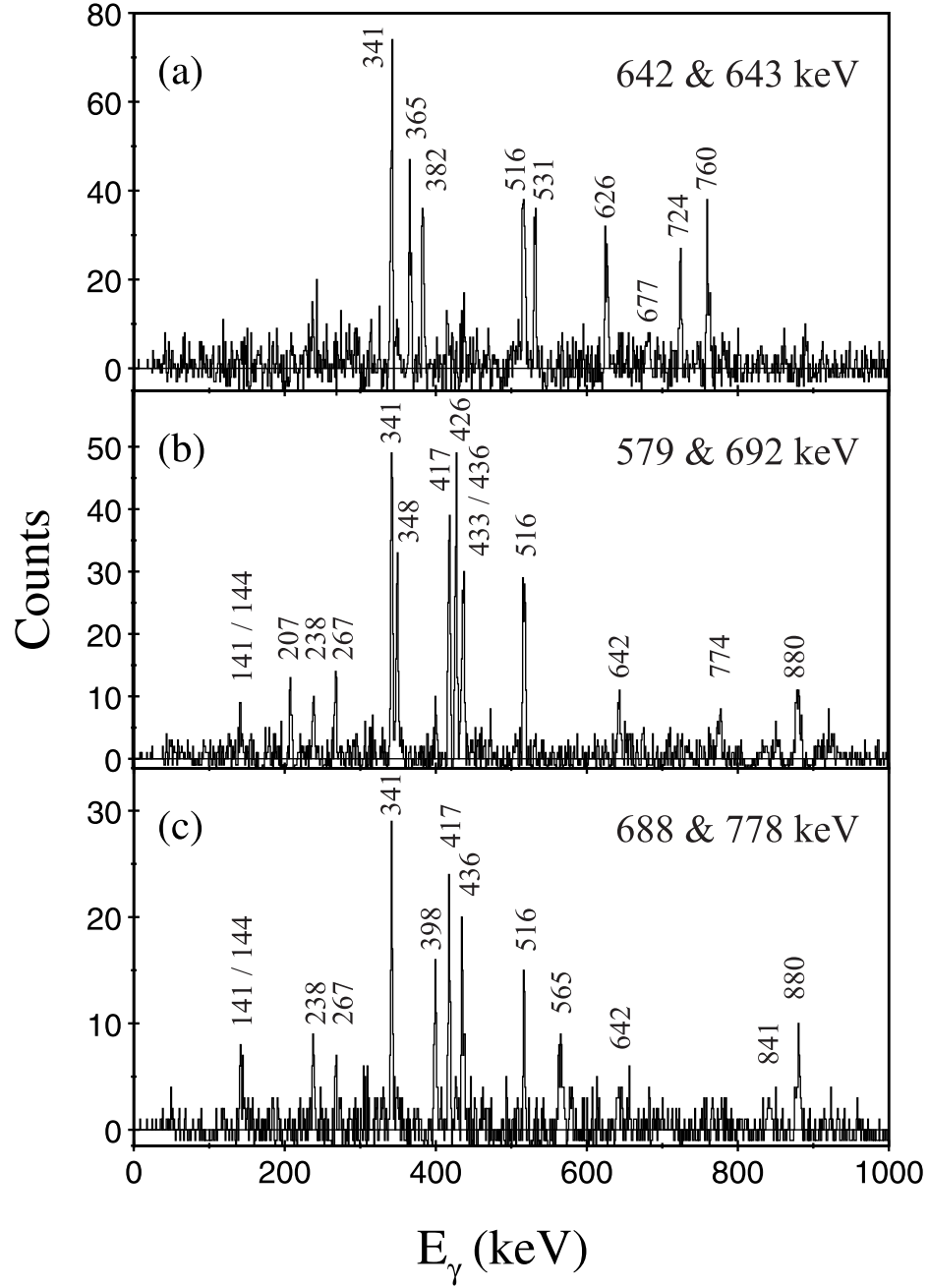


Figure 3.2: Double-gated γ -ray coincidence spectra correlated with a recoil implantation in the GREAT spectrometer. (a) spectrum showing γ rays in coincidence with the 642 and 643 keV transitions. (b) Spectrum showing γ rays in coincidence with the 579 and 692 keV transitions in Band 3. (c) Spectrum showing γ rays in coincidence with the 688 and 778 keV transitions in Band 4.

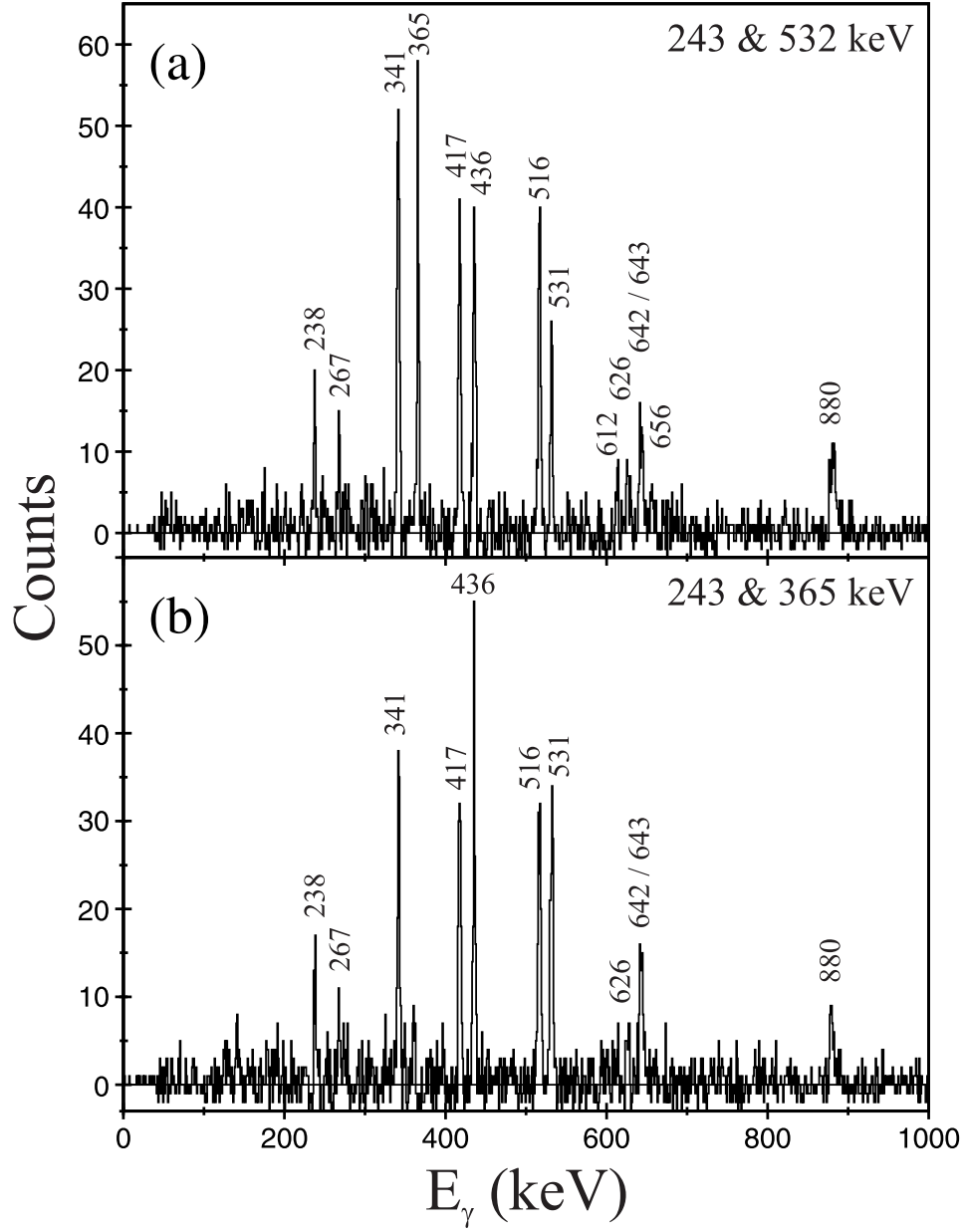


Figure 3.3: Double-gated γ -ray coincidence spectra correlated with a recoil implantation in the GREAT spectrometer. Spectra show a new decay path from the 12^+ state to the 9^- state in Band 3. (a) spectrum showing γ rays in coincidence with the 243 and 532 keV transitions. (b) Spectrum showing γ rays in coincidence with the 243 and 365 keV transitions.

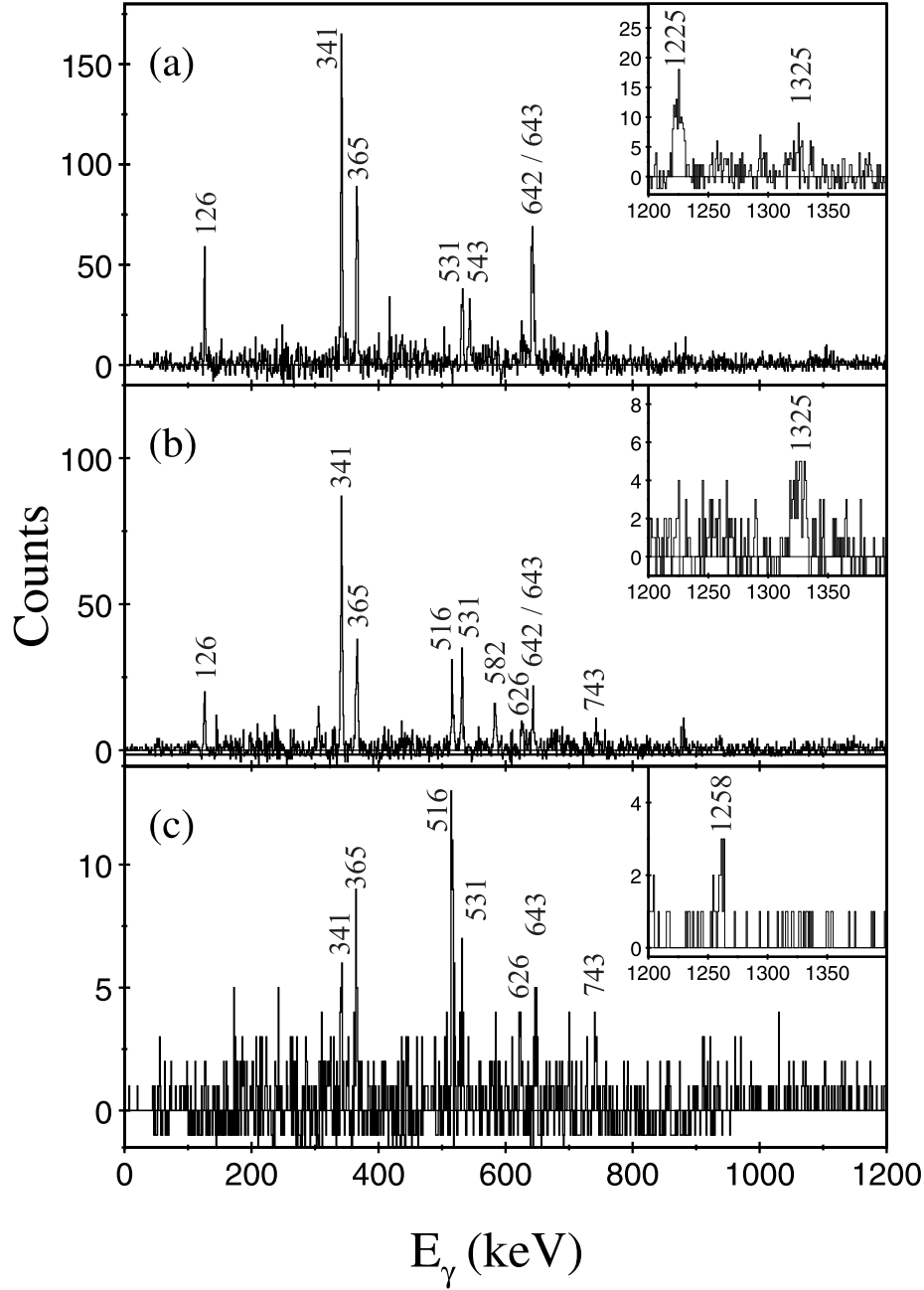


Figure 3.4: Double-gated γ -ray coincidence spectra correlated with a recoil implantation in the GREAT spectrometer. Spectra show a new decay path from the 12^+ state to Band 1. Insets to the figure show the high-energy linking transitions from the quasi- β band to the ground-state band. (a) Spectrum showing γ rays in coincidence with the 516 and 516 keV transitions. (b) Spectrum showing γ rays in coincidence with the 516 and 543 keV transitions. (c) Spectrum showing γ rays in coincidence with the 543 and 582 keV transitions.

The 12^+ state in Band 2 was known to have discrete γ -ray branches to the ground-state band and the negative-parity side bands, Bands 3 and 4. In this work two further decay paths from the 12^+ state have been established. Figure 3.1 shows a new decay path from the 12^+ state comprising the 243 keV transition and another 531 keV transition that feeds the negative-parity odd-spin structure labelled as Band 3. Figure 3.3 (a) and (b) show γ -ray in coincidence with 243 and 521 keV and 243 and 365 keV transitions, respectively. The figures support the link between Band 2 and Band 3.

In addition, Figure 3.1 shows a new band structure (Band 1), which forms another parallel decay path to the low-spin states of the ground state band. Spectra in Figure 3.4 indicate γ -ray in coincidence with 516 and 516 keV and 516 and 543 keV and 543 and 582 keV transitions, respectively. The spectra show a new decay path from the 12^+ state to Band 1. Although, it has not been possible to measure the multipolarities of the transitions in the new band, a positive-parity even-spin structure is likely from the γ -ray decay branches from the lowest observed state in Band 1 to low-spin states of the ground-state band.

3.4 Discussion

3.4.1 Configuration Assignments

The first excited positive-parity band is traditionally assumed to be based on a β -vibrational state. However, reduced transition probabilities are required to confirm whether this is the case for ^{168}Os [87]. The β -vibrational bands have been observed in the heavier even- N Os isotopes above ^{170}Os in experiments probing non-yrast states populated in the β decay of the odd-odd Ir precursors. Figure 3.5 compares Band 1 in ^{168}Os with the systematic trends established for the heavier isotopes. The excitation energies in Band 1 appear to show a smooth increase below $N = 96$

compared with the relatively constant trends established for the heavier isotopes. Band mixing calculations indicate that the band head of the deformed intruder configuration is expected be around 1800 keV and it may be possible for mixing to perturb the regular band sequence [13].

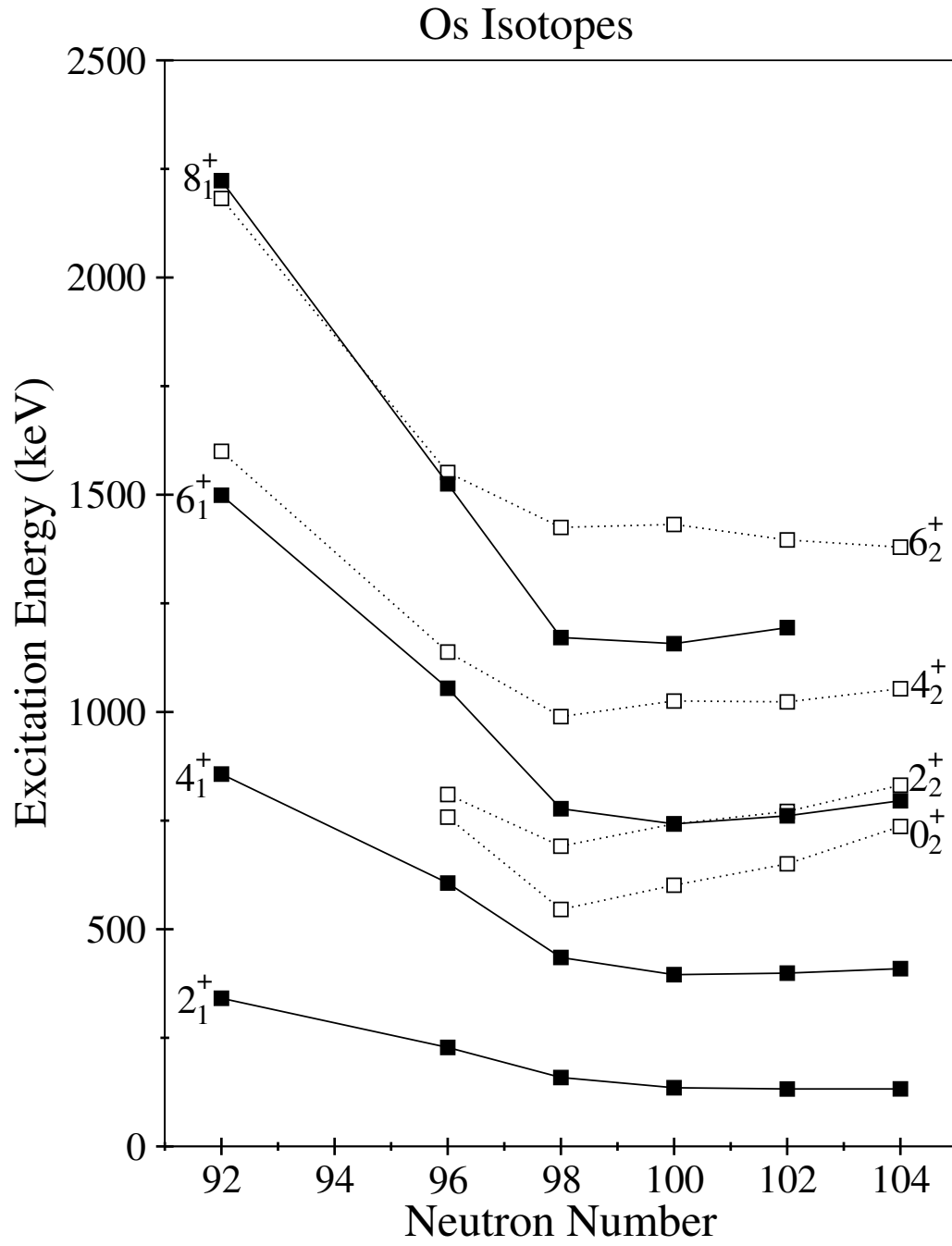


Figure 3.5: Comparison of the excitation energies of states in the new positive-parity structure in ^{168}Os (Band 1) with the quasi- β bands in the heavier Os isotopes. Data taken from references [88].

Figure 3.6 shows the alignment, I_x , as a function of rotational frequency for the bands in ^{168}Os extracted from the level scheme in Figure 3.1. The ground-state band shows an alignment gain of $\Delta I_x = 11\hbar$ at $\hbar\omega = 0.2$ MeV, which is consistent with the rotational alignment of a pair of $i_{13/2}$ neutrons. The extension of Band 2 to higher spin is reflected in Figure 3.6 as the beginnings of an upbend at $\hbar\omega = 0.3$ MeV. As the complete alignment is not seen it is difficult to assign a configuration. It is also possible that the new transitions assigned to Band 2 are links to other unobserved high spin structures.

The alignments extracted for Bands 2 and 3 are very similar. At low frequency, the alignments for both bands are low but quickly achieve an alignment of around $9\hbar$ at 0.2 MeV, which is lower than the alignment measured for Band 1. At rotational frequencies $\hbar\omega > 0.2$ MeV, the alignment of both side bands increases smoothly. These features have been interpreted previously as octupole vibrational states that are crossed by two-quasineutron configurations formed by coupling the $i_{13/2}$ and $(f_{7/2}, h_{9/2})$ neutrons [13].

3.4.2 Reduced Transition Probabilities

Lifetimes of excited states in ^{168}Os were extracted using the differential decay curve method using recoil-correlated $\gamma\gamma$ coincidences in a recent experiment by Grahn *et al.* [1]. The reduced transition probabilities extracted from lifetime measurements of the 2^+ and 4^+ states yielded an anomalous ratio $B(E2)_{4^+/2^+} = 0.36(14)$. $B(E2)$ ratios less than unity are seen around closed-shells due to seniority effects [21], however, it is quite unexpected in deformed nuclei far from closed shells. The other physical phenomenon that can produce low $B(E2)$ ratios relate to shape coexistence.

The manifestations of shape coexistence in the osmium isotopes differ from those displayed by nuclei closer to the $Z = 82$ closed shell. In Pb and Hg isotopes distinctly deformed configurations based on multiple proton-hole excitations are ob-

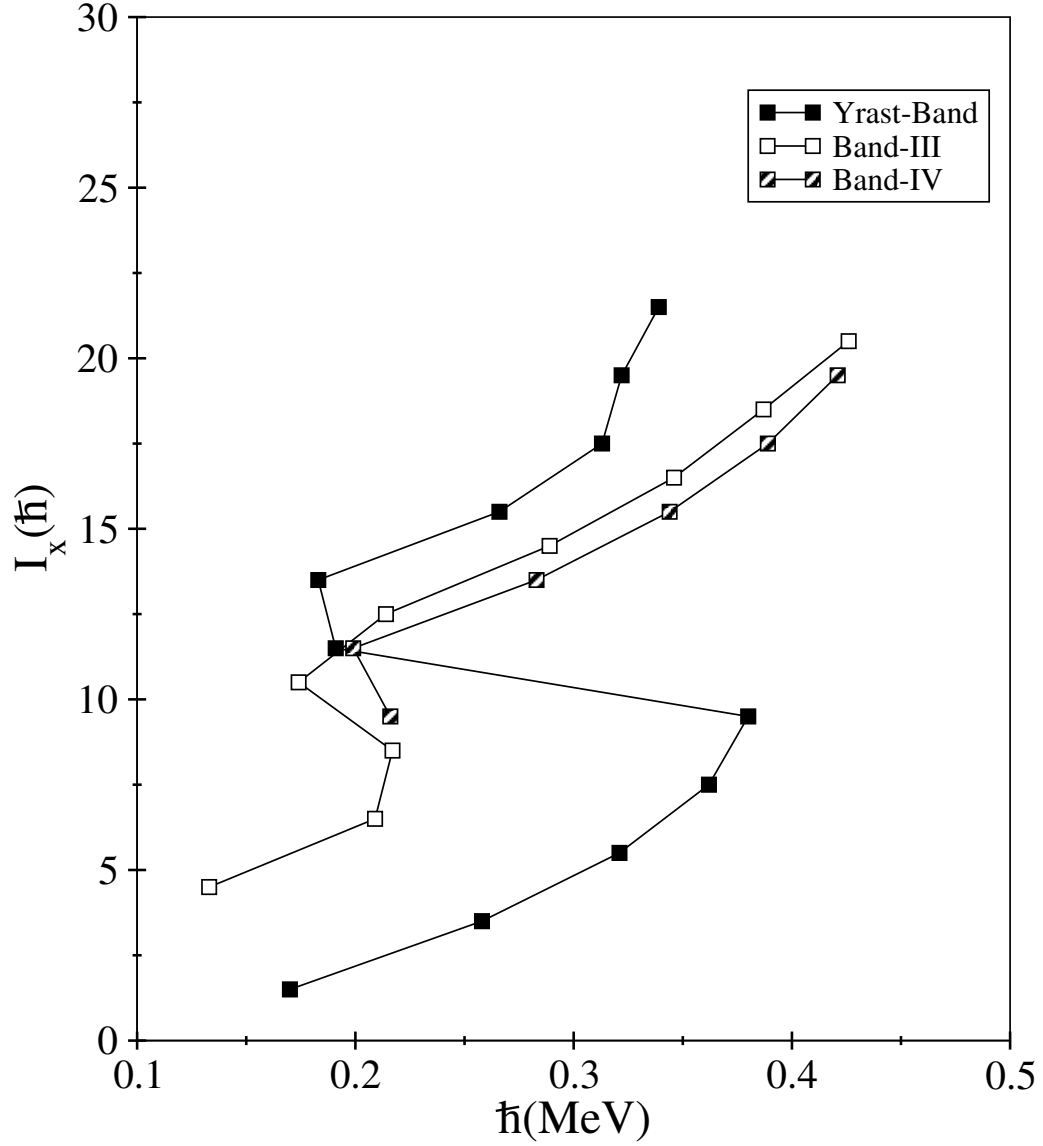


Figure 3.6: The total aligned angular momentum, I_x as a function of rotational frequency for the bands in ^{168}Os .

served while in the Pt and Os nuclei the interaction of the ground and intruder bands result in a single mixed band with an irregular yrast spectrum. Figure 3.7 shows the variation of the excitation energy ratio $E_{4+/2+}$ as a function of neutron number in the neutron-deficient $66 \leq Z \leq 78$ nuclei. The nuclei with proton numbers up to $Z = 74$ show a smooth behaviour interpreted as the variation from a well-deformed prolate structure near the neutron midshell ($N = 104$) to the near

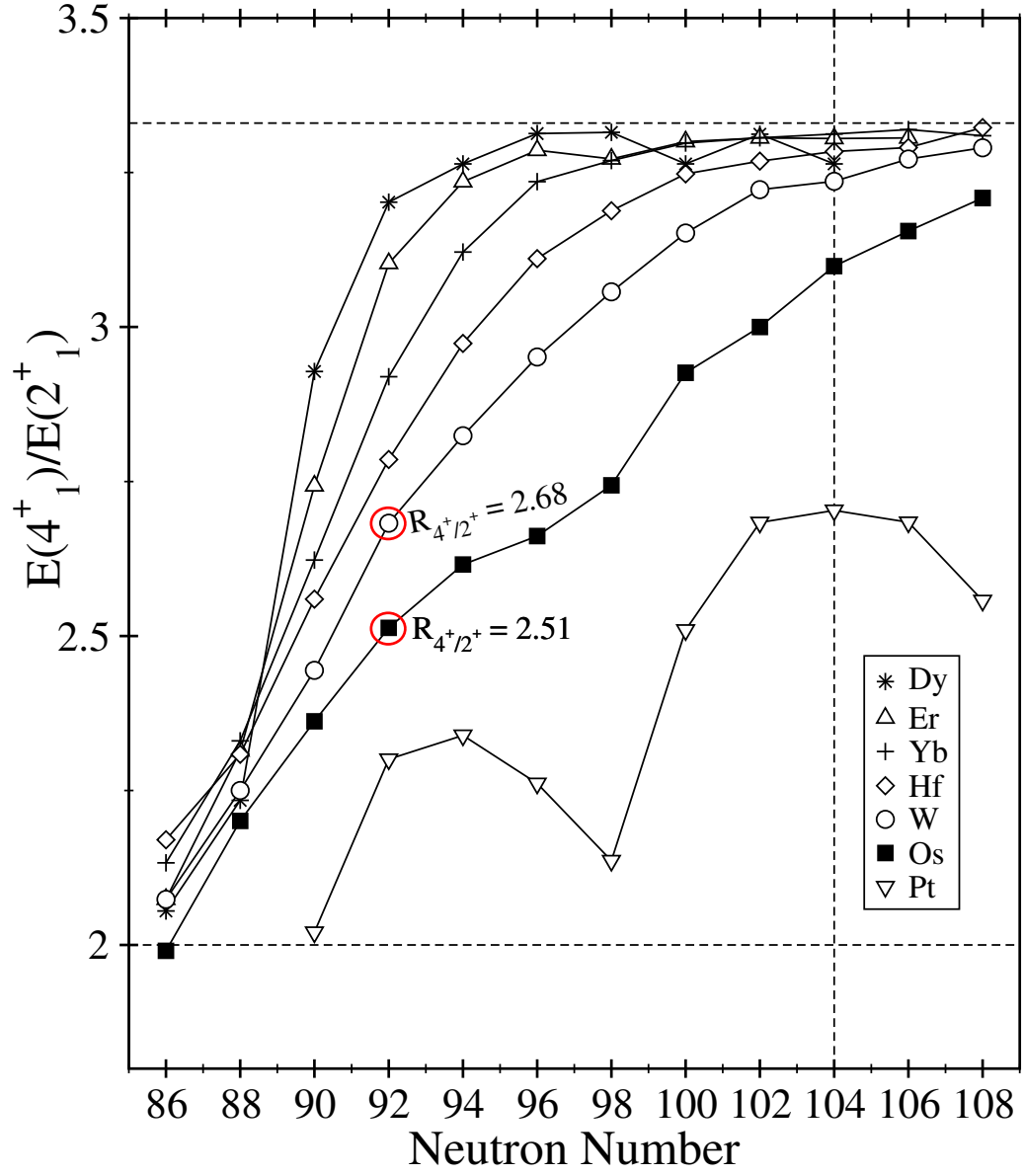


Figure 3.7: Variation of ratio of the 4^+ and 2^+ state excitation energy in the even neutron-deficient $66 \leq Z \leq 78$ nuclei as function of neutron number. Data from National Nuclear Data Center (NNDC).

spherical single-particle regime at $N = 82$. The Os and Pt isotopes show deviations from this smooth behaviour around $N = 98$, which is attributed to arise from the perturbation of the yrast levels due to band mixing [14, 78, 88, 89]. The ratio for the ground-state band in ^{168}Os appears to be on the edge of the shape coexistence region and follows the otherwise smooth trend for the isotopic chain. Indeed, band mixing calculations by Joss *et al.* place the deformed intruder band at a higher excitation energy in ^{168}Os relative to the ground state when compared with the heavier osmium isotopes [13] and show less pronounced perturbation effects. The smooth variation of the alignment plot showed in Figure 3.6 also suggests that there are no significant mixing at low spin. The new level scheme has revealed a second 4^+ state in Band 1, see Figure 3.2, but not 2_2^+ state. The 4_2^+ state is placed 750 keV above the 4_1^+ state and suggest there is little mixing between Band 1 and the ground-state band.

The key point to explain the anomaly in $B(E2)_{4^+/2^+}$ ratio is to understand which state causes the problem. The $B(E2)$ systematics have been examined for the 2^+ and 4^+ states in ^{168}Os and the neutron-deficient $66 \leq Z \leq 78$ nuclei in Figure 3.8.

Figure 3.8(a) shows the $B(E2)$ measurements of the 2^+ state. There is a smooth trend as a function of neutron number with higher Z nuclei having lower collectivity, which reflect their positions relative to the closed proton shell at $Z = 82$. Figure 3.8(b) displays the $B(E2)$ measurements of the 4^+ states. The collectivity of the 4^+ state of the Dy, Er and Yb isotopes behaves in a similar way in the 2^+ state systematics. However, the sudden decrease in the Os and W isotopes is striking suggesting that the anomalous ratio $B(E2)_{4^+/2^+}$ might originate from the measurements of the 4^+ state.*

Figure 3.9 shows the $B(E2)_{4^+/2^+}$ ratios extracted for collective bands in the even-even neutron-deficient $66 \leq Z \leq 78$ nuclei as a function of P factor. The P factor is

*N.B. The $B(E2:2^+ \rightarrow 0^+)$ value in ^{166}W also deviates from the trend for the W isotopes and could affect the $B(E2)_{4^+/2^+}$ ratio. See next chapter.

defined as

$$P = \frac{N_\pi N_\nu}{N_\pi + N_\nu}, \quad (3.1)$$

where N_π and N_ν are the number of valence protons and neutrons from the nearest closed shell, respectively. The $B(E2)_{4+/2+}$ ratios for most nuclei are banded together above $B(E2)_{4+/2+} > 1$, however ^{168}Os and its isotone, ^{166}W are particularly low. The next section develops a simple model to attempt to explain the anomaly in ^{168}Os .

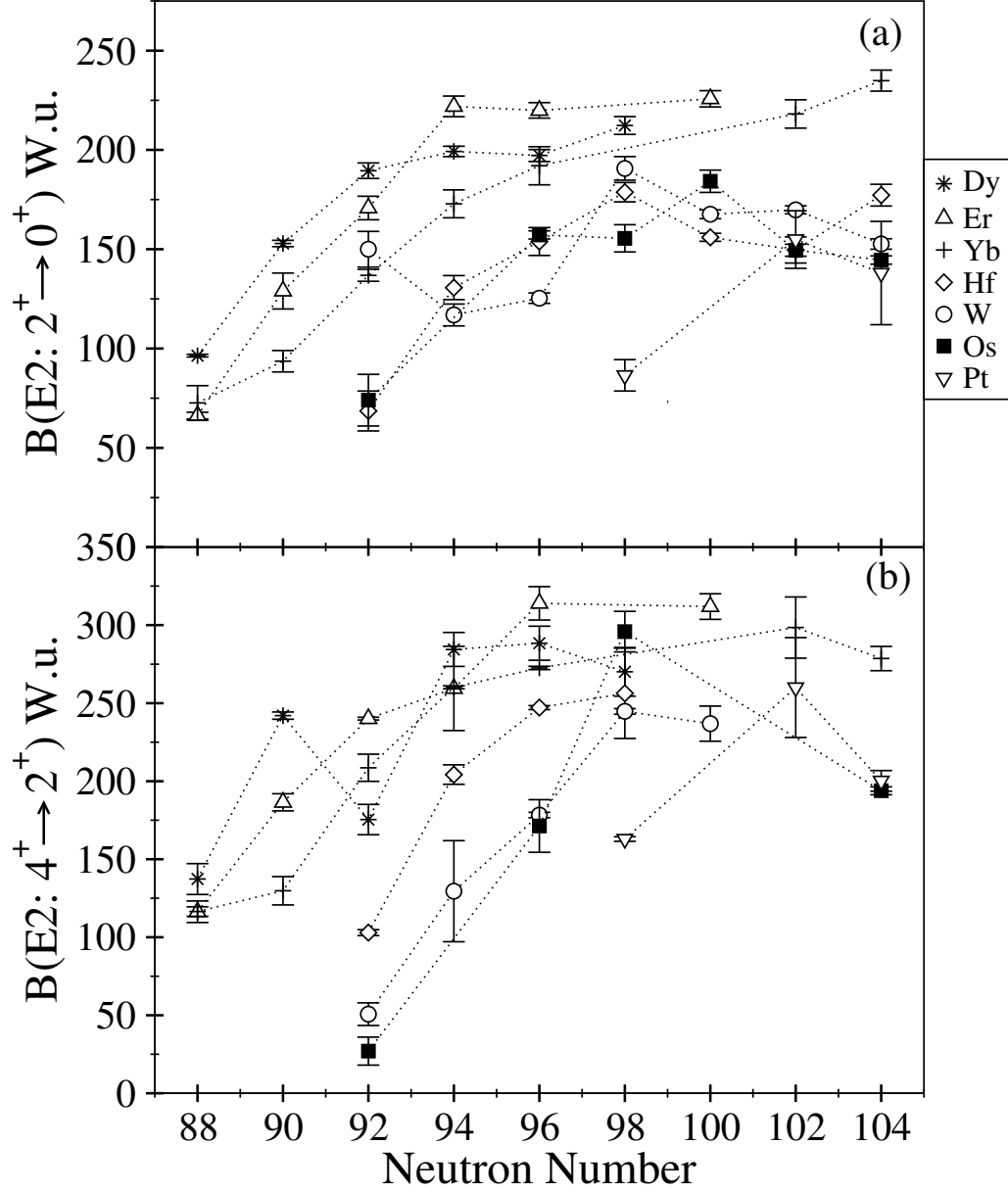


Figure 3.8: Comparison of experimental $B(E2)$ values of the 2^+ and 4^+ state in the even neutron-deficient $66 \leq Z \leq 78$ nuclei as a function of neutron number. Data from National Nuclear Data Center (NNDC). Exceptions are ^{168}Os [1], ^{166}W from present work, τ of the 2^+ state in ^{172}W and ^{178}W [90], ^{174}W [91] and ^{176}W [92].

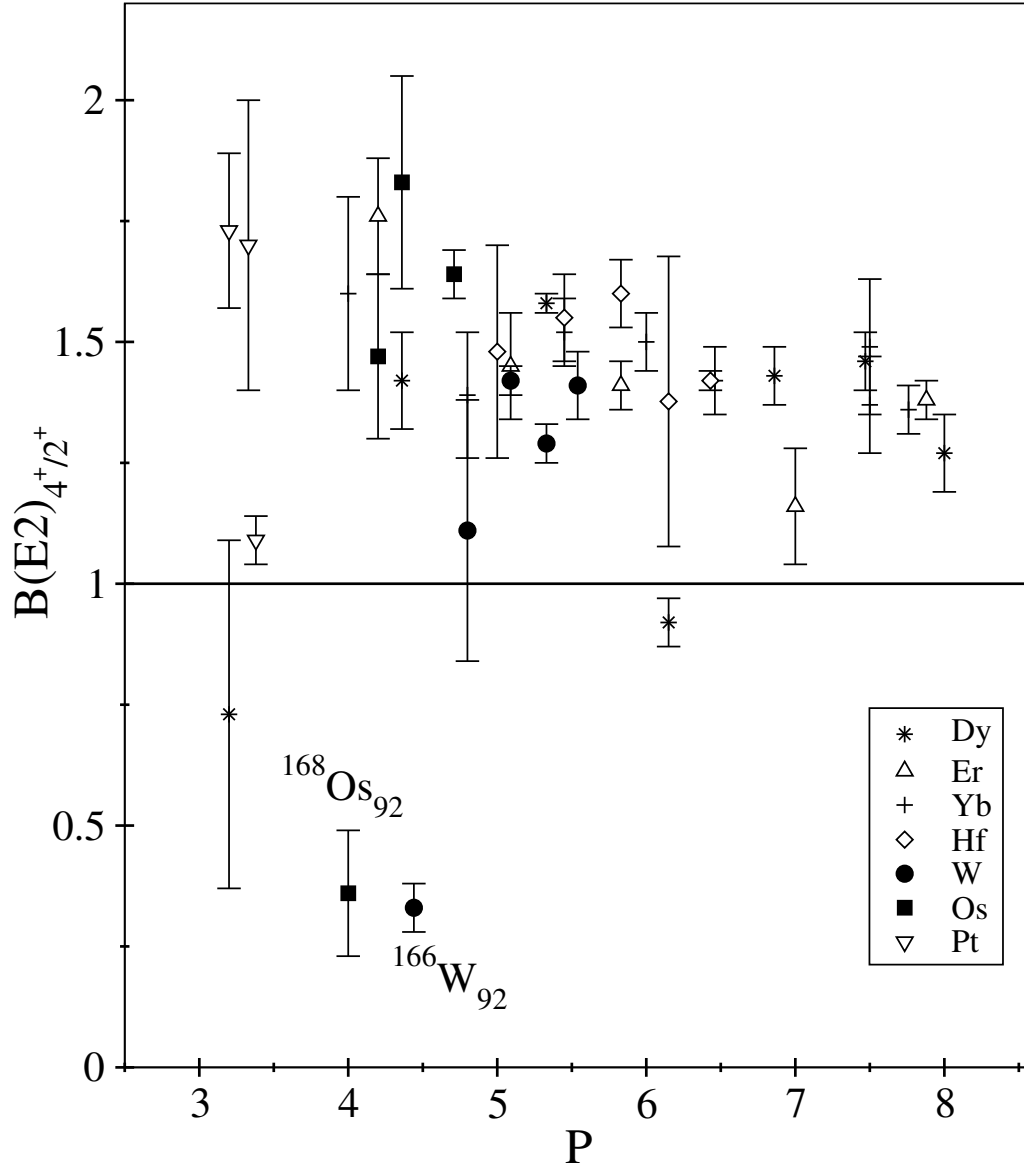


Figure 3.9: Comparison of experimental $B(E2)_{4+/2+}$ ratios in the even neutron-deficient $66 \leq Z \leq 78$ nuclei as a function of P factor. Data from National Nuclear Data Center (NNDC). Exceptions are ^{168}Os [1], ^{166}W from present work, τ of the 2^+ state in ^{172}W and ^{178}W [90], ^{174}W [91] and ^{176}W [92].

3.4.3 The Model

A model based on differential decay curve method has been produced using the Bateman Equations to explore possible scenarios for the anomalous $B(E2; 4_1^+ \rightarrow 2_1^+)/B(E2; 2_1^+ \rightarrow 0_1^+)$ ratios. In this section, the model and its mathematical foundation are described. The DDCM concepts have been explained in Section 2.7. The necessary shifted and degraded components of γ -ray transitions that are used as input for the DDCM are modelled as a function of time using Bateman equations for n th order γ -ray cascades. The concept of activity defined as

$$N(t) = N_0 \exp(-\lambda t), \quad (3.2)$$

plays a key role in the model to reproduce experimentally observed shifted and degraded components.

The objective of the model is to investigate the time behaviour of the feeder and depopulator transitions of the level of interest. In the experimental analysis of the ^{168}Os , lifetimes of the 2^+ and 4^+ states were extracted using the difference between the intensities of degraded components of the feeder and depopulator of the state of interest. The abnormal behaviour of the $B(E2)_{4^+/2^+}$ ratio arises as a result of the reduced transition probability of the 4^+ , see Figure 3.8. The new features in the ^{168}Os level scheme may have implications for the time behaviour of the 4^+ state deduced from the DDCM analysis since the 516 keV and 642/643 keV doublets were used to extract the lifetime of the 4^+ state.

The effects of the following structural features in the level scheme on the lifetime of the 4^+ state are explored in terms of the model.

- (a) The 642/643 keV doublet.
- (b) The fragmented character of the decay path from the 12^+ state implies a

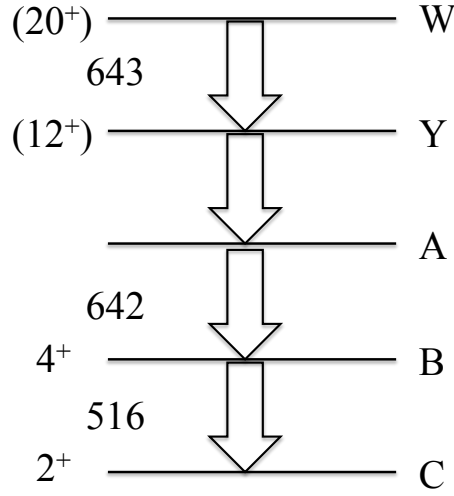


Figure 3.10: Hypothetical Level Scheme based on ^{168}Os . The labelling of the levels maps the real spins and parities on ^{168}Os to the labels used in the model.

lifetime and a feeding delay.

- (c) The 642/643 keV doublet straddling a long-lived 12^+ state .
- (d) The 516 keV doublet.
- (e) Contaminants from other reaction channels in the recoil-gated spectra.

Figure 3.10 shows a simple level scheme based on the ^{168}Os level scheme. Level B represents the 4^+ state, A is the 6^+ state, Y is assigned to be the 12^+ state that is suggested to have a relatively ($\sim \text{ns}$) long half-life and W indicates the 20^+ state that is depopulated by 643 keV transition in Figure 3.1.

Assume a gate was set on 516 keV transition in order to obtain the degraded component of the overlapping 642/643 keV transition. In the reaction, ^{168}Os nuclei can be independently populated at W, Y and A states. Once nuclei populated at

state W, it decays via Y and A. If nuclei are populated at state Y, then they decay via A. The last possibility is to populate nuclei directly at state A. Although the nuclei can be populated at B, the time profile of the depopulator transition of the state B is not under investigation at this moment. Firstly, the level population should be determined by using Bateman equation. The objective of the mathematical model is to define number of nuclei in a given state and subsequently estimate the activity of the corresponding state.

Equation 3.3 represents the number of nuclei in state A populated via the decay of state W via Y and A

$$N_A = \frac{N_W \lambda_W \lambda_Y e^{-\lambda_W t}}{(\lambda_Y - \lambda_W)(\lambda_A - \lambda_W)} + \frac{N_W \lambda_W \lambda_Y e^{-\lambda_Y t}}{(\lambda_W - \lambda_Y)(\lambda_A - \lambda_Y)} + \frac{N_W \lambda_W \lambda_Y e^{-\lambda_A t}}{(\lambda_W - \lambda_A)(\lambda_Y - \lambda_A)}, \quad (3.3)$$

where N_W is the number of nuclei populated at state W that can be measured from experimental data, λ_W , λ_Y and λ_A are the decay constants of states W, Y and A, respectively. The corresponding activity for any given decay is defined by the differential equation

$$\frac{dN_X}{dt} = -\lambda_X N_X, \quad (3.4)$$

where X corresponds to any specific state (e.g. A, B, C, W, Y). Thus the activity of state A can be found using

$$\frac{dN_A}{dt} = - \left(\frac{N_W \lambda_W \lambda_Y e^{-\lambda_W t}}{(\lambda_Y - \lambda_W)(\lambda_A - \lambda_W)} + \frac{N_W \lambda_W \lambda_Y e^{-\lambda_Y t}}{(\lambda_W - \lambda_Y)(\lambda_A - \lambda_Y)} + \frac{N_W \lambda_W \lambda_Y e^{-\lambda_A t}}{(\lambda_Y - \lambda_A)(\lambda_W - \lambda_A)} \right) \lambda_A. \quad (3.5)$$

After determining the number of decays as a function of time, the integration of Equation 3.6 is employed within the time interval $[0, t]$. Equations 3.7 and 3.8 show

the integration step by step.

$$\int_0^t \frac{dN_A}{dt} = - \int_0^t \left(\frac{N_W \lambda_W \lambda_Y \lambda_A e^{-\lambda_W t}}{(\lambda_Y - \lambda_W)(\lambda_A - \lambda_W)} + \frac{N_W \lambda_W \lambda_Y \lambda_A e^{-\lambda_Y t}}{(\lambda_W - \lambda_Y)(\lambda_A - \lambda_Y)} + \frac{N_W \lambda_W \lambda_Y \lambda_A e^{-\lambda_A t}}{(\lambda_Y - \lambda_A)(\lambda_W - \lambda_A)} \right) dt, \quad (3.6)$$

$$\int_0^t \frac{dN_A}{dt} = - \left(\frac{N_W \lambda_Y \lambda_A (e^{-\lambda_W t})|_0^t}{(\lambda_Y - \lambda_W)(\lambda_A - \lambda_W)} + \frac{N_W \lambda_W \lambda_A (e^{-\lambda_Y t})|_0^t}{(\lambda_W - \lambda_Y)(\lambda_A - \lambda_Y)} + \frac{N_W \lambda_W \lambda_Y (e^{-\lambda_A t})|_0^t}{(\lambda_Y - \lambda_A)(\lambda_W - \lambda_A)} \right), \quad (3.7)$$

$$\int_0^t \frac{dN_A}{dt} = - \left(\frac{N_W \lambda_Y \lambda_A (e^{-\lambda_W t} - 1)}{(\lambda_Y - \lambda_W)(\lambda_A - \lambda_W)} + \frac{N_W \lambda_W \lambda_A (e^{-\lambda_Y t} - 1)}{(\lambda_W - \lambda_Y)(\lambda_A - \lambda_Y)} + \frac{N_W \lambda_W \lambda_Y (e^{-\lambda_A t} - 1)}{(\lambda_W - \lambda_A)(\lambda_Y - \lambda_A)} \right). \quad (3.8)$$

Equation 3.9 defines the shifted component of the 642/643 keV transition as a function of time in the decay path from W to A.

$$\int_0^t \frac{dN_A}{dt} = \frac{N_W \lambda_Y \lambda_A (1 - e^{-\lambda_W t})}{(\lambda_Y - \lambda_W)(\lambda_A - \lambda_W)} + \frac{N_W \lambda_W \lambda_A (1 - e^{-\lambda_Y t})}{(\lambda_W - \lambda_Y)(\lambda_A - \lambda_Y)} + \frac{N_W \lambda_W \lambda_Y (1 - e^{-\lambda_A t})}{(\lambda_W - \lambda_A)(\lambda_Y - \lambda_A)} \quad (3.9)$$

Equation 3.10 defines the shifted component of the 642/643 keV transition as a function of time in the decay path from Y to A.

$$\int_0^t \frac{dN_A}{dt} = \frac{N_Y \lambda_A (1 - e^{-\lambda_Y t})}{(\lambda_A - \lambda_Y)} + \frac{N_Y \lambda_Y (1 - e^{-\lambda_A t})}{(\lambda_Y - \lambda_A)} \quad (3.10)$$

Equation 3.11 defines the shifted component of the 642/643 keV transition as a function of time in the decay path from A.

$$\int_0^t \frac{dN_A}{dt} = N_A (1 - e^{-\lambda_A t}) \quad (3.11)$$

Equation 3.12 defines the shifted component of the second 642/643 keV transition as a function of time. The component in Equation 3.12 refers the effect of the being doublet 642/643 keV transition in the analysis of apparent lifetime of state B, (see

later in Equation 3.17).

$$\int_0^t \frac{dN_W}{dt} = N_W(1 - e^{-\lambda_W t}) \quad (3.12)$$

In order to extract the lifetime of the 4^+ state, the second gate was set on the 642/643 keV transition to obtain the degraded component of the 516 keV transition. To examine the time profile of the depopulator transition it is assumed that ^{168}Os nuclei can be populated at states W then decay via Y, A and B or populated at Y then decay via A and B or populated at A, then decays via B. The nuclei cannot be populated at B, since the gate on 642 keV eliminates side-feeding to state B. Steps such as the determination of the number of nuclei, activity and integration follow the same methodology stated earlier and are not reproduced in this instance for reasons of brevity. Equation 3.13 shows the time behaviour of the shifted component of the 516 keV transition in the decay path from W to B.

$$\begin{aligned} \int_0^t \frac{dN_B}{dt} = & \frac{N_W \lambda_Y \lambda_A \lambda_B (1 - e^{-\lambda_W t})}{(\lambda_Y - \lambda_W)(\lambda_A - \lambda_W)(\lambda_B - \lambda_W)} + \frac{N_W \lambda_W \lambda_A \lambda_B (1 - e^{-\lambda_Y t})}{(\lambda_W - \lambda_Y)(\lambda_A - \lambda_Y)(\lambda_B - \lambda_Y)} \\ & + \frac{N_W \lambda_W \lambda_Y \lambda_B (1 - e^{-\lambda_A t})}{(\lambda_W - \lambda_A)(\lambda_Y - \lambda_A)(\lambda_B - \lambda_A)} + \frac{N_W \lambda_W \lambda_Y \lambda_A (1 - e^{-\lambda_B t})}{(\lambda_W - \lambda_B)(\lambda_Y - \lambda_B)(\lambda_A - \lambda_B)} \end{aligned} \quad (3.13)$$

Equation 3.14 shows the time behaviour of the shifted component of the 516 keV transition in the decay path from Y to B.

$$\int_0^t \frac{dN_B}{dt} = \frac{N_Y \lambda_A \lambda_B (1 - e^{-\lambda_Y t})}{(\lambda_A - \lambda_Y)(\lambda_B - \lambda_Y)} + \frac{N_Y \lambda_Y \lambda_B (1 - e^{-\lambda_A t})}{(\lambda_Y - \lambda_A)(\lambda_B - \lambda_A)} + \frac{N_Y \lambda_Y \lambda_A (1 - e^{-\lambda_B t})}{(\lambda_Y - \lambda_B)(\lambda_A - \lambda_B)} \quad (3.14)$$

Equation 3.15 shows the time behaviour of the shifted component of the 516 keV transition in the decay path from A to B.

$$\int_0^t \frac{dN_B}{dt} = \frac{N_A \lambda_B (1 - e^{-\lambda_A t})}{(\lambda_B - \lambda_A)} + \frac{N_A \lambda_A (1 - e^{-\lambda_B t})}{(\lambda_A - \lambda_B)} \quad (3.15)$$

The DDCM in coincidence mode uses the following relation to determine the lifetime

of a state

$$\tau(t) = \frac{I_{dep.}^d(t) - I_{fee.}^d(t)}{\frac{d}{dt}I_{dep.}^s(t)}. \quad (3.16)$$

The degraded components of the 642/643 keV and 516 keV transitions should be obtained by subtracting the shifted components. Firstly, N_W , N_Y and N_A should be summed in order to determine the initial number of nuclei. The time behaviour of the degraded components can be obtained if the sum of the shifted components are subtracted from the initial number of nuclei. Equation 3.17 defines the degraded component of the 642/643 keV transition as a function of time,

$$I_{fee.}^d = \Delta \times N_W + N_Y + N_A - \left(\left(\int_0^t \frac{dN_A}{dt} \right)_W + \left(\int_0^t \frac{dN_A}{dt} \right)_Y + \left(\int_0^t \frac{dN_A}{dt} \right)_A + (\Delta - 1) \left(\int_0^t \frac{dN_W}{dt} \right)_W \right) \quad (3.17)$$

where Δ is a control parameter and equal to 2 if the 642/643 keV transition is a doublet, otherwise $\Delta = 1$. Equation 3.18 defines the degraded component of the 516 keV transition as a function of time.

$$I_{dep.}^d = N_W + N_Y + N_A - \left(\left(\int_0^t \frac{dN_B}{dt} \right)_W + \left(\int_0^t \frac{dN_B}{dt} \right)_Y + \left(\int_0^t \frac{dN_B}{dt} \right)_A \right) \quad (3.18)$$

The final formulation of the model is achieved by substituting Equation 3.17 and Equation 3.18 into Equation 3.16 for $I_{fee.}^d$ and $I_{dep.}^d$, respectively.

This model has been used to explore the scenarios outlined earlier. Figure 3.11 shows the variation of state B (4^+ state) as a function of the half-life of state Y (12^+ state) using the input parameters listed in Table 3.5. The input parameter for the half-life of state B was chosen to be 3.8 ps in the model to ensure the $B(E2)_{4^+/2^+}$ ratio is 1. Hence, the calculation leads to a lifetime of the 4^+ state to be 5.47 ps. Figure 3.11 (a) shows that as the lifetime of the 12^+ increases there is a corresponding increase in the lifetime of the 4^+ state. The half-life of state Y (12^+)

Table 3.5: Parameter definitions in the model. Relative gamma-ray intensities extracted from recoil-correlated γ -ray coincidences have been used to define the N_W , N_Y and N_A .

N_W	N_Y	N_A	$t_{1/2}^W$	$t_{1/2}^A$	$t_{1/2}^B$
35	22.5	34.5	1	4	3.8

in the $7 \leq t_{1/2}^Y < 2000$ ps range has a significant effect on the measured half-life of state B half-life (4^+ half-life). If the fragmented structure of the 12^+ state in ^{168}Os and the evolution of the shifted and degraded components as a function of target-to-degrader distance are considered, it is seen that the 12^+ state (state Y in the model) has a half-life of the order of ns. Figure 3.11(a) shows that the apparent half-life of state B is equal to 10 ps when the state Y has a half-life above ns. The half-life value ($t_{1/2} = 10$ ps) of state B produced by the model is equal to the measured half-life value of the 4^+ state in ^{168}Os . This supports the hypothesis that when the 642/643 doublet straddles the 12^+ state, it has an effect on the apparent half-life of state B.

Figure 3.11(b) shows the lifetime of the 4^+ state as a function of the 12^+ state lifetime in the absence of a doublet. Figure 3.11(b) suggests that a short-lived isomeric state without a doublet would have little effect on the lifetime of the 4^+ state measured with the DDCM technique.

The effect of the doublet 516 keV has been tested in a more complicated model, which revealed the doublet of depopulator has no significant effect on the apparent lifetime of the state B. The 516 keV and 640 keV also belong to the nuclide ^{167}Re , which is also produced in the fusion evaporation reaction used in this analysis and contaminates the recoil-correlated γ -ray spectrum. The model has been used to assess the effect of contamination peaks from ^{167}Re . This model indicates that this kind of contamination would shorten the apparent lifetime of the state B and consequently has no impact on the measurement made by Grahn *et al.* [1].

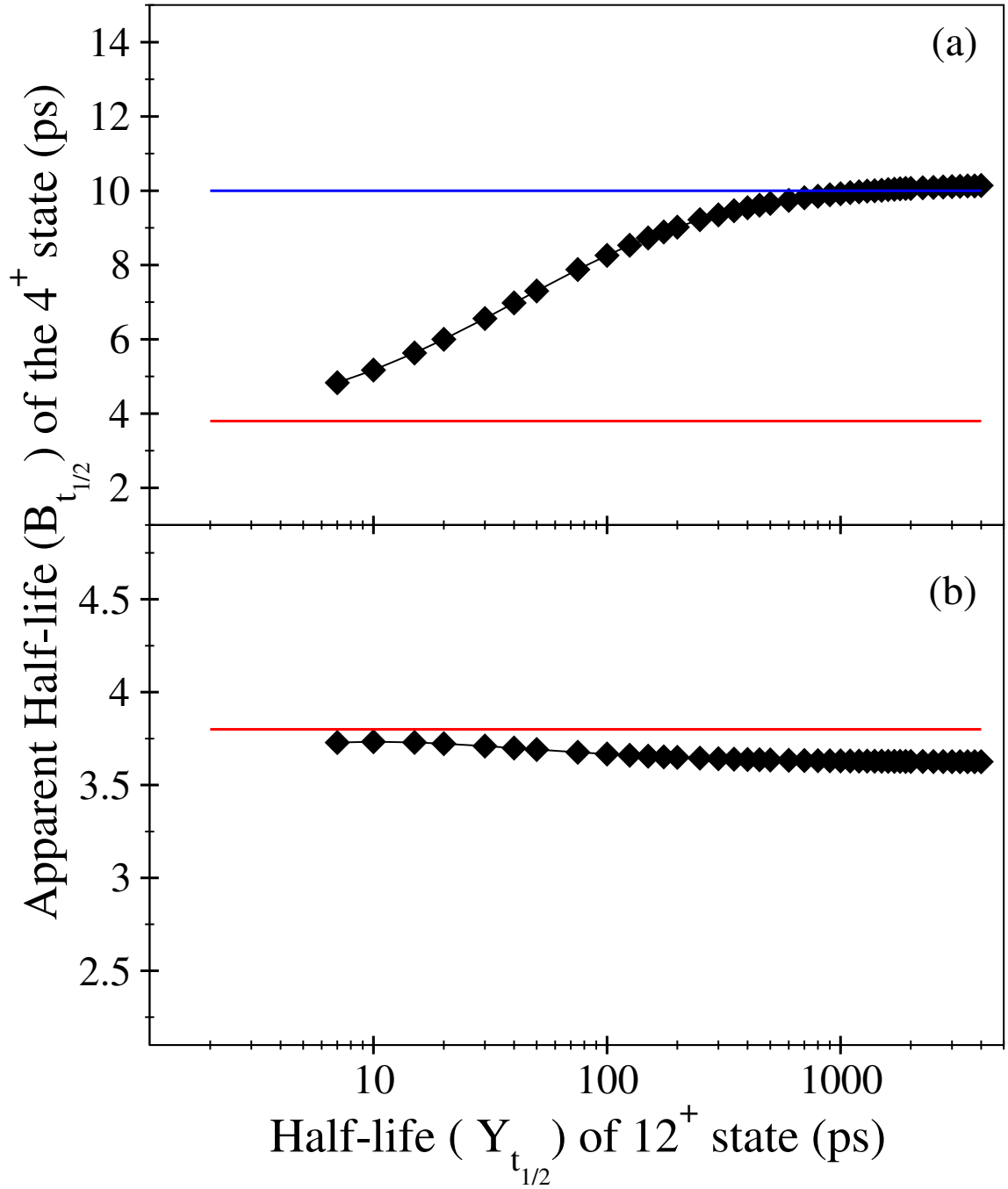


Figure 3.11: Variation in the apparent half-life of state B (4^+) as a function of the half-life of the state Y (12^+). (a) The effect of a doublet with components above state Y. (b) The variation as a function of the half-life of state Y without a straddling doublet. Blue line indicates the measured half-life of the 4^+ state by Grahn *et al.* [1]. Red line indicates the half-life value of the state B(the 4^+ state) have been extracted from calculation for a ratio of $B(E2)_{4^+/2^+} = 1$.

3.5 Summary

This chapter reports the results of an experiment performed at the JYFL Accelerator Laboratory. The reaction $^{92}\text{Mo}(^{78}\text{Kr},4\text{p})$ at bombarding energies of ~ 335 and ~ 348 MeV Kr^{15+} beam populated new excited states in the neutron-deficient nuclide ^{168}Os . Gamma-ray coincidences in delayed coincidence with recoiling fusion evaporation residues revealed extensions to known band structures, two new decay paths from the 12^+ state and a new positive-parity band structure. Three self-coincident doublets were revealed in this analysis. These new features were investigated in a model using the Bateman equations and based on the DDCM method to search for possible explanations for the anomalous $B(E2)_{4+/2+}$ ratios for ^{168}Os extracted from recent lifetime measurements by Grahn *et al.* [1]. It is concluded that the 642/643 doublet that straddles the 12^+ , which is assumed to have a relatively long lifetime from its fragmented decay path, has the effect of lengthening the lifetime of the 4^+ state. Thus the anomalous $B(E2)_{4/2}$ ratios could arise from the measurement of an *apparent* lifetime, which is complicated by the unique structural features of ^{168}Os .

Chapter 4

Lifetime measurements of excited states in ^{166}W

Recent lifetime measurements for the 2^+ and 4^+ states in the neutron-deficient nuclide $^{168}\text{Os}_{92}$ have yielded a $B(E2)_{4^+/2^+}$ ratio with an anomalously small value. The motivation for this work is to find out whether this anomaly is a special case for ^{168}Os or it affects other nuclei in this region of the Segre Chart. This chapter represents the results of the first lifetime measurement of low-lying excited states in the $N = 92$ isotone ^{166}W performed at the Accelerator Laboratory of the University of Jyväskylä. The lifetimes have been measured using the Recoil Distance Doppler-shift method in conjunction with recoil tagging techniques. Reduced transition probabilities of the excited 2^+ , 4^+ , 6^+ , 12^+ and 14^+ states were extracted for the first time. Strikingly, the analysis of this work revealed a $B(E2; 4^+ \rightarrow 2^+)/B(E2; 2^+ \rightarrow 0^+)$ ratio less than unity.

4.1 Introduction

The neutron-deficient nuclide ^{166}W , which lies 10 neutrons above the $N = 82$ closed shell, was first identified by Toth *et al.* in α -decay studies [93]. The α -decay energy was measured to be $E_\alpha = 4.739(3)$ MeV and has a 19.6(12) s half-life. The nucleus decays predominantly by β emission and the α -decay branching ratio is measured to be 0.03(1)% [94]. Excited states in ^{166}W were established by Gerl *et al.* [95] up to 26^+ for the yrast band and up to 19^- in a negative-parity band. Subsequent work by Simpson *et al.* extended the level scheme to higher spin and found a second negative-parity side band [96]. Cranked shell model calculations were used to assign configurations to the yrast and side bands. The ground-state band is interpreted as a zero quasiparticle band, which is crossed by a configuration based on an aligned $(i_{13/2})^2$ neutron pair. The side-bands are interpreted as two-quasineutron configurations formed by coupling the $i_{13/2}$ neutron to one of the negative-parity orbitals originating from the mixed $(f_{7/2}, h_{9/2})$ quasineutron orbitals. The excitation energy ratio $E(4^+)/E(2^+)$ of ^{166}W is equal to 2.68, which is close to the ideal value of 2.5 for a γ -soft rotor. Hence the shape of ^{166}W is sensitive to the occupation of core polarising orbitals at the Fermi surface. This chapter reports the first lifetime measurements of excited states in ^{166}W , which provide an insight on the collectivity of this nucleus in the transitional region between collective and single-particle regimes.

4.2 Experimental Details

Excited states in ^{166}W were populated using the reaction $^{92}\text{Mo}(^{78}\text{Kr}, 4p)$. The ~ 380 MeV Kr^{15+} beam was accelerated by the K130 cyclotron at the Accelerator Laboratory at the University of Jyväskylä (JYFL) and bombarded a 0.6 mg/cm² ^{92}Mo target. A nominal beam intensity of 3 pA was delivered to the target. The reaction provided an initial recoil velocity of $v/c = 4.3\%$. The γ rays emitted by the recoiling

Table 4.1: Calculated energy separation of the fully Doppler-shifted and degraded components of excited states in ^{166}W recorded at 158° and 134° using the velocities before and after degrader. The v/c is equal to 4.3% before the degrader and v/c equals to 3.4% after the degrader.

$I_i^\pi \rightarrow I_f^\pi$	$E_\gamma(\text{keV})$	$\Delta E (\text{keV})$ at 158°	$\Delta E (\text{keV})$ at 134°
$2^+ \rightarrow 0^+$	252	2.19	1.62
$4^+ \rightarrow 2^+$	424	3.68	2.73
$6^+ \rightarrow 4^+$	550	4.78	3.5
$12^+ \rightarrow 10^+$	480	4.17	3.09
$14^+ \rightarrow 12^+$	326	2.83	2.1

nuclei were detected by the JUROGAMII Ge detector array consisting of 15 Phase 1-type [58] and 24 Compton suppressed HPGe segmented Clovers detectors [59]. A plunger device, DPUNS [56] was installed at the JUROGAMII target position in order to employ the Recoil Distance Doppler-Shift (RDDS) technique [68, 67]. Table 4.1 lists the energy separation of the fully Doppler-shifted and degraded components of the transitions under investigation. A 1 mg/cm^2 thick Mg degrader was employed to let reaction products recoil into the gas-filled separator RITU [97, 98, 62] and be transported to the focal plane. At the focal plane recoils were implanted into the DSSDs GREAT [55] spectrometer at the focal plane of RITU. A MWPC was used to record the energy loss and time signal information produced by the recoils and unreacted beam. The time-of-flight and energy loss information from the MWPC and DSSDs were used to discriminate fusion evaporation residues from scattered beam. The GREAT triggerless data acquisition (TDR) system [99] was utilised to collect data time stamped to a precision of 10 ns. The data analysis software package GRAIN [85] was used to acquire γ -ray spectra in delayed coincidence with implanted recoils and NAPATAU software for the Differential Decay Curve Method (DDCM) [69, 70, 16] was employed.

4.3 Results

4.3.1 The 2^+ , 4^+ and 6^+ states

The lifetimes of the 2^+ , 4^+ and 6^+ excited states for ^{166}W have been determined for the first time. Recoil distance Doppler shift measurements were made at nine target-to-degrader distances ranging from 5 μm to 8000 μm as listed in Table 4.2. Gamma-ray coincidences correlated with recoil implantations at the focal plane were sorted into separate asymmetric two-dimensional matrices for the detectors at 158° or 134° versus all detector angles and for each target-to-degrader distance.

It was not possible to select coincidences with the direct feeding transitions for the 2^+ , 4^+ and 6^+ states due to γ rays with similar energies in other parts of the ^{166}W level scheme. There were sufficient statistics to allow coincidences to be demanded with the higher lying transitions at 480 keV and 686 keV. The shifted and degraded components at specific angles were obtained by demanding coincidences on the 'all angle' axis and the resulting spectra analysed to extract the normalised shifted decay curves. The validity of this method has been demonstrated in Ref [100]. For these lifetime measurements only the detectors at 158° (five detectors) and 134° (10 detectors) relative the beam direction were used. The limits of the each gate were fixed for each target-to-degrader distance. Figure 4.1, Fig. 4.2 and Fig. 4.3 show typical coincidence spectra for the depopulating and feeding transitions of the 2^+ , 4^+ and 6^+ states in ^{166}W , respectively.

The fitted peaks were normalised to the summed intensities of the fully shifted and degraded components. The lifetime of the level of interest, determined by indirect gating, was extracted using

$$\tau(x) = \frac{\{C, A_d\} - \alpha\{C, B_d\}}{v \frac{d}{dx}\{C, A_s\}} \quad (4.1)$$

Table 4.2: List of the target-to-degrader distances

No	Target-to-Degrader Distance
1	5 μm
2	100 μm
3	200 μm
4	500 μm
5	1000 μm
6	2000 μm
7	3000 μm
8	5000 μm
9	8000 μm

Table 4.3: Lifetimes and reduced transition probabilities of the low-lying 2^+ , 4^+ and 6^+ yrast states in ^{166}W .

$E_\gamma[\text{keV}]$	$I_i^\pi \rightarrow I_f^\pi$	$\tau(\text{ps})$	$B(E2)[e^2b^2]\downarrow$	$B(E2)[\text{W.u.}]$
252	$2^+ \rightarrow 0^+$	86(6)	0.81(0.05)	150(9)
424	$4^+ \rightarrow 2^+$	21(3)	0.27(0.03)	50(7)
550	$6^+ \rightarrow 4^+$	16(4)	0.09(0.02)	18(4)

where A_d , B_d and A_s are the quantities in coincidence with transition C that correspond to the degraded component of the depopulating transition, the degraded component of the feeding transition of the level of interest and the shifted component of the depopulating transition, respectively. The α parameter is the branching ratio, which for a gating transition in a cascade is unity. The fitted peak areas from the projected spectra at both 158° and 134° were normalised by $I_s/(I_s + I_d)$ and used to extract lifetimes. The DDCM was applied to the normalised shifted curves separately to obtain lifetimes for levels of interest. Figure 4.4, 4.5 and 4.6 show the normalised shifted curves of 2^+ , 4^+ and 6^+ states recorded at 134° and 158° . The error-weighted average lifetimes of these states and reduced transition probabilities are given in Table 4.3.

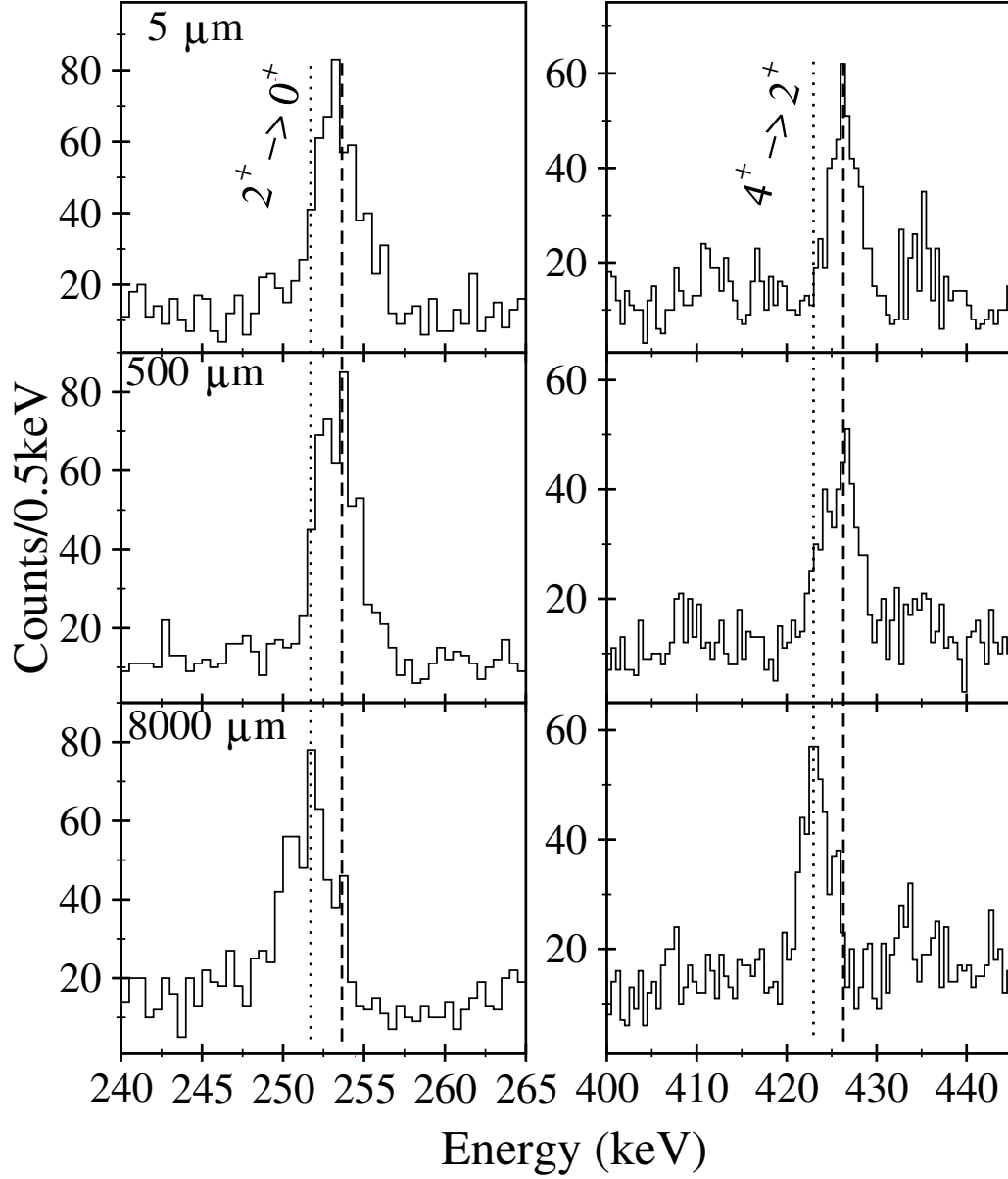


Figure 4.1: Typical recoil-gated γ - γ -coincidence spectra of ^{166}W recorded at three target-to-degrader distances with the 10 JUROGAMII detectors at 134° . The evolution of the shifted and the degraded components is shown as a function of target-to-degrader distance for depopulator (left column) and feeder (right column) transitions of the 2^+ state in ^{166}W . The dotted and dashed lines indicate the position of the fully shifted and degraded components of the depopulating transition, respectively.

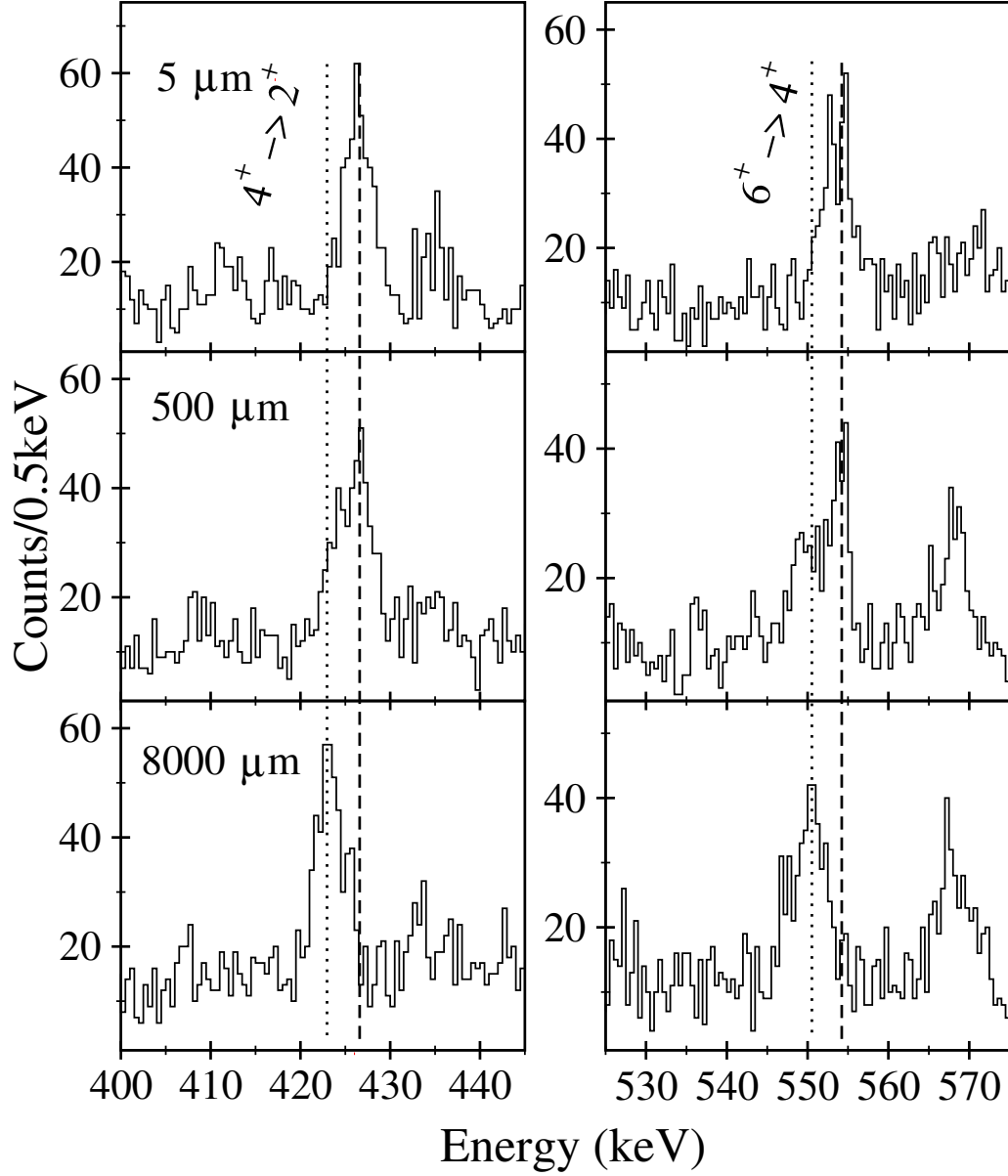


Figure 4.2: Typical recoil-gated γ - γ -coincidence spectra of ^{166}W recorded at three target-to-degrader distances with the 10 JUROGAMII detectors at 134° . The evolution of the shifted and the degraded components is shown as a function of target-to-degrader distance for depopulator (left column) and feeder (right column) transitions of the 4^+ state in ^{166}W . The dotted and dashed lines indicate the position of the fully shifted and degraded components of the depopulating transition, respectively.

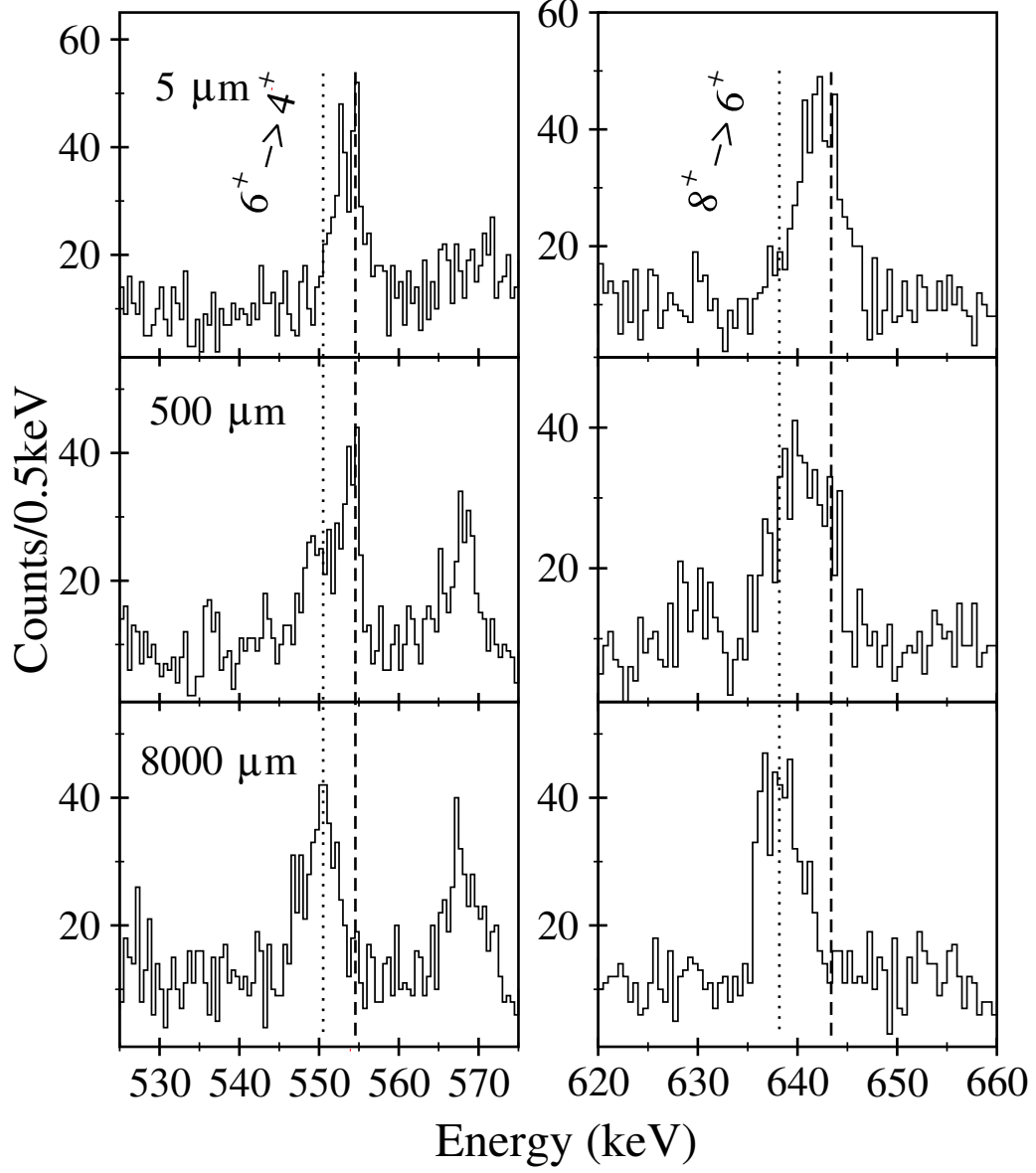


Figure 4.3: Typical recoil-gated γ - γ -coincidence spectra of ^{166}W recorded at three target-to-degrader distances with the 10 JUROGAMII detectors at 158° . The evolution of the shifted and the degraded components is shown as a function of target-to-degrader distance for depopulator (left column) and feeder (right column) transitions of the 6^+ state in ^{166}W . The dotted and dashed lines indicate the position of the fully shifted and degraded components of the depopulating transition, respectively.

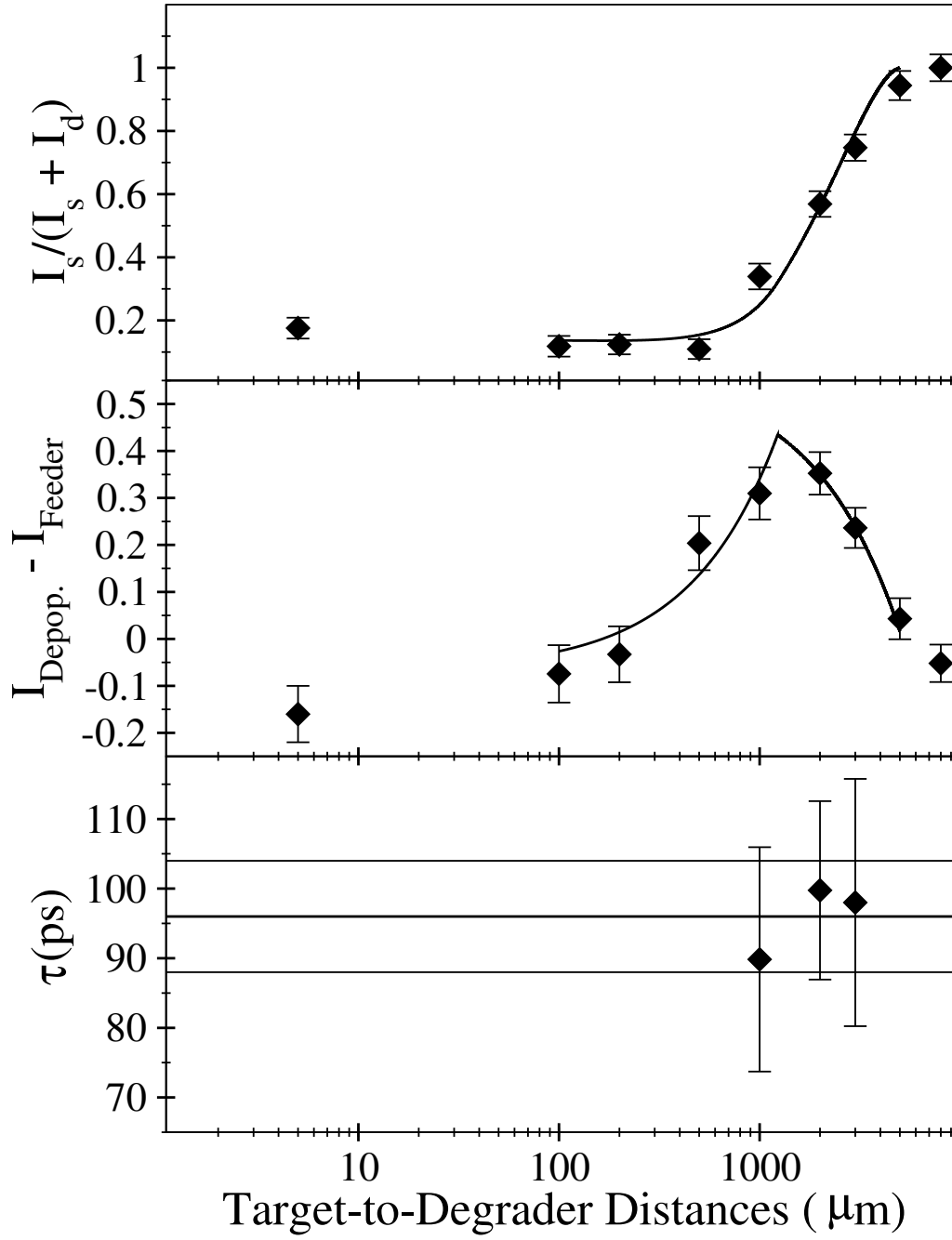


Figure 4.4: A graph illustrating the principles of the DDCM. Top panel shows the normalised shifted curve of the 2^+ state of ^{166}W extracted from spectra recorded by detectors placed at 134° . Middle panel shows the intensity difference of the direct feeding and depopulating transition and the solid line is the derivative of the curve shown in the upper panel. Bottom panel shows the lifetime τ as a weighted mean of values τ .

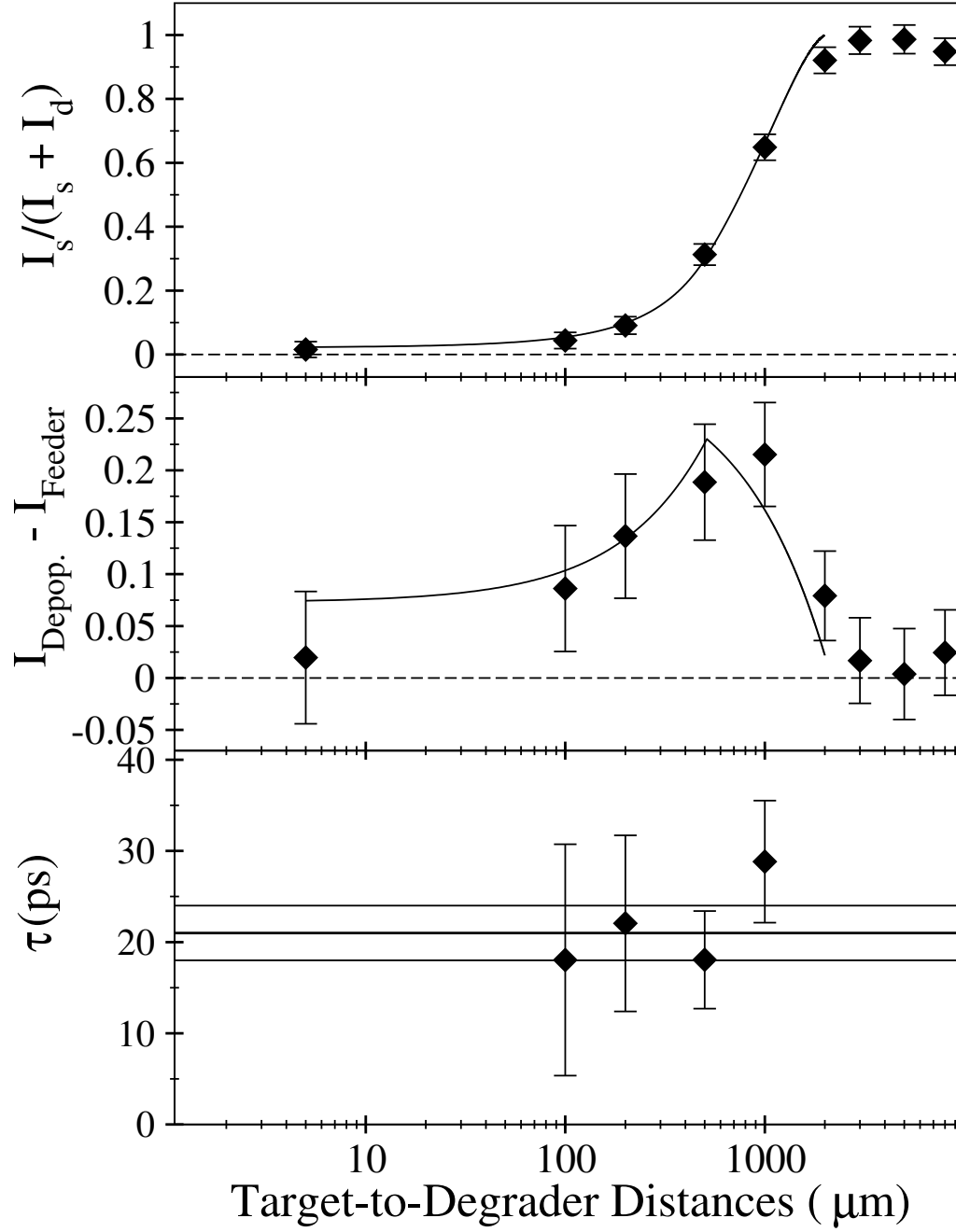


Figure 4.5: A graph illustrating the principles of the DDCM. Top panel shows the normalised shifted curve of the 4^+ state of ^{166}W extracted from spectra recorded by detectors placed at 134° . Middle panel shows the intensity difference of the direct feeding and depopulating transition and the solid line is the derivative of the curve shown in the upper panel. Bottom panel shows the lifetime τ as a weighted mean of values τ .

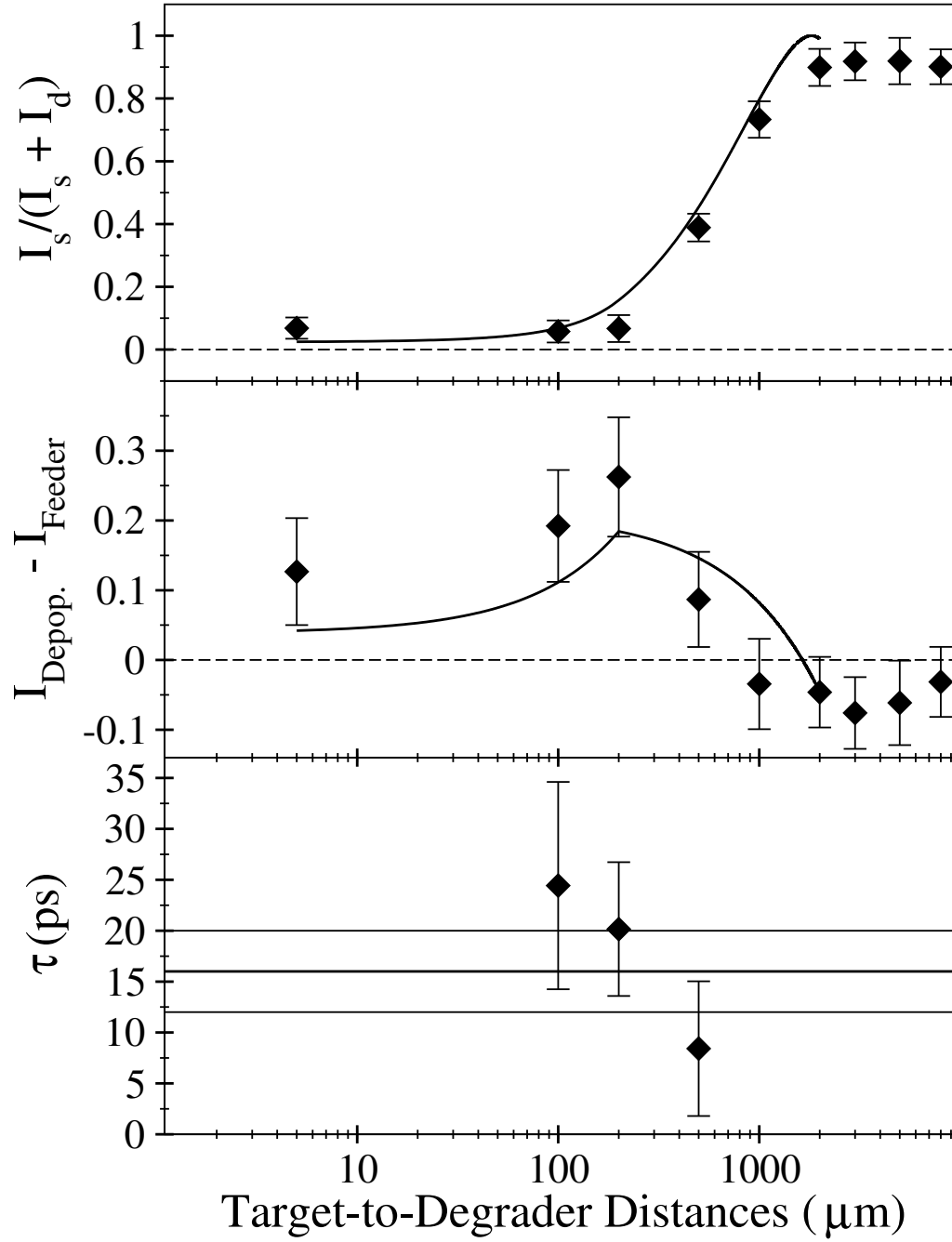


Figure 4.6: A graph illustrating the principles of the DDCM. Top panel shows the normalised shifted curve of the 6^+ state of ^{166}W extracted from spectra recorded by detectors placed at 158° . Middle panel shows the intensity difference of the direct feeding and depopulating transition and the solid line is the derivative of the curve shown in the upper panel. Bottom panel shows the lifetime τ as a weighted mean of values τ .

4.3.2 The 12^+ and 14^+ states

In order to extract the lifetimes of the 12^+ and 14^+ states, the analysed data set used the nine distances between 5 μm to 8000 μm , see Table. 4.2. Gamma-ray coincidences correlated with a recoil implantation at the focal plane were sorted into a two-dimensional matrix. Spectra for the feeding and depopulating transitions were obtained by demanding coincidences with the direct feeding transitions. The gate limits for coincidences were fixed for each transition at all target-to-degrader distances. Spectra were generated using γ rays detected at 158° or 134° for each distance. The low statistics required coincidences to be demanded with the full line shape of the direct feeder. The lifetimes of the 12^+ and 14^+ states were determined using

$$\tau(x) = \frac{\{B, A_d\} - \alpha\{A, B_d\}}{v \frac{d}{dx} \{B, A_s\}} \quad (4.2)$$

where A is the depopulating transition and B is the feeding transition of the level of interest. The parameter $\{B, A\}$ represents the intensity of A in coincidence with transition B , A_d is the degraded component and A_s is the shifted component of the depopulating transition of the level of interest. α is the branching ratio. The degraded component of the feeding transition, B_d , must be considered in order to extract lifetimes from the direct gating method. The validity of this method was demonstrated in Refs [18, 101]. An internal normalisation was applied to the fitted peak areas using the summed intensities of degraded and fully shifted components of the transition of interest in order to avoid errors arising from the time and beam intensity differences between individual distances. The mean lifetimes, τ , were extracted from the normalised shifted components fitted separately to the 158° and 134° spectra using DDCM for each distance. The resulting lifetimes are weighted averages of lifetimes extracted within the region of sensitivity. Evolution

Table 4.4: Reduced transition probability of the 12^+ and 14^+ states in ^{166}W extracted from the present lifetime measurement.

$E_\gamma[\text{keV}]$	$I_i^\pi \rightarrow I_f^\pi$	$\tau(\text{ps})$	$B(E2)[e^2b^2]\downarrow$	$B(E2)[\text{W.u.}]$
480	$12^+ \rightarrow 10^+$	27(4)	0.11(0.01)	21(3)
326	$14^+ \rightarrow 12^+$	21(2)	0.98(0.08)	182(16)

of the shifted and degraded components as a function of target-to-degrader distance for depopulator and feeder transition of the 12^+ state in ^{166}W with 10 JUROGAMII detectors at 134° is given in Figure 4.7. The dotted and dashed lines indicate the position of the fully shifted and degraded components of the depopulating transition, respectively. The normalised shifted curve of the 480 keV transition which is fitted with experimental data point using three second order polynomials, the intensity difference of the degraded component of the direct feeding and depopulating transition and the lifetime τ as a weighted mean of values τ are shown in Figure 4.8. The time evolution of the shifted and degraded components as a function of target-to-degrader distance for depopulator and feeder transition of the 14^+ state in ^{166}W with 10 JUROGAMII detectors at 134° is given in Figure 4.9. The dotted and dashed lines indicate the position of the fully shifted and degraded components of the depopulating transition, respectively. The normalised shifted curve of the 480 keV transition which is fitted with experimental data point using two second order polynomials, the intensity difference of the degraded component of the direct feeding and depopulating transition and the lifetime τ as a weighted mean of values τ are shown in Figure 4.10. Table 4.4 summarises the result obtained in the present work for the 12^+ and 14^+ .

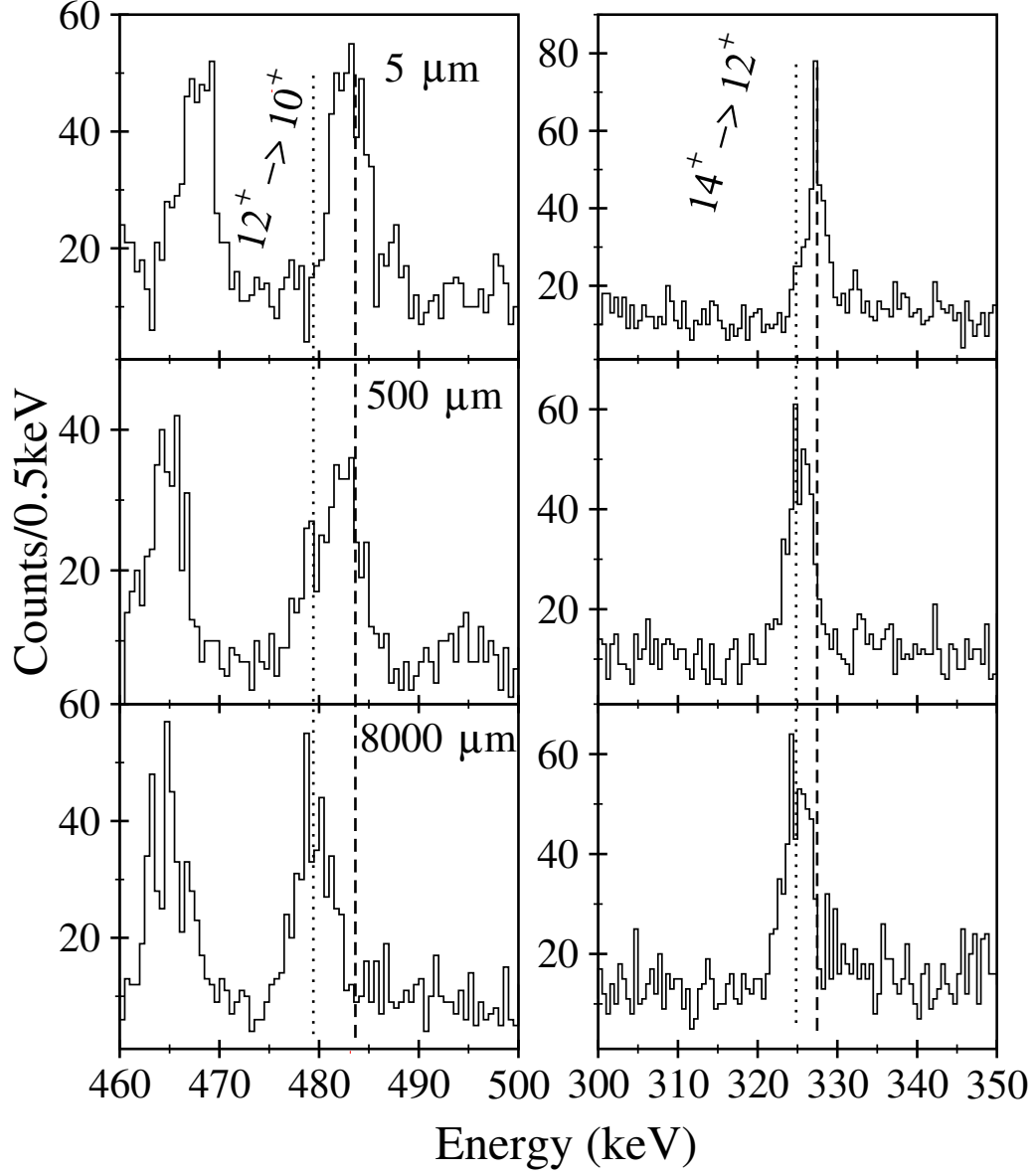


Figure 4.7: Evolution of the shifted and degraded components as a function of target-to-degrader distance for depopulator and feeder transition of the 12^+ state in ^{166}W with 10 JUROGAMII detectors at 134° . The dotted and dashed lines indicate the position of the fully shifted and degraded components of the depopulating transition, respectively.

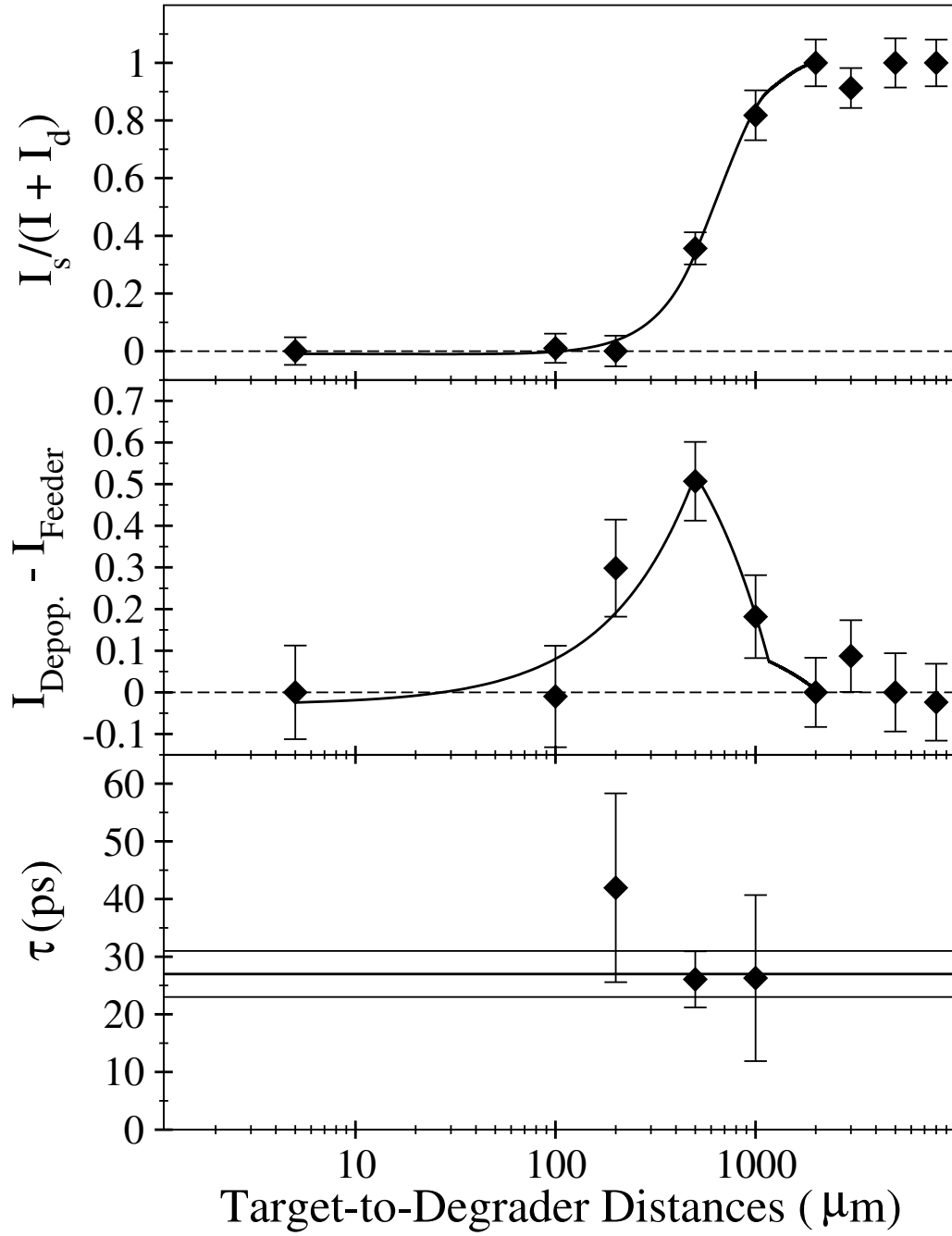


Figure 4.8: A graph illustrating the principles of the DDCM. Top panel shows the normalised shifted curve of the 12^+ state of ^{166}W extracted from spectra recorded by detectors placed at 134° . Middle panel shows the intensity difference of the degraded component of the direct feeding and depopulating transition and the solid line is the derivative of the curve shown in the upper panel. Bottom panel shows the lifetime τ as a weighted mean of values τ .

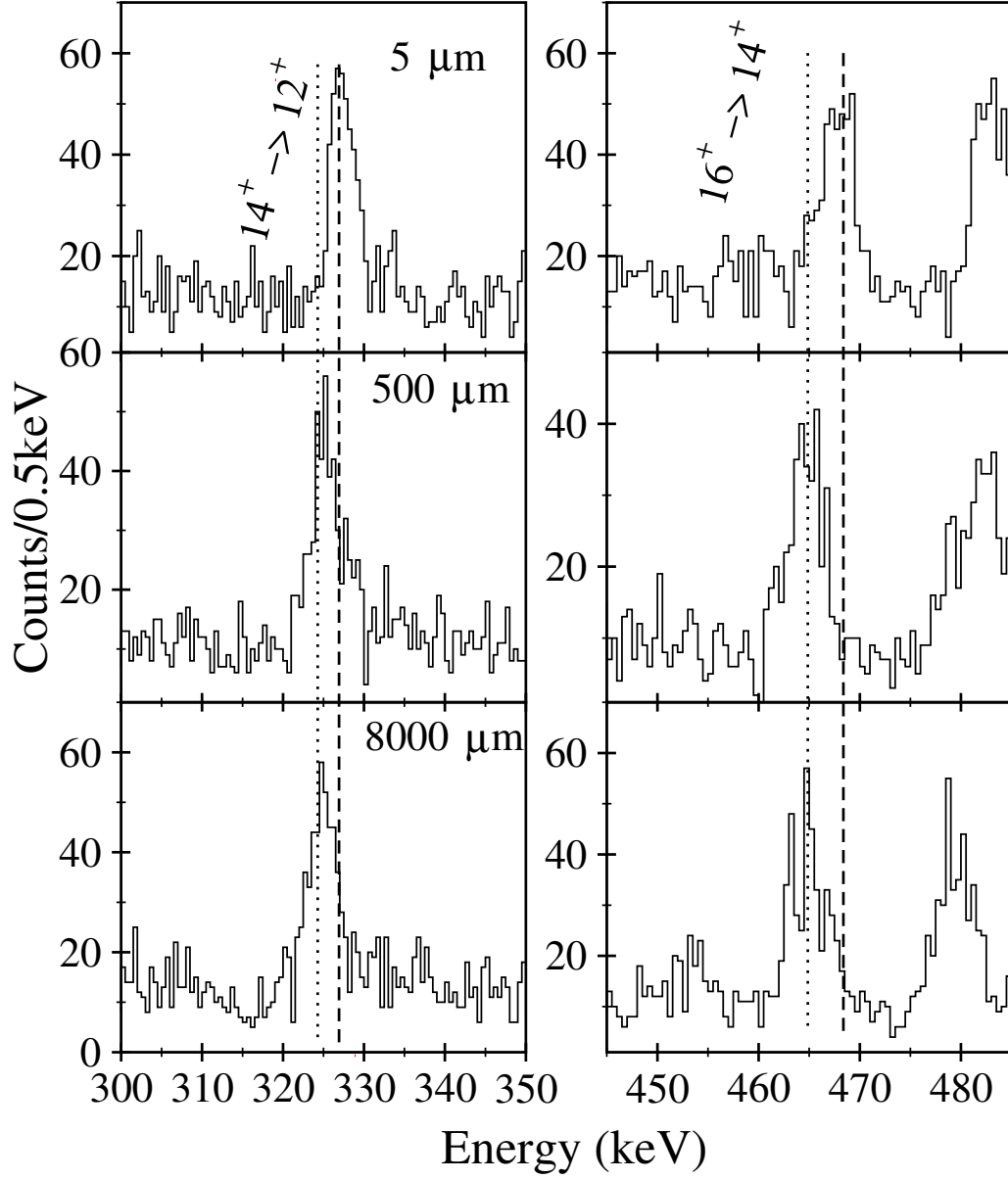


Figure 4.9: Evolution of the shifted and degraded components as a function of target-to-degrader distance for depopulator and feeder transition of the 14^+ state in ^{166}W with 10 JUROGAMII detectors at 134° . The dotted and dashed lines indicate the position of the fully shifted and degraded components of the depopulating transition, respectively.

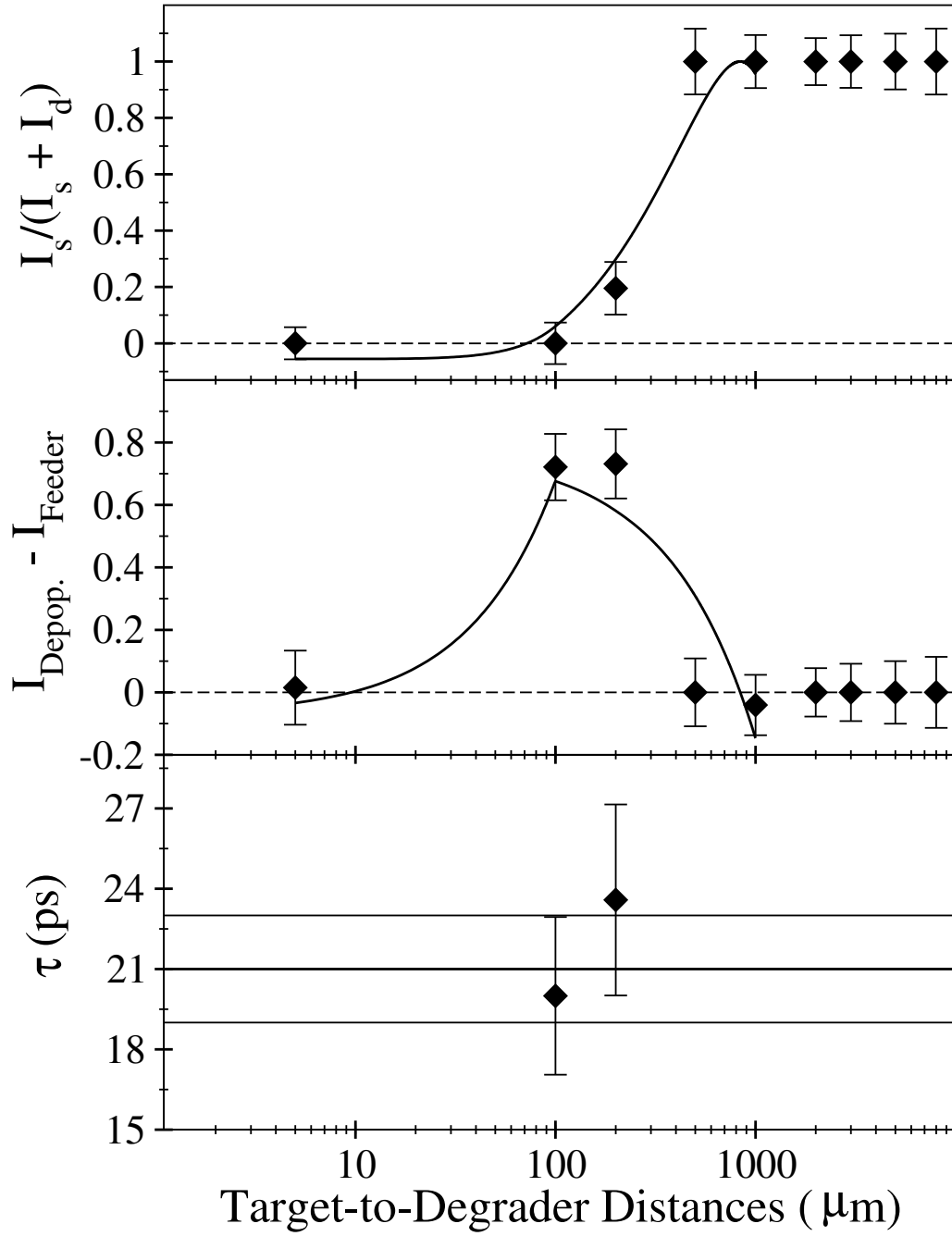


Figure 4.10: A graph illustrating the principles of the DDCM. Top panel shows the normalised shifted curve of the 14^+ state of ^{166}W extracted from spectra recorded by detectors placed at 134° . Middle panel shows the intensity difference of the degraded component of the direct feeding and depopulating transition and the solid line is the derivative of the curve shown in the upper panel. Bottom panel shows the lifetime τ as a weighted mean of values τ .

4.4 Discussion

4.4.1 Reduced Transition Probabilities

The ratio of reduced transition probabilities $B(E2)_{4+/2+} = 0.33(5)$ extracted from the lifetime measurements in ^{166}W is anomalously low. The recent lifetime measurements in the $N = 92$ isotone ^{168}Os cited in the previous chapter also yields a similar ratio with $B(E2)_{4+/2+} = 0.36(11)$. The origin of the anomaly is puzzling since ^{166}W is located 8 protons and 10 neutrons away from the nearest closed shells and features related to seniority and shape coexistence are not anticipated. Figure 3.7 shows the $E_{4+/2+}$ excitation energy ratio of the 4^+ and 2^+ states and displays a smoothly varying trend for the W isotopes as a function of neutron number. Unlike the Pt and Os isotopes there is no indication of perturbed levels in the W isotopes due to the mixing of ground-state and deformed-bands [102]. The W systematics follow a clear trend of decreasing $E_{4+/2+}$ ratio with decreasing neutron number, which corresponds to the transition from a well-deformed prolate structure at the neutron midshell ($N = 104$) towards a weakly deformed shape near the closed shell ($N = 82$). Figure 4.11(a) shows the variation of excitation energies of the 2^+ and 4^+ states in the W isotopes as a function of neutron number. A smooth variation of increasing 2^+ and 4^+ excitation energy is observed below $N = 98$ reflecting the change towards a lower average deformation near the closed neutron shell.

An inverse behaviour in the $B(E2)$ values as a function of decreasing neutron number from the neutron midshell to the closed shell is expected [90]. Figure 4.11(b) shows the variation of the reduced transition probabilities $B(E2; 2^+ \rightarrow 0^+)$ as a function of neutron number. The $B(E2; 2^+ \rightarrow 0^+)$ values are approximately 190 W.u. around the neutron midshell and dip to 100 W.u. at $N = 94$. The $B(E2; 2^+ \rightarrow 0^+)$ value extracted for $^{166}\text{W}_{92}$ shows an increase to 150(9) W.u. This seems at variance to the expectation suggested by Figure 4.11(a), which shows a smooth

increase in excitation energy corresponding to a decrease in average deformation approaching the closed $N = 82$ shell. The higher deformation in ^{166}W then ^{168}W in the 2^+ state is a possible source the anomalous $B(E2)_{4^+/2^+}$ ratio in ^{166}W , since the 2^+ state is more deformed then it is expected.

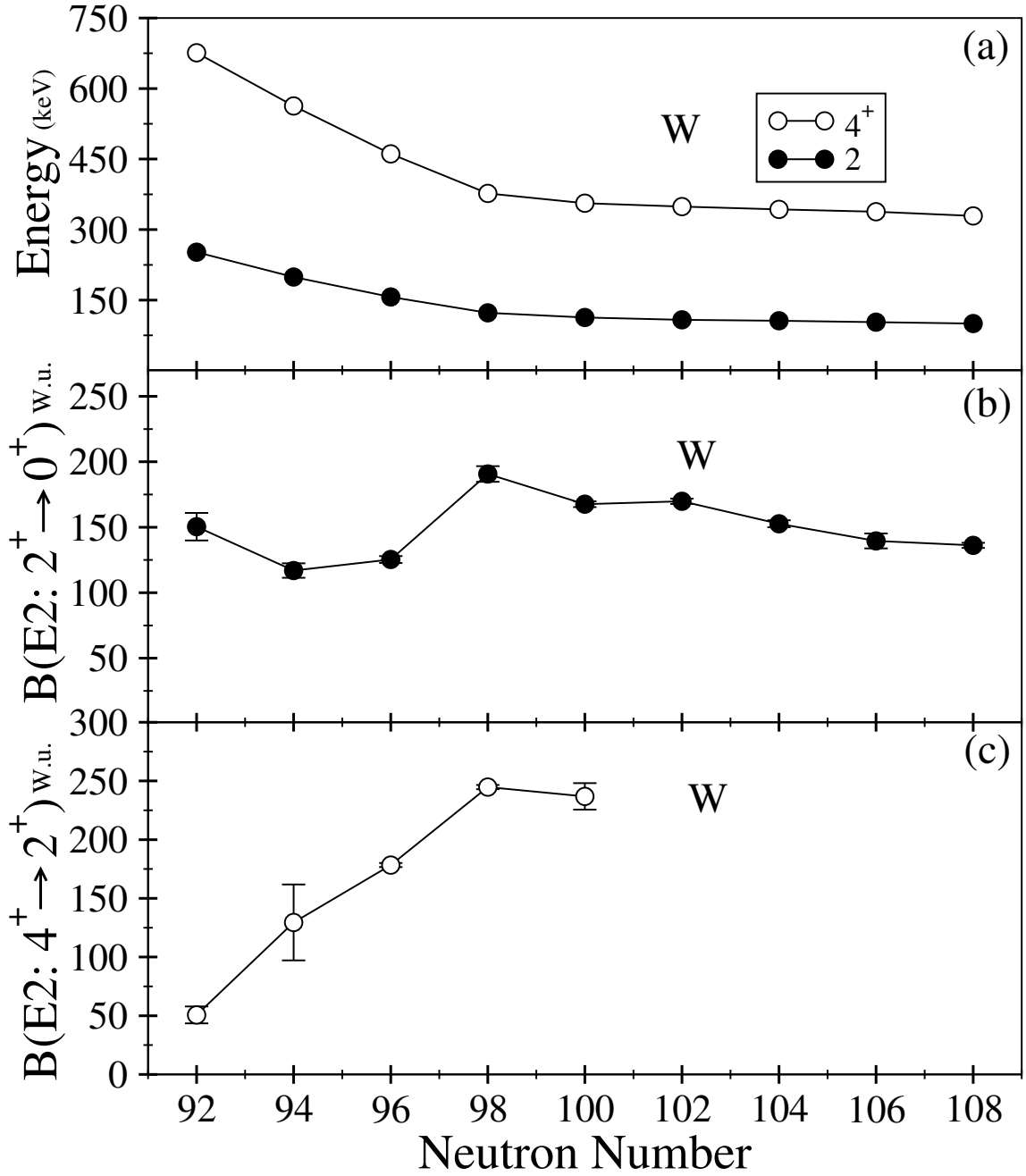


Figure 4.11: (a) Excitation energies of the 2^+ and 4^+ states as a function of neutron number for the W isotopes. (b) Experimental reduced transition probabilities $B(E2; 2^+ \rightarrow 0^+)$ as a function of neutron number for the W isotopes. (c) Experimental reduced transition probabilities $B(E2; 4^+ \rightarrow 2^+)$ as a function of neutron number for the W isotopes. Data for excitation energies from National Nuclear Data Center (NNDC). τ of the 2^+ state in ^{172}W and ^{178}W [90], ^{174}W [91] and ^{176}W [92]. ^{166}W from present work and τ of the 4^+ state from National Nuclear Data Center (NNDC).

The corresponding figure for the $B(E2; 4^+ \rightarrow 2^+)$ value shows a smooth decrease below the neutron midshell where the maximum collectivity is expected. A comparison of the reduced transition probabilities, $B(E2; 4^+ \rightarrow 2^+)$, extracted for the W isotopes with the trends for other isotopic chains (see Figure 3.8) indicates the collectivity of the $4^+ \rightarrow 2^+$ state decreases at a faster rate in the W isotopes than might be expected for a deformed nucleus. In ^{168}Os , the observed anomaly in $B(E2)_{4^+/2^+}$ ratio is understood to arise from complications involving the decay of the 4^+ state. However, it appears that both the 2^+ and 4^+ state may cause the anomaly for ^{166}W .

In the theoretical framework of the collective model the relation between $B(E2; I \rightarrow I - 2)$ and $B(E2; 2 \rightarrow 0)$ is given by [50]

$$B(E2; I \rightarrow I - 2) = \frac{15I(I - 1)}{2(2I - 1)(2I + 1)} B(E2; 2^+ \rightarrow 0^+). \quad (4.3)$$

This relation yields the $B(E2; 4^+ \rightarrow 2^+) = 1.43B(E2; 2^+ \rightarrow 0^+)$ and $B(E2; 6^+ \rightarrow 4^+) = 1.57B(E2; 2^+ \rightarrow 0^+)$. However, the experimental ratios have been measured to be $B(E2)_{4^+/2^+} = 0.33(5)$ and $B(E2)_{6^+/2^+} = 0.12$. These ratios are compared with those of other nuclei with low ratios as a function of P -factor in Figure 4.12. The present measurements indicate that ^{166}W has unusually low $B(E2; I \rightarrow I - 2)/B(E2; 2^+ \rightarrow 0^+)$ ratios for a deformed nucleus.

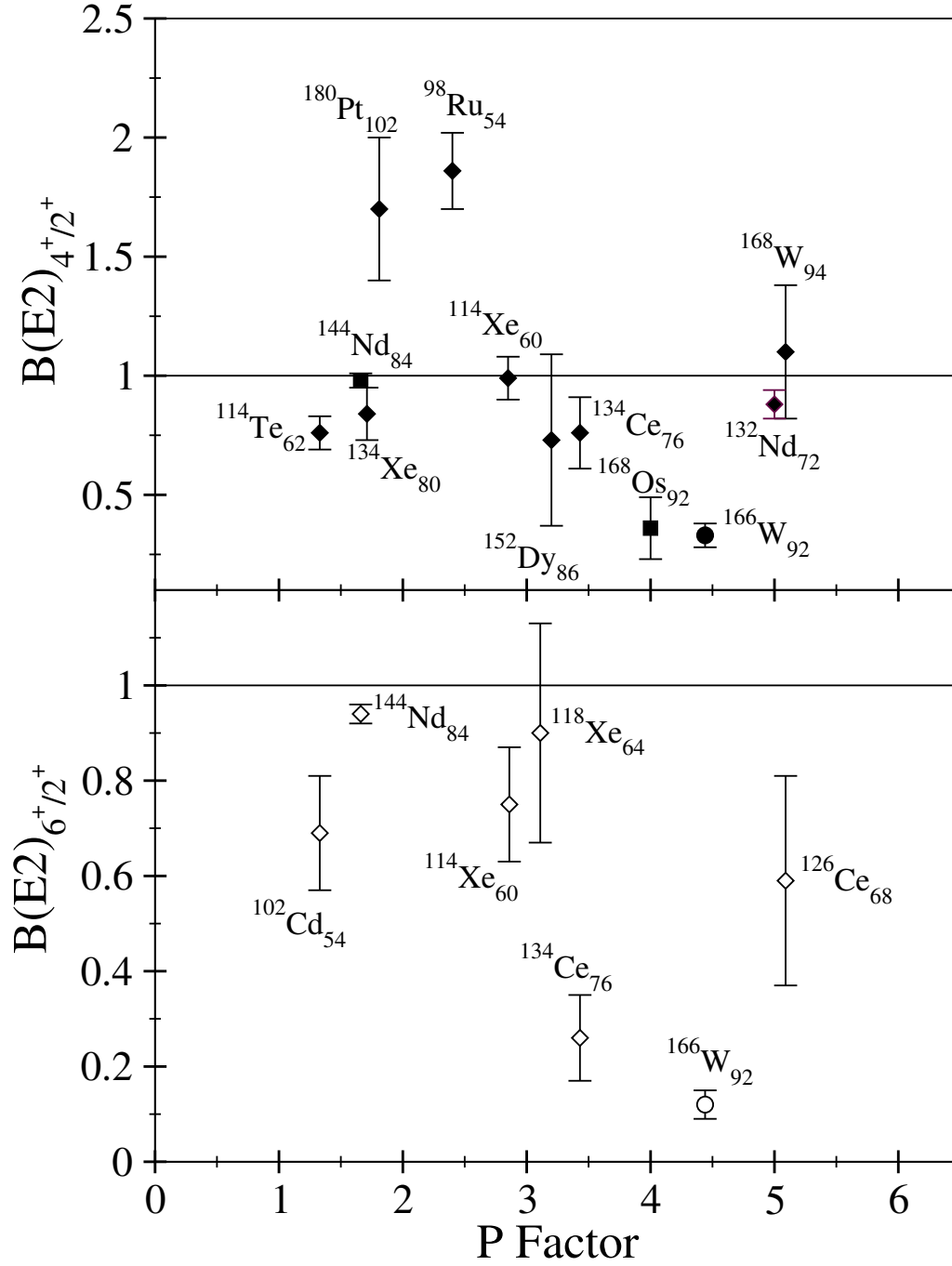


Figure 4.12: Experimental $B(E2)_{4+ / 2+}$ ratios as a function of P factor. At this point, it makes sense including ^{168}W , because it reveals a ratio less than unity by errors, relative to ^{152}Dy . Data from National Nuclear Data Center (NNDC). Exceptions are ^{168}Os [1], ^{166}W from present work, $^{98}\text{Ru}_{54}$ [23], $^{114}\text{Te}_{62}$ [26], $^{114}\text{Xe}_{60}$ [27], $^{134}\text{Xe}_{80}$ [28], $^{132}\text{Ce}_{74}$ [29], $^{134}\text{Ce}_{74}$ [30], $^{132}\text{Nd}_{72}$ [31], $^{144}\text{Nd}_{84}$ [25], $^{180}\text{Pt}_{102}$ [24].

4.4.2 The Level Scheme of ^{166}W

The level scheme of ^{166}W was examined using a thin target data set from a parallel experiment in order to determine whether the $\text{B}(\text{E}2)_{4+/2+}$ anomaly in ^{166}W has a similar structural origin as that proposed for ^{168}Os in the previous chapter. The $^{78}\text{Kr} + ^{92}\text{Mo}$ reaction at a bombarding energy of 357 MeV favours the $4p$ evaporation channel leading to ^{166}W over the lower beam energies used to identify extensions to the level scheme of ^{168}Os (see Table 3.2). Target thicknesses of 0.5 mg/cm^2 and 1.0 mg/cm^2 were irradiated for 172 hours and 26 hours, respectively. These data were sorted into a recoil-correlated $E_{\gamma 1} - E_{\gamma 2} - E_{\gamma 3}$ coincidence cube, which contained approximately 1.5×10^8 recoil correlated $\gamma\gamma\gamma$ events.

The anomalous $\text{B}(\text{E}2)_{4+/2+}$ ratio in ^{168}Os is proposed to arise from a γ -ray energy doublet that has components that straddle the 12^+ state. The lifetime measurements of Grahn *et al.* [1] do not measure a fully shifted component even for the longest target-degrader distances implying that the 12^+ state is relatively long-lived and consequently has a fragmented decay path to the ground-state band, the negative-parity side bands and the new non-yrast positive-parity band. The recoil-correlated cube was used to search for similar features. Figure 4.16 show the level scheme deduced from earlier work and confirmed in this thesis. The cube was analysed to investigate whether the the 252 keV ($2^+ \rightarrow 0^+$) and the 424 keV ($4^+ \rightarrow 2^+$) transitions were self-coincident doublets. Figure 4.13(a) shows γ rays in coincidence with 252 keV and 252 keV. It is clear from the spectrum that no such decay path involving two self-coincident 252 keV transitions exists in ^{166}W . Figure 4.13(b) shows the corresponding spectrum demanding a double gate on the 424 keV transitions. Gamma rays at 224 keV, 252 keV and 550 keV are apparent in this spectrum, however the 424 keV coincidence window is likely to overlap with the 421 keV transition, which forms part of the decay path from Band 1 to the ground state. Problems with this overlap have been eliminated in the lifetime measurement by

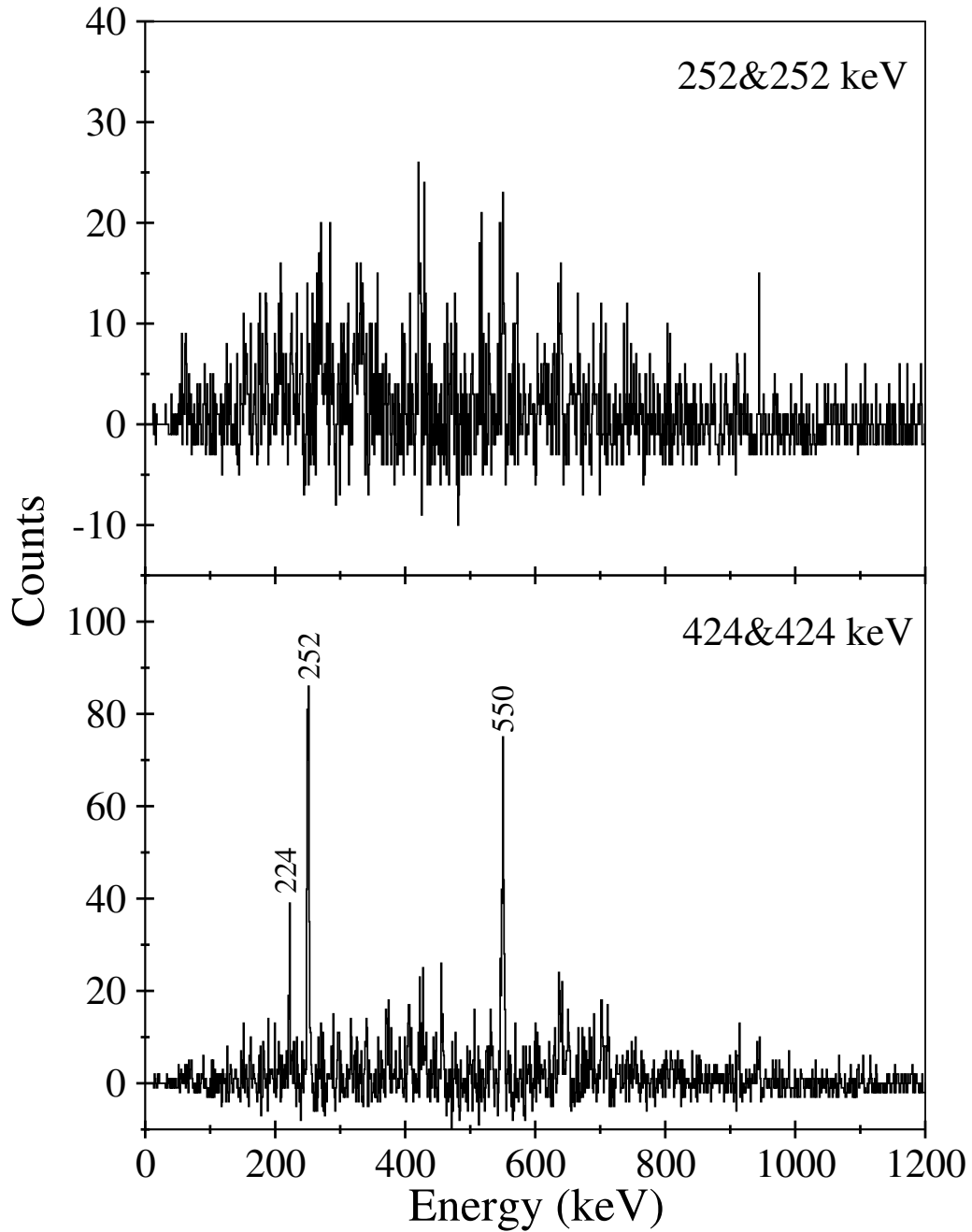


Figure 4.13: Double-gated γ -ray coincidence spectra correlated with a recoil implantation in the GREAT spectrometer. (a) spectrum showing γ rays in coincidence with the hypothesised 252 keV self-coincident doublet. (b) The 424 keV hypothesised doublet.

indirect gating on the 480 keV ($12^+ \rightarrow 10^+$) and 686 keV ($10^+ \rightarrow 8^+$) transitions in the yrast band.

Figure 4.14 shows typical double γ -ray coincidences that were used to search for

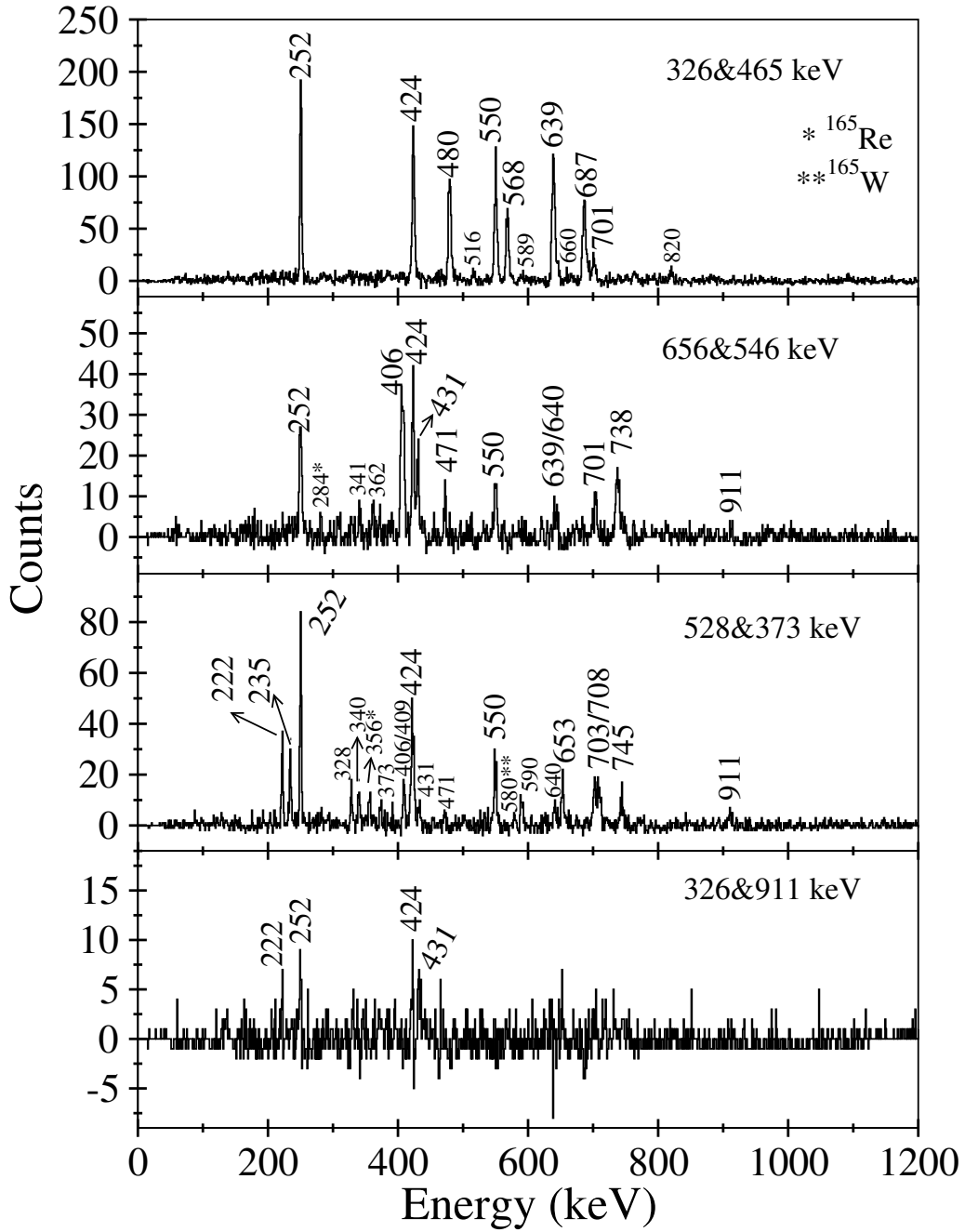


Figure 4.14: Examples of double-gated γ -ray coincidence spectra correlated with a recoil implantation in the GREAT spectrometer. (a) spectrum showing γ rays in coincidence with the 326 and 465 keV transitions showing transitions in the yrast band. (b) γ rays in coincidence with the 546 and 656 keV transitions showing transitions in Band 2. (c) γ rays in coincidence with the 373 and 528 keV transitions showing transitions in Band 3. (d) γ rays in coincidence with the 326 and 911 keV transitions.

linking transitions from the 12^+ state to the negative-parity bands. No evidence for linking transitions could be found suggesting that decay path from the 12^+ state

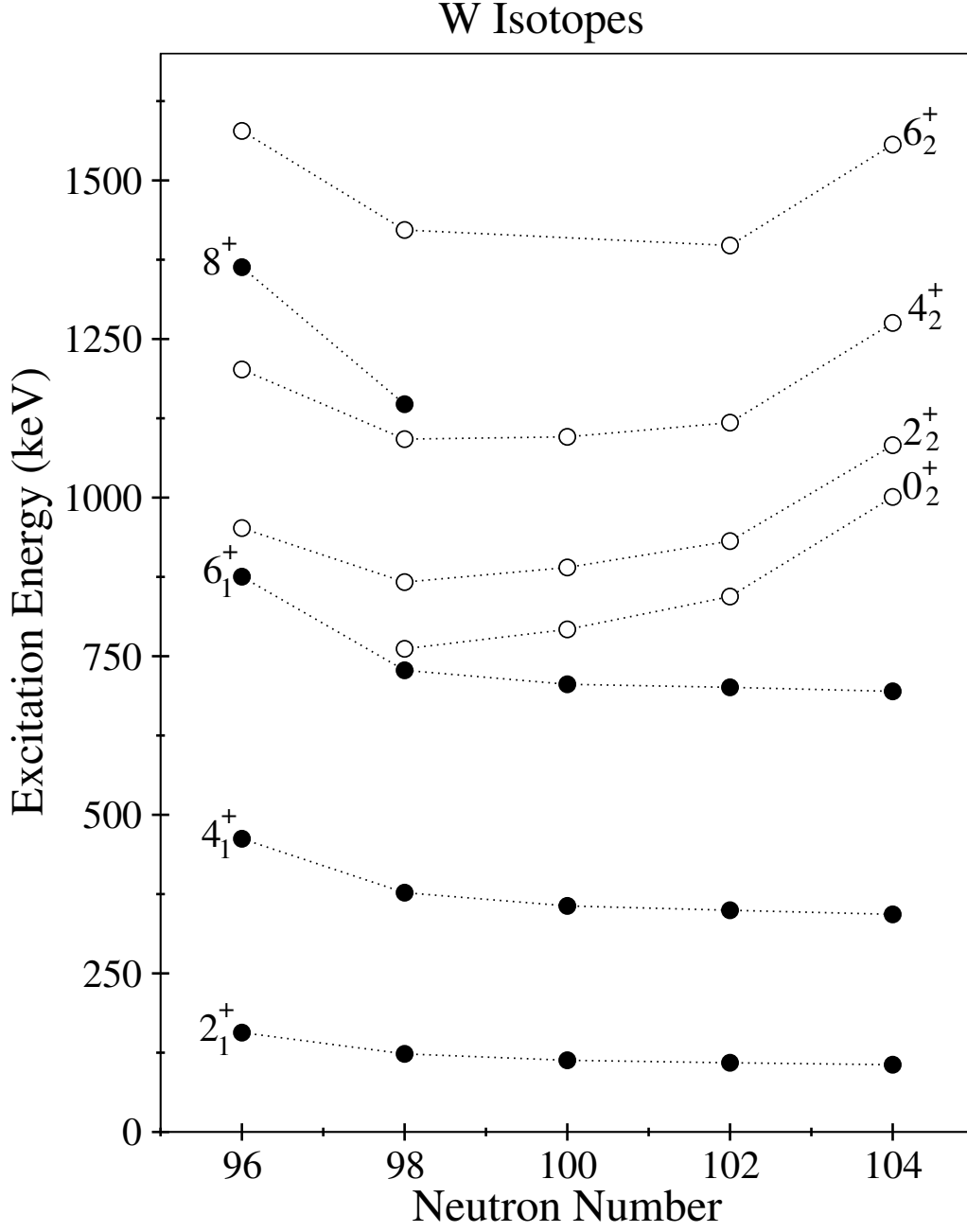


Figure 4.15: Excitation energies of quasi- β bands in ^{166}W . Data taken from references [102]

^{166}W is not fragmented. The model for ^{168}Os revealed that the effect of the lifetime of the 12^+ state with a doublet placed over it starts at given lifetime of 10 ps and the 12^+ state lifetime in ^{166}W is measured in this work ($\tau=27(4)$ ps). However, no analogous doublet could be identified in ^{166}W .

No evidence could be found for a non-yrast positive-parity structure as seen in ^{168}Os . The absence of a quasi- β band in ^{166}W is not surprising. Kibedi *et al.* performed measurements of the non-yrast states in the even- N W isotopes from ^{178}W to ^{170}W and found that the quasi- β band has a parabolic energy dependence on neutron number, see Figure 4.15 [102]. Kibedi *et al.* also noted that comparisons of quasi- β bands in the Os, Pt and Hg isotopes revealed a trend towards higher excitation energies for the excited 0^+ state as the proton number decreases from $Z = 82$ providing an explanation for the absence of the quasi- β band in ^{166}W [102].

A thorough search has been made to identify potential contaminants in the coincidence spectra arising from either new transitions in ^{166}W or from other fusion-evaporation channels in this data set. No extensions were made to the level scheme and no contaminants have been identified. Hence, it is concluded that the anomalous $B(E2)_{4^+/2^+}$ ratios in ^{166}W and ^{168}Os do not have a common origin.

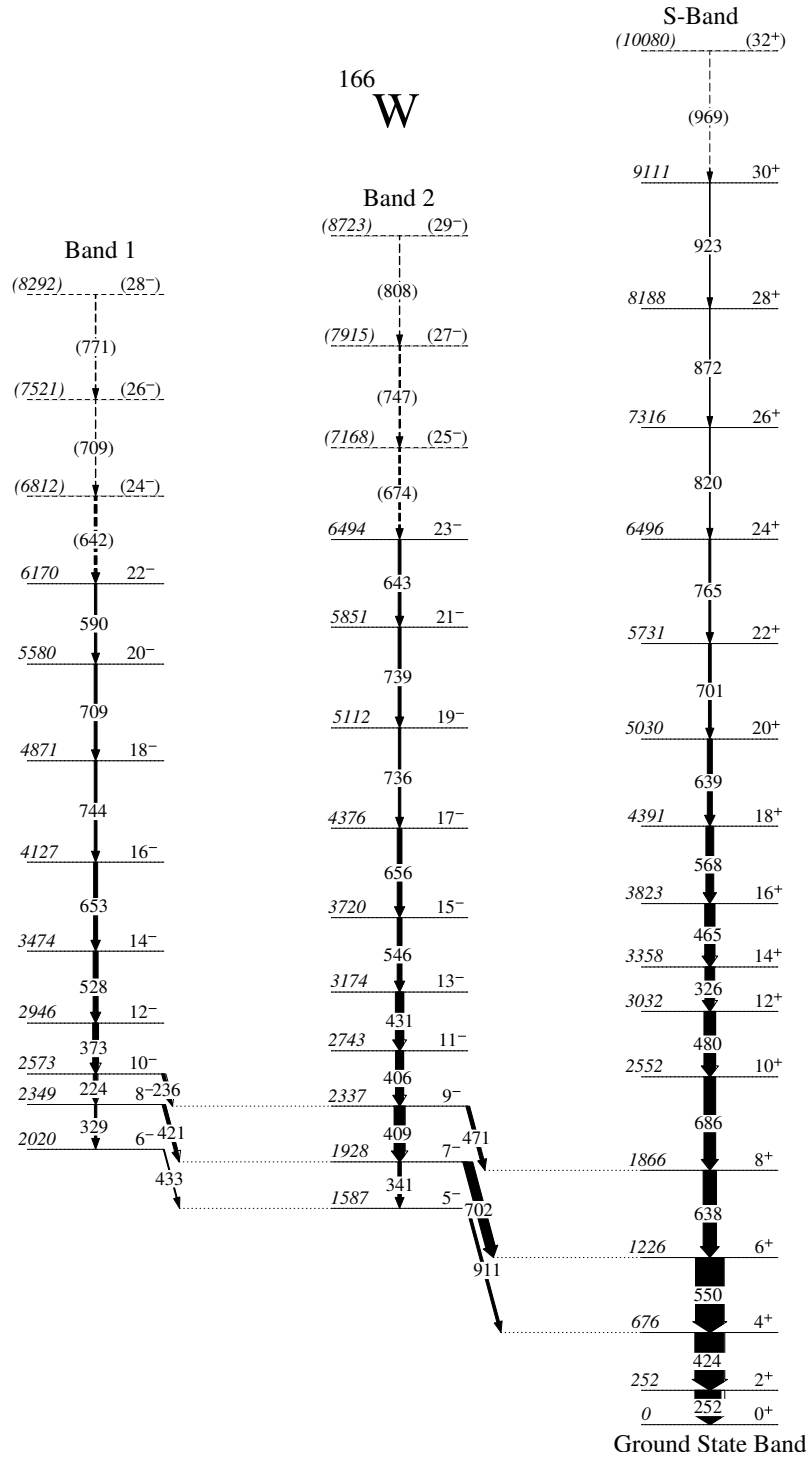


Figure 4.16: Level scheme of ^{166}W showing the yrast and side bands [96].

4.4.3 Comparison with Nuclear Models

Raman has provided a survey of theoretical $B(E2:2^+ \rightarrow 0^+)$ values using different model approaches in the $2 \leq Z \leq 100$ nuclei [29]. Figure 4.17 shows a comparison between experimental $B(E2:2^+ \rightarrow 0^+)$ and those predicted by the Finite-Range Droplet Model (FRDM), the Woods-Saxon Model (WSM) and the Dynamical Microscopic Model (DMM) for the $92 \leq N \leq 108$ tungsten isotopes. The theoretical values for $B(E2; 0^+ \rightarrow 2^+)_{\uparrow}$ in Reference [29] were corrected to $B(E2; 2^+ \rightarrow 0^+)_{\downarrow}$ [103] using

$$B(T_{\lambda}; I_2 \rightarrow I_1) = \frac{2I_1 + 1}{2I_2 + 1} B(T_{\lambda}; I_1 \rightarrow I_2) \quad (4.4)$$

In the FRDM, the nuclear potential energy is calculated using a macroscopic-microscopic model. The macroscopic part of the potential comes from the finite-range droplet model and the microscopic part employs shell and pairing corrections from a folded Yukawa single-particle potential. The WSM uses the Strutinsky shell correction method. The macroscopic part of the potential is given by the Yukawa-plus-exponential mass formula and the microscopic part of the potential is calculated by Woods-Saxon potential. The DMM [104] is based on the generator coordinate method (GCM) with a Gaussian overlap approximation. The nuclear potential is calculated by the shell-correction method of Strutinsky with liquid-droplet macroscopic part and zero-point energy [29]. In general, all three models predict qualitatively the behaviour of experimental measurements. While the FRDM and WSM calculations reproduce the magnitude of the experimental $B(E2:2^+ \rightarrow 0^+)$ values they both fail in their prediction for the $N = 92$ tungsten isotope. The DMM predictions shown in Figure 4.17(c) fails to reproduce the experimental results in terms of absolute magnitude. Figure 4.17(d) shows the DMM calculations normalised the the experimental measurements and indicates that the $B(E2:2^+ \rightarrow 0^+)$ trends are reproduced well for all isotopes including ^{166}W . The generator coordinate method

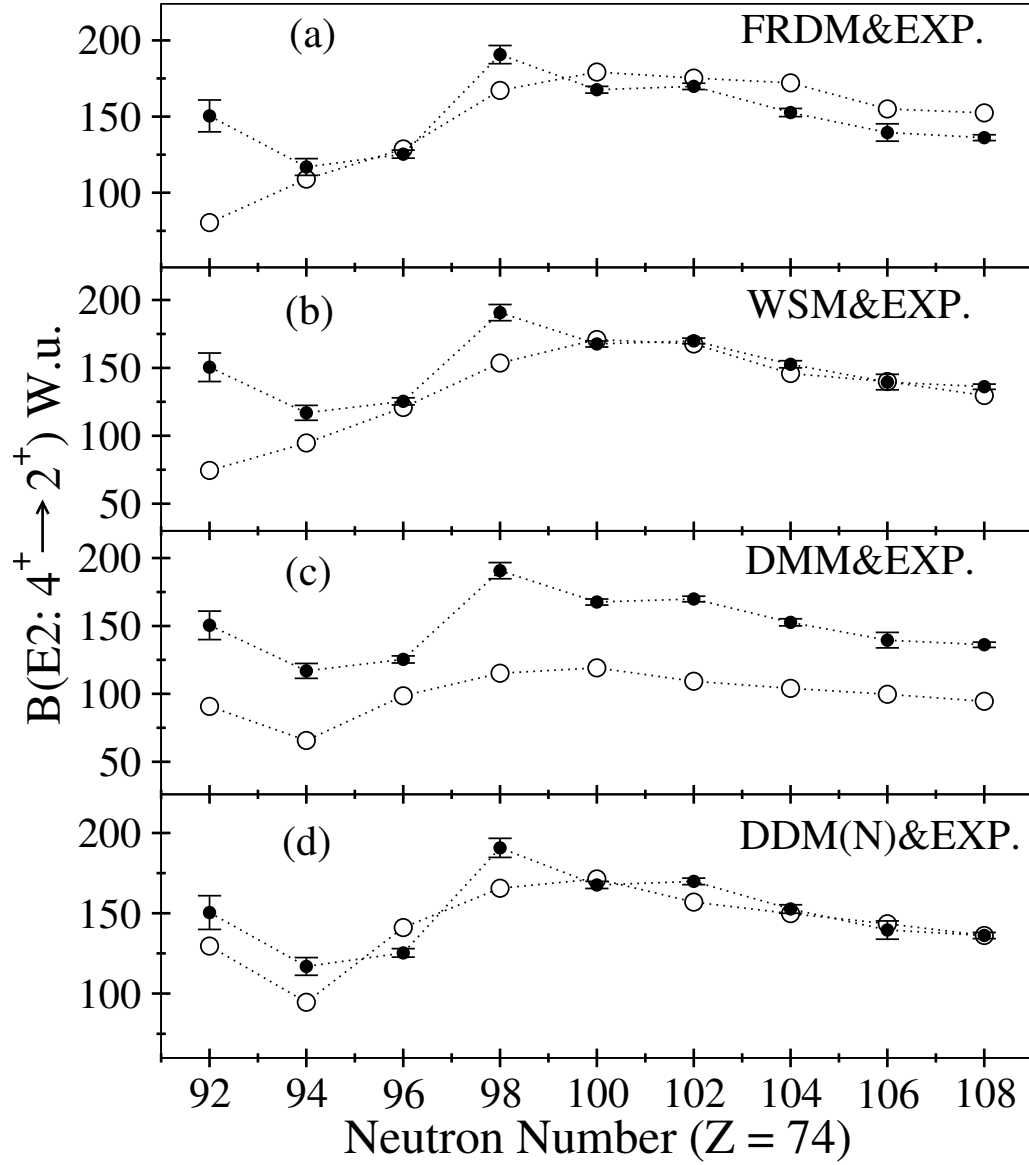


Figure 4.17: The comparison of theoretical calculations for 2^+ states in tungsten isotopes with experimentally measured values. The theoretical values were taken from Reference [29]. (a) Finite-Range Droplet Model (FRDM) (b) WoodsSaxon Model (WSM) (c) Dynamical Microscopic Model (DMM) and (d) DMM calculations theoretical predictions were normalised with experimental value of ^{182}W . Data from National Nuclear Data Center (NNDC). Exceptions are ^{172}W and ^{178}W [90], ^{174}W [91] and ^{176}W [92]. ^{166}W from present work.

is often regarded as the optimal approach for describing transitional nuclei through the microscopic determination of the collective dynamics for anharmonic vibrations and rotations [105, 106]. While beyond the scope of this thesis, a detailed theoretical study of the DMM framework might reveal the underlying physical basis for the unusual nature of the 2^+ state in the γ -soft transitional nuclide, ^{166}W .

4.4.4 High-Spin Structure of ^{166}W

Figure 4.18 shows the systematic trends for reduced transition probabilities and level excitation energies for the 6^+ , 12^+ and 14^+ states in ^{166}W . Figure 4.18(a) and (b) reflect a trend of decreasing collectivity with increasing spin up to the 12^+ state. In the rare earth region $A \sim 160$, backbending occurs due to a crossing of the g-band and a two quasi-particle band based on $i_{13/2}$ neutrons at $12 \leq I \leq 16$ [107, 108]. The 12^+ and 14^+ states in ^{166}W are expected to be the lowest transitions in the band formed by the rotational alignment of a pair of $i_{13/2}$ neutrons, see Figure 4.19(a). For the crossing bands, the two factors that give rise to S -shaped curve are the difference between the effective moments of inertia of two intersecting band and the strength of the interaction of the bands. Lifetime measurements in the $(12-16\hbar)$ backbending region allow the E2 transition strengths to be deduced, which provides an insight into the strength of the interaction. The lifetime measurement of ^{168}W revealed a dramatic reduction in the ground-Stockholm band crossing strength [109]. The corresponding value for the $12_s^+ \rightarrow 10_g^+$ transition is a factor of 50 lower than the the B(E2) value of the $14_s^+ \rightarrow 12_s^+$ transition. This dramatic reduction was interpreted as an existence of very weak mixing between the bands with an interaction matrix element of $10 < V < 19$ keV.

Figure 4.19(b) shows the variation of the B(E2) transition strength with increasing spin in the nuclides ^{166}W and ^{168}W . The backbending occurs of the same rotational frequency for both ^{166}W and ^{168}W . Consequently, a similar behaviour is expected in the evolution of the B(E2) values in the crossing region. Figure 4.19(b) shows a sharp change in the collectivity from 12^+ to 14^+ state. In the both nuclei, the s-g crossing occurs at the $12_s^+ \rightarrow 10_g^+$ transition. In conclusion, the sudden change in the B(E2) transition probability allow us to infer a weak interaction between the crossing bands in ^{166}W .

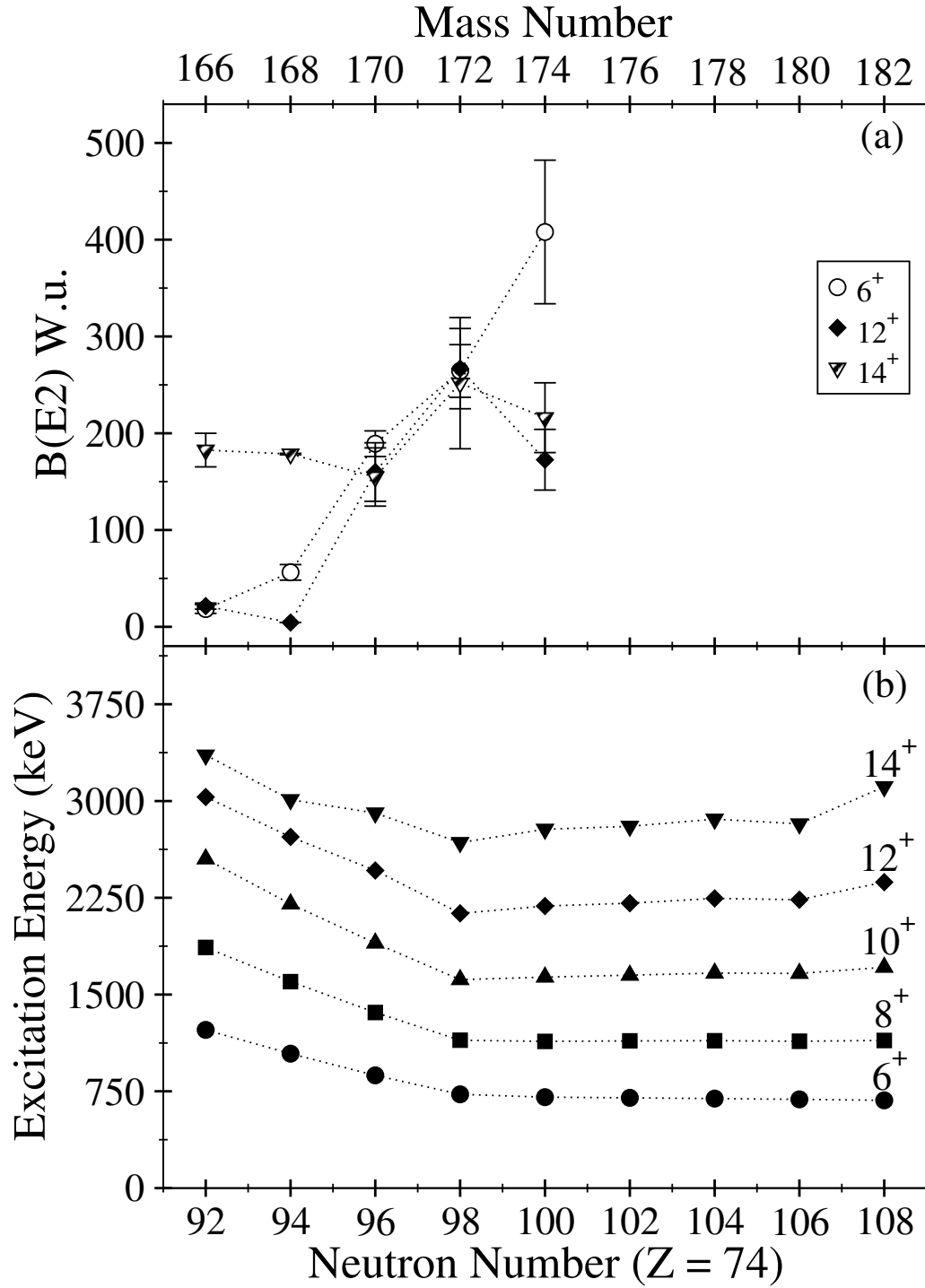


Figure 4.18: (a) $B(E2)$ values of excited states for W isotopes as a function of neutron number. (b) Energies of excited states for W isotopes as a function of neutron number. Data from National Nuclear Data Center (NNDC). Exceptions are $B(E2)$ values for ^{166}W from present work

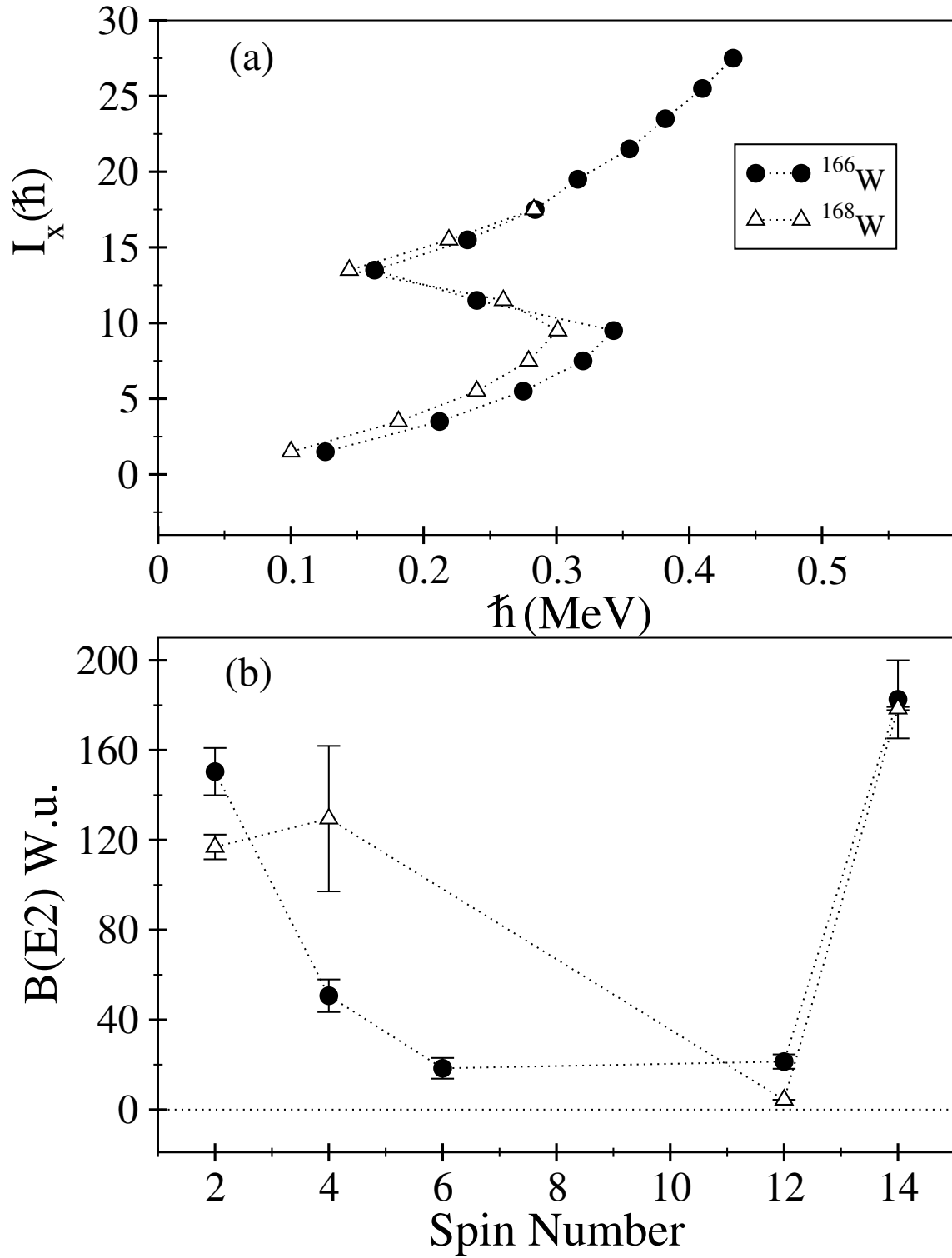


Figure 4.19: (a) B(E2) values of excited states for W-isotopes as a function of neutron number.(b) Energies of excited states for W-isotopes as a function of neutron number. Data for ^{168}W from Ref [109], excitation energies for ^{166}W from Ref [96] and B(E2) values from present work.

4.5 Summary

Lifetimes of the excited states in ^{166}W have been measured for the first time. Excited states in ^{166}W were populated in the reaction $^{92}\text{Mo}(^{78}\text{Kr},4\text{p})$ at a bombarding energy of 380 MeV. The lifetimes of 2^+ , 4^+ , 6^+ , 12^+ and 14^+ states in ^{166}W have been determined using the RDDS method. Reduced transition probabilities extracted from these lifetimes have revealed an abnormal $B(E2)_{4^+/2^+}$ ratio with a value of 0.33(5). In the Bohr collective model, this ratio is expected to be approximately 1.43 [50]. The systematics of the 2^+ and 4^+ have been investigated and suggest that the 2^+ state is more collective than usual and the 4^+ state is less collective than it should be. The level scheme has been reviewed with a complementary single-target experiment and no further extensions have been observed (c.f. ^{168}Os) that would reveal an obvious structural origin for the anomalous $B(E2)_{4^+/2^+}$ ratio. The experimental 2^+ systematics in the W isotopes have been compared with theoretical predictions. The Dynamical Microscopic Model based on the generator coordinate method is able to reproduce qualitatively the experimental behaviour for $92 \leq N \leq 108$ tungsten isotopes [29].

The lifetimes of the 6^+ , 12^+ and 14^+ states in ^{166}W show that the trend of decreasing of collectivity with increasing spin continues up to the 12^+ state. A sudden change in the $B(E2)$ transition probability occurs for the $12^+ \rightarrow 14^+$ transition suggesting a weak interaction at the ground-Stockholm band crossing in ^{166}W .

Chapter 5

Conclusion and Future Work

In this work, one of the main goals was to explain the anomalous ratio of the $B(E2)_{4+/2+} = 0.36(13)$ in ^{168}Os measured in an earlier lifetime experiment by Grahn *et al.* [1]. In order to investigate the abnormal behaviour from an different perspective, the level scheme of ^{168}Os has been examined and an empirical model has been produced. The level scheme of ^{168}Os has been extended in a recent experiment at the Accelerator Laboratory of the University of Jyväskylä (JYFL) employing JUROGAMII and GREAT [55] spectrometer in conjunction with RITU [54] separator. The decay of 12^+ state is found to be more fragmented with two new decay paths being observed. The new decay branch via the 126 keV γ -ray feeds a new positive parity structure while the branch proceeding through the 243 keV γ -ray feeds the known octupole structure. The lifetime data of Grahn *et al.* [1] and the fragmented decay paths reported in this thesis indicate that the 12^+ state has a relatively long lifetime.

These features were investigated in a model that uses the Bateman equations within the framework of the differential decay curve method [69] and takes into account the long lifetime of the 12^+ and doublet of 642/643 keV transition, which corresponds to the $4^+ \rightarrow 2^+$ transition energy. The model suggests that the long life-

time of the 12^+ state has no effect on the apparent lifetime of the 4^+ state. However, the combined effect of the 642/643 keV doublet components straddling a long-lived 12^+ state lengthens the apparent lifetime of the 4^+ state. In addition, we have observed that contamination from γ -ray emissions from nuclei populated in other reaction channels also affect the apparent lifetime of the level of interest. For example, ^{167}Re is produced in the same reaction and has γ -ray transitions that are similar to the $6^+ \rightarrow 4^+$ and $4^+ \rightarrow 2^+$ transitions in ^{168}Os . These transitions will appear at some level in the recoil-gated γ -ray coincidence spectra. The model has been used to consider the role of contaminants and concluded that, in this case, the doublets will shorten the apparent lifetime of the 4^+ state. Hence, the weak contamination from ^{167}Re does not explain the anomalous $B(E2)_{4^+/2^+}$ ratio. It is concluded that level schemes should be checked carefully for doublets and their placement relative to long-lived excited states if true (and not apparent) lifetimes are to be measured.

This thesis also reports the first lifetime measurements of yrast states in ^{166}W . These results come from a recent RDDS experiment that performed at the Accelerator Laboratory of the University of Jyväskylä (JYFL). The differential plunger DPUNS device [56] was installed at the JUROGAMII target position and coupled to the RITU [54] separator and GREAT [55] spectrometer. Lifetimes of excited states have been extracted using differential decay curve method in coincidence mode in order to eliminate the influence of unobserved side feeding. In this study, the reduced transition probability $B(E2)$ values for transitions depopulating the 2^+ , 4^+ , 6^+ , 12^+ and 14^+ states have been deduced from the measured lifetimes. The $B(E2) = 150(9) \text{ W.u.}$ value confirmed that the 2^+ state has a collective behaviour. However, the collectivity of the 4^+ state is measured to be lower than the 2^+ state, which results in an anomaly in the $B(E2)_{4^+/2^+}$ ratio ($B(E2)_{4^+/2^+} = 0.33(5)$). An examination of systematics of related states revealed that the 2^+ state is more col-

lective than usual and the 4^+ state is perhaps less collective than it should be. The lifetimes of the 6^+ , 12^+ and 14^+ states in ^{166}W show that the trend of decreasing of collectivity with increasing spin continues up to the 12^+ state. A sudden change in the $B(E2)$ reduced transition probability occurs from 12^+ to 14^+ that suggests a weak interaction between the intersecting bands in ^{166}W similar to ^{168}W [109].

A new recoil-correlated single-target experiment was used to investigate the level of ^{166}W . Unlike ^{168}Os , no doublets have been observed for the key transitions and no new bands structures have been identified. The 12^+ state does not have a fragmented structure and its lifetime has been measured in this work ($\tau=27(4)$ ps). Moreover, no fusion-reaction products have been seen in the recoil-gated spectrum that contaminate transitions in ^{166}W . It is suggested that the source of the anomalous $B(E2)_{4^+/2^+}$ ratio in ^{166}W is different to that measured for ^{168}Os . A qualitative comparison of the experimental $B(E2; 2^+ \rightarrow 0^+)$ trends for the W isotopes with model predictions imply that a dynamical macroscopic-microscopic model based on the generator coordinate method [105, 106] reproduces the enhanced collectivity of the 2^+ state relative to the heavier isotopes. Further theoretical work must be done to explore this phenomenon in heavy transitional nuclei. Further experiments probing this anomaly are approved at JYFL and the Argonne National Laboratory to measure the lifetimes of low-lying states in ^{166}Os and ^{170}Os .

Bibliography

- [1] T. Grahn, *Private Conversation* .
- [2] A. Bohr and B. R. Mottelson, *Nuclear Structure, Volume II, : Nuclear Deformation* (World Scientific, 1998).
- [3] M. G. Mayer, Phys. Rev. **78**, 16 (1950).
- [4] O. Haxel, J. H. D. Jensen, and H. E. Suess, Phys. Rev. **75**, 1766 (1949).
- [5] E.S. Paul *et al.*, Phys. Rev. **C51**, 78 (1995).
- [6] A. Keenan *et al.*, Phys. Rev. C **63**, 064309 (2001).
- [7] S.L. King *et al.*, Phys. Rev. C **62**, 067301 (2000).
- [8] D.E. Appelbe *et al.*, Phys. Rev. C **66**, 014309 (2002).
- [9] S.L. King *et al.*, Phys. Lett. **B443**, 82 (1998).
- [10] D. O'Donnell *et al.*, Phys. Rev. C **85**, 054315 (2012).
- [11] D.T. Joss *et al.*, Phys. Rev. C **70**, 017302 (2004).
- [12] S.J. Steer *et al.*, Phys. Rev. C **84**, 044313 (2011).
- [13] D.T. Joss *et al.*, Nucl. Phys. A **689**, 631 (2001).
- [14] R. Bark, G. Dracoulis, and A. Stuchbery, Nuclear Physics A **514**, 503 (1990).

- [15] R. Kumar *et al.*, Phys. Rev. C **80**, 054319 (2009).
- [16] A. Dewald, O. Moller, and P. Petkov, Prog. in Part. and Nucl. Phys. **67**, 786 (2012).
- [17] H. Watkins *et al.*, Phys. Rev. C **84**, 051302 (2011).
- [18] T. Grahn *et al.*, Phys. Rev. C **80**, 014324 (2009).
- [19] M. Scheck *et al.*, Phys. Rev. C **81**, 014310 (2010).
- [20] T. Grahn *et al.*, Phys. Rev. Lett. **97**, 062501 (2006).
- [21] J.J. Ressler *et al.*, Phys. Rev. C **69**, 034317 (2004).
- [22] R. B. Cakirli, R. F. Casten, J. Jolie, and N. Warr, Phys. Rev. C **70**, 047302 (2004).
- [23] D. Radeck *et al.*, Phys. Rev. C **85**, 014301 (2012).
- [24] E. Williams *et al.*, Phys. Rev. C **74**, 024302 (2006).
- [25] C.R. Fitzpatrick *et al.*, Phys. Rev. C **78**, 034309 (2008).
- [26] O. Möller *et al.*, Phys. Rev. C **71**, 064324 (2005).
- [27] G. de Angelis *et al.*, Phys. Lett. **B535**, 93 (2002).
- [28] G. Jakop *et al.*, Phys. Rev. C **65**, 024316 (2002).
- [29] S. Raman, C. Nestor, and P. Tikkanen, Atomic Data and Nuclear Data Tables **78**, 1 (2001).
- [30] W. Dehnhardt *et al.*, Nucl. Phys. **A225**, 1 (1974).
- [31] M. O. M. I. A. Makishima, T. Ishii, Nucl. Instrum. Methods. Phys. Res. A. **363**, 591 (1995).

- [32] B. Kharraja *et al.*, Phys. Rev. C **61**, 024301 (1999).
- [33] A.A. Sonzogni, Nuclear Data Sheets **93**, 599 (2001).
- [34] M.J.A De Voigt *et al.*, Nucl. Phys. **A507**, 472 (1990).
- [35] P. Ring and P. Schuck, *The Nuclear Many-Body Problem* (Springer, 2004).
- [36] R. A. Dunlop, *An Introduction to The Physics of Nuclei and Particles* (Brooks/Cole, CENGAGE Learning, 2004).
- [37] R. F. Casten, *Nuclear Structure from a Simple Perspective* (Oxford Science Publications, 2000).
- [38] V. Soloviev, *Theory of Complex Nuclei* (Pergamon Press, 1976).
- [39] R. Woods and D. Saxon, Phys. Rev. **95**, 577 (1954).
- [40] J. Rainwater., Phys. Rev. **79**, 432 (1950).
- [41] A. Bohr., Phys. Rev. **81**, 134 (1951).
- [42] A. Faessler and R. K. Sheline, Phys. Rev. **148**, 1003 (1966).
- [43] S. Nilsson, Mat. Fys. Medd. Dan. Vid. Selsk. **69**, 16 (1955).
- [44] S. G. Nilsson and I. Radnarsson, *Shapes and Shells in Nuclear Structure* (Cambridge University Press, 1995).
- [45] R. Bengtsson, J. Dudek, W. Nazarewicz, and P. Olanders, Physica Scripta **39**, 196 (1989).
- [46] D. J. Rowe, *Nuclear Collective Motion, Models and Theory* (World Scientific, 2010).

- [47] K. Krane, R. Steffen, and R. Wheeler, Atomic Data and Nuclear Data Tables **11**, 351 (1973).
- [48] S. S. Wong, *Introductory Nuclear Physics* (Wiley, 2004).
- [49] K. S. Krane, *Introductory Nuclear Physics* (John Wiley and Sons, Inc, 1988).
- [50] D. J. Rowe and J. L. Wood, *Fundamentals of Nuclear Models, Foundational Models* (World Scientific, 2010).
- [51] J. Suhonen, *From Nucleons to Nucleus, Concepts of Microscopic Nuclear Theory* (Springer, 2007).
- [52] K. Heyde, *Basics Ideas and Concepts in Nuclear Physics* (Institute of Physics, 2000).
- [53] J. Cetnar, Ann. Nucl. Eng **33**, 640 (2006).
- [54] M. Leino, Nucl. Instrum. Methods. Phys. Res. B **126**, 320 (1997).
- [55] R.D. Page *et al.*, **204**, 634 (2003).
- [56] M.J. Taylor *et al.*, Nucl. Instr. and Meth. **A707**, 143 (2013).
- [57] H. Morinaga and P. Gugelot, Nucl. Phys. **46**, 210 (1963).
- [58] C.W. Beausang *et al.*, Nucl. Instrum. Methods. Phys. Res. A **313**, 37 (1992).
- [59] G. Duchêne *et al.*, Nucl. Instrum. Methods. Phys. Res. A **432**, 90 (1999).
- [60] J. Sarén, J. Uusitalo, M. Leino, and J. Sorri, Nucl. Instrum. Methods. Phys. Res. A **654**, 508 (2011).
- [61] M. Leino *et al.*, Nucl. Instrum. Methods. Phys. Res. B **99**, 653 (1995).

- [62] J. Sarén, J. Uusitalo, M. Leino and J. Sorri., Nucl. Instrum. Methods. Phys. Res. A. **654**, 508 (2011).
- [63] I.H. Lazarus *et al.*, Nuclear Science, IEEE Transactions on **48**, 567 (2001).
- [64] T. Grahn, *Ph.D Thesis* (University of Jyväskylä, 2006).
- [65] L. Cleemann, J. Eberth, W. Neumann, N. Wiehl, and V. Zobel, Nucl. Instr. Meth. **156**, 477 (1978).
- [66] T. Alexander and A. Bell, Nucl. Instrum. Meth. **81**, 22 (1970).
- [67] P. J. Nolan and J. F. Sharpey-Schafer, Reports on Progress in Physics **42**, 1 (1979).
- [68] A. Z. Schwarzschildt and E. K. Warburton, Annual Review of Nuclear Science **18**, 197 (1968).
- [69] A. Dewald, S. Harissopulos, and P. von Brentano, Zeitschrift für Physik A Hadrons and Nuclei **334**, 163 (1989).
- [70] G. Böhm, A. Dewald, P. Petkov, and P. von Brentano, Nucl. Instrum. Methods. Phys. Res. A. **329**, 248 (1993).
- [71] D. Ward *et al.*, Phys. Rev. Lett. **30**, 493 (1973).
- [72] L. Bianco *et al.*, Phys. Lett. **B690**, 15 (2010).
- [73] T. Kurtukian-Nieto *et al.*, Preprint, 2007.
- [74] R. Robinson and M. Thoennessen., At. Data Nucl. Data Tables **98**, 911 (2012).
- [75] M.C. Drummond *et al.*, Phys. Rev. C **87**, 054309 (2013).
- [76] K. Lagergren *et al.*, Phys. Rev. C **83**, 014313 (2011).

- [77] J.M. Rees *et al.*, Phys. Rev. C **83**, 044314 (2011).
- [78] G.D. Dracoulis *et al.*, Phys. Rev. C **44**, R1246 (1991).
- [79] T.M. J. Goon *et al.*, Phys. Rev. C **70**, 014309 (2004).
- [80] D. G. Jenkins *et al.*, Phys. Rev. **C66**, 011301(R) (2002).
- [81] M. Scheck *et al.*, Phys. Rev. C **83**, 037303 (2011).
- [82] R.D. Page *et al.*, Phys. Rev. C **84**, 034308 (2011).
- [83] A.N. Andreyev *et al.*, Nature(London) **405**, 430 (2010).
- [84] G.D. Dracoulis *et al.*, Phys. Rev. C **69**, 054318 (2004).
- [85] P. Rahkila., Nucl. Instrum. Methods. Phys. Res. A **595**, 637 (2008).
- [86] D. C. Radford., Nucl. Instrum. Methods. Phys. Res. A **361**, 297 (1995).
- [87] P. E. Garrett, Journal of Physics G: Nuclear and Particle Physics **27**, R1 (2001).
- [88] T. Kibedi, G.D. Dracoulis, A.P. Byrne, P.M. Davidson, and S. Kuyucak., Nucl. Phys. **A567**, 183 (1994).
- [89] G.D. Dracoulis *et al.*, Journal of Physics G: Nuclear Physics **12**, L97 (1986).
- [90] M. Rudigier, J.-M. Régis, J. Jolie, K. Zell, and C. Fransen, Nucl. Phys. A **847**, 89 (2010).
- [91] V. Werner *et al.*, Journal of Physics: Conference Series **312**, 092062 (2011).
- [92] M. Régis *et al.*, Nucl. Instrum. Methods. Phys. Res. A **606**, 466 (2009).
- [93] K. S. Toth, W. D. Schmidt-Ott, C. R. Bingham, and M. A. Ijaz, Phys. Rev. C **12**, 533 (1975).

- [94] T. Hild *et al.*, Nuclear Physics A **492**, 237 (1989).
- [95] J. Gerl *et al.*, Nuclear Physics A **443**, 348 (1985).
- [96] J. Simpson *et al.*, Journal of Physics G: Nuclear and Particle Physics **18**, 1207 (1992).
- [97] M. Leino *et al.*, Nucl. Instrum. Methods. Phys. Res. B. **126**, 320 (1997).
- [98] J. Uusitalo *et al.*, Nucl. Instrum. Methods. Phys. Res. B. **204**, 638 (2003).
- [99] I. H. Lazarus *et al.*, IEEE Trans. Nucl. Sci. **48**, 567 (2001).
- [100] M.G. Procter *et al.*, Phys. Rev. C **84**, 024314 (2011).
- [101] A. Dewald *et al.*, Phys. Rev. C **68**, 034314 (2003).
- [102] T. Kibedi, G. Dracoulis, A. Byrne, and P. Davidson, Nuclear Physics A **688**, 669 (2001).
- [103] A. Bohr and B. R. Mottelson, *Nuclear Structure, Volume I, : Single Particle Motion* (World Scientific, 1998).
- [104] B. Nerlo-Pomorska, K. Pomorski, M. Brack, and E. Werner, Nucl. Phys. A **462**, 252 (1987).
- [105] P. G. Reinhard and K. Goeke, Reports on Progress in Physics **50**, 1 (1987).
- [106] N. Onishi and S. Yoshida., Nucl. Phys. **80**, 367 (1966).
- [107] F. Stephens, Rev. Mod. Phys **47**, 43 (1975).
- [108] R. Bengtsson and S. Frauendorf, Nucl. Phys. **A314**, 27 (1979).
- [109] G.D. Dracoulis *et al.*, Phys. Rev. C **29**, 1576 (1984).